



universität
wien

DISSERTATION

Titel der Dissertation

„Comparison of the measured X-ray yields of kaonic
helium-3 and helium-4“

Verfasserin

Mag. rer. nat. Barbara Katharina Wünschek

angestrebter akademischer Grad

Doktorin der Naturwissenschaften (Dr. rer. nat.)

Wien, 2012

Studienkennzahl lt. Studienblatt: A 791 411

Dissertationsgebiet lt. Studienblatt: Physik

Betreuerin / Betreuer: Hon.-Prof. Dipl.-Phys. Dr. Eberhard Widmann

Abstract

Kaonic helium is an exotic atom where a Kaon replaces a shell electron, well suited for the study of the strong interaction at low energies. The strong interaction between the kaon and the nucleus affects the low-lying atomic states in the kaonic helium atom by causing a shift compared to its electromagnetic value. This shift can be measured with spectroscopic tools, which was performed recently by two experiments. In particular, the SIDDHARTA experiment at LNF (Italy) investigated the strong interaction shift via the measurement of the X-ray transitions to the 2p level in kaonic helium-3 and kaonic helium-4. The E17 experiment at J-PARC (Japan), planned for 2012, measures a possible difference between the shifts in kaonic helium-3 and helium-4. For this purpose, so-called silicon drift detectors are used which have been optimized for the requirements of the experiment. Due to geometrical limits of the E17 setup, the properties of these detectors have been investigated in a similar setup. Their energy and time resolutions have been studied as a function of the detector temperature and compared to theoretical models of the electron mobility in silicon.

Furthermore, the yields (i.e. the transition rates) of the kaonic helium X-ray transitions to the 2p level were determined within this thesis. Therefore, the SIDDHARTA data were analysed, where the X-ray transitions in gaseous kaonic helium-3 and helium-4 were measured with a complex SDD detector system. The absolute yields were obtained with inputs from a Monte Carlo simulation. Since the previous measurements on the kaonic helium X-ray transitions solely used liquid kaonic helium, these results give crucial information on theoretical calculations of the density dependence of the yields. Additionally, the determination of the yields in gaseous kaonic helium-3 and helium-4 allows an estimation of the prospective X-ray detection efficiencies in E17.

Zusammenfassung

Kaonisches Helium ist ein exotisches Atom, welches sich besonders zur Untersuchung der starken Wechselwirkung bei niedrigen Energien eignet. Die starke Wechselwirkung zwischen Kaon und Heliumkern verursacht eine Verschiebung der inneren Energieniveaus des Atoms, die mithilfe spektroskopischer Methoden messbar ist. In den letzten Jahren wurden verstärkt im Zuge zweier Experimente (E570 in Japan und SIDDHARTA in Italien), die Verschiebung des 2p Niveaus in kaonischem Helium-3 und Helium-4 - über die Messung der Röntgenübergänge - bestimmt. Ein weiteres Experiment (E17) ist für 2012 an J-PARC, Japan, geplant, in welchem mögliche Unterschiede zwischen der Verschiebung in kaonischem Helium-3 und in kaonischem Helium-4 festgestellt werden sollen. Für das Experiment E17 werden neuartige, hochmoderne Siliziumdetektoren, sogenannte Silicon Drift Detektoren verwendet, deren Funktionsparameter für diese Messungen optimiert worden sind. Die Anforderungen des experimentellen Aufbaus von E17 erfordern zudem eine genaue Kenntnis der Detektoreigenschaften, die im Zuge dieser Doktorarbeit untersucht wurden. Hierfür wurde die Temperaturabhängigkeit ihrer Energie- und Zeitauflösung in einem ähnlichen experimentellen Aufbau an der Forschungsanlage KEK in Japan studiert und mit Modellen über die Elektroneneigenschaften in Silizium verglichen. Des Weiteren wurden in dieser Arbeit die Übergangsraten der Röntgenübergänge zum 2p Niveau in gasförmigem Helium bestimmt. Dazu wurden die Daten des SIDDHARTA Experiments ausgewertet, das mithilfe eines komplexen SDD-Detektorsystems, die Röntgenübergänge in kaonischem Helium-3 und Helium-4 gemessen hat. Die absoluten Übergangsraten wurden mit Hilfe einer Monte-Carlo Simulation ermittelt. Da alle bisherigen Experimente flüssiges Helium für die Untersuchung der Röntgenübergänge verwendet haben, konnte mit diesen Ergebnissen erstmals eine Dichteabhängigkeit der Übergangsraten experimentell beobachtet werden, die - besonders für theoretische Berechnungen - wichtige Informationen liefern. Ferner können damit die zu erwarteten Detektionsraten für E17, und damit die benötigte Messzeit, abgeschätzt werden.

Contents

1	Introduction	1
1.1	Precision X-ray spectroscopy with kaonic helium	1
1.2	Outline of this thesis	3
2	Kaonic Helium	5
2.1	An introduction to exotic atoms	5
2.2	Kaonic helium atoms	7
2.2.1	Processes in the kaonic helium atom	7
2.2.2	Theoretical framework for the K^- -nucleus interaction	10
2.2.3	The strong interaction shift in kaonic helium	11
2.2.4	The yields in kaonic helium	13
2.3	Calculation of the electromagnetic energy levels kaonic helium	15
2.4	Recent developments in kaonic helium	18
3	Silicon drift detectors for X-ray spectroscopy	23
3.1	Introduction	23
3.2	Working principle and response function of an SDD	26
3.3	SDDs for SIDDHARTA	28
3.4	SDDs and preamplifiers for E17	29
3.5	Temperature studies with E17-SDDs	32
3.5.1	Experimental setup	32
3.5.2	Data acquisition	33
3.5.3	Temperature dependence of preamplifier properties . .	36
3.5.4	Temperature dependence of SDD properties	37
3.6	Summary and comparison	41
4	Kaonic Helium with SIDDHARTA	45
4.1	The facility: DAΦNE	46

4.2	The SIDDHARTA Setup	49
4.3	Experimental procedure and data acquisition	52
4.3.1	Data recording	52
4.3.2	Data types	54
4.3.3	Data used for evaluation	55
4.4	Data evaluation: Calibration data	56
4.5	Data evaluation: Production data	59
4.5.1	Self-trigger data	59
4.5.2	Coincidence data	62
4.6	Yields in gaseous kaonic helium	74
4.6.1	Number of X-rays from the Monte Carlo simulation	74
4.6.2	Peak areas	83
4.6.3	Absolute and relative yields	87
4.7	Conclusion and summary	90
5	Kaonic helium with E17	93
5.1	J-PARC, the facility	94
5.2	E17 setup	95
6	Conclusions and summary	99
	Bibliography	103
	Acknowledgements	113
	Curriculum Vitae	115

List of Figures

2.1	Cascade in pionic hydrogen π^-H	9
2.2	The $3d \rightarrow 2p$ X-ray transition in kaonic helium	12
2.3	Model by Akaishi	13
2.4	Calculated and measured yields in liquid kaonic 4He	14
2.5	Theoretic strong interaction shifts in kaonic atoms	18
2.6	Sketch of the E570 setup at KEK	20
3.1	Drift chamber proposed by Gatti and Rehak	24
3.2	SDD proposed by Lechner	25
3.3	Model of an E17-SDD	25
3.4	Characteristic X-ray spectrum of Mn	28
3.5	Scheme of the SIDDHARTA-SDDs	29
3.6	Signal of a E17-preamplifier	30
3.7	Photograph of an E17-SDD	32
3.8	Vacuum chamber at KEK	33
3.9	Logic scheme of the SDD studies	34
3.10	Drift time distribution of an SDD	35
3.11	Effects of the preamplifier temperature	37
3.12	Effects of the SDD temperature on the response function	38
3.13	Peak center as a function of SDD temperature	40
3.14	Simulation of the drift time distribution of SDDs	42
4.1	Photograph of the two main rings at DAΦNE	46
4.2	Accelerators at DAΦNE	47
4.3	Injection cycle at DAΦNE	48
4.4	The SIDDHARTA setup	49
4.5	Photograph of the target cell	52
4.6	Logic scheme of the data acquisition in SIDDHARTA	53

4.7	Correlated and uncorrelated SDD data	55
4.8	Overview of the measurements with SIDDHARTA	56
4.9	Calibration spectrum of an SDD	57
4.10	Comparison of two simulated SDD response functions	58
4.11	Energy spectrum of kaon-uncorrelated X-ray data	59
4.12	Energy dependence of the Gauss-widths	61
4.13	Energy spectra of the raw coincidence data	62
4.14	The impact of the time walk	63
4.15	Energy cuts for the slewing correction	65
4.16	The slewing corrected data	65
4.17	2D spectrum of the kaon detector	66
4.18	Comparison a the raw and a corrected energy spectrum	67
4.19	Final energy spectra of kaonic ^3He and ^4He	70
4.20	Self-trigger spectrum of all chosen 92 SDD	72
4.21	Technical drawing	75
4.22	Kaonic X-rays as a function of foil/degrader thickness	77
4.23	Simulated kaon stops	79
4.24	Time difference between SDD and kaon detector	84
4.25	Entries in three SDDs as a function of time	86
4.26	Absolute and relative yields in kaonic ^3He and ^4He	88
4.27	Absolute yields of kaonic Kapton atoms	89
4.28	Yields in comparison with other experiments and theory	92
5.1	Overview over the J-PARC facility	93
5.2	Photograph of the K1.8BR beam line in the hadron hall	94
5.3	Schematic view of the E17 setup	95
5.4	Model of the CDS	96
5.5	Technical drawing of the cryostat	97

List of Tables

2.1	Calculated electromagnetic atomic states in kaonic ^3He	16
2.2	Calculated electromagnetic X-ray transitions in kaonic helium	17
4.1	Peak intensity ratios of further X-ray peaks	69
4.2	The strong interaction shift in kaonic ^3He	73
4.3	Error contribution	81
4.4	X-ray detection efficiencies for ^3He and ^4He	82
4.5	Calculated absolute yields in ^3He and ^4He	87

Chapter 1

Introduction

1.1 Precision X-ray spectroscopy with kaonic helium

The study of the strong interaction at low energies is a domain of quantum chromodynamics (QCD) which still offers plenty of room for more exploration. In particular the theoretical extension to systems with strangeness relies on experimental studies which gained more and more interest in the recent years. Exotic atoms with a hadron (e.g. antiproton \bar{p} , antikaon K^-) replacing a shell electron are suitable candidates for a spectroscopical observation of the effects of the strong interaction. Since the low lying atomic states of such atoms are shifted and broadened due to the strong interaction between hadron and nucleus, from these shifts and widths conclusions on the nuclear potential can be drawn. In particular the determination of the 2p level strong interaction shift in kaonic helium gives information about possible kaon-bound states in the nucleus. Motivated by a discrepancy between theoretical predictions and former experimental results, as well as by new theoretical aspects, recently three experiments approached the X-ray spectroscopy of the transitions to the 2p level in kaonic helium. The E570 experiment solved the discrepancy in ^4He in favor of the theoretical predictions, which was confirmed by the SIDDHARTA group two years later. Although the SIDDHARTA group also obtained a similar result for ^3He in 2011, the possibility of an isospin difference in the shift is still open. This issue - among others - is tackled by the E17 experiment at J-PARC, planned after 2012, by measuring the 2p level shift and width in kaonic ^3He and ^4He

with a precision of less than 2 eV.

One part of the presented work was an investigation of the silicon drift detectors (SDDs) used for the E17 experiment. These state-of-the-art detectors are optimized for X-ray spectroscopy, characterized by a large area and a good energy resolution. Similar detectors of the same type have already been used for SIDDHARTA and E570, nevertheless crucial characteristics of the E17 setup required a detailed study of the SDD response function. The presented measurements are a unique study of the temperature behavior of SDDs and give the basic conditions for their operation during the experiment. In order to understand the results, they were compared to models of the electron mobility in silicon.

The second part of the thesis focuses on the determination of the kaonic helium yields of the X-ray transitions to the 2p level state in gaseous helium, i.e. on the number of X-rays of a transition per captured kaon. Therefore, the data from the SIDDHARTA experiments in gaseous ^3He and ^4He with different densities have been evaluated. With inputs from a Monte Carlo simulation, the yields were calculated and compared to previous results on liquid ^4He . The determination of the yields in gaseous kaonic helium are also a key subject for theoretical models dealing with the density dependence of yields and for the estimation of the prospective number of detected X-rays in future experiments on kaonic helium, such as E17.

1.2 Outline of this thesis

In chapter 2 of this thesis, an introduction to kaonic helium is presented. The processes in the atom, as well as a summary of the theoretical models dealing with the kaon-nucleus interaction are described. The end of the chapter focuses on a detailed description and calculation of the 2p state in kaonic helium.

The next part is dedicated to silicon drift detectors. First, a summary about recent developments is given, followed by a presentation of their working principle. The detectors for SIDDHARTA and E17 are described in detail and compared. The main part of this chapter is the presentation of the temperature studies of the SDDs' response function.

Chapter 4 concentrates on the analysis of the SIDDHARTA data. A description of the setup is followed by a report of the data taking and calibration processes. The evaluation, including a determination of the 2p level shift in kaonic ^3He , is described. Also a description of the Monte Carlo simulation is given from which the number of detected X-rays per kaon is obtained for the calculation of the yields, followed by the results of the relative and the absolute yields in gaseous kaonic ^3He and ^4He . Finally, the results are discussed and compared to theoretical models and former experiments.

In the last chapter, a short overview of the J-PARC facility and the E17 setup is given.

Chapter 2

Kaonic Helium

2.1 An introduction to exotic atoms

Exotic atoms, extensively described in references [1–3], have already been postulated by Fermi and Teller in 1947. Such atoms are not solely composed of electrons, neutrons and protons: an exotic particle can replace either the nucleus (e.g. positronium e^+e^- or muonium μ^+e^-) or a shell electron. In case of a replaced shell electron, its substitutes are leptons which interact weakly and electromagnetically with the nucleus, or hadrons where also strong interaction occurs. These leptonic or hadronic atoms are named after the particle replacing the electron. They are formed when a decelerated negatively charged particle X^- is captured by a target atom in an outer orbit with a principal quantum number n of

$$n \approx n_e \cdot \sqrt{\frac{\mu_{X^-}}{m_e}} \quad (2.1)$$

with n_e as the principal quantum number of the corresponding electron orbit, m_e as the electron mass and μ_{X^-} as the reduced mass of an arbitrary captured particle in the atom. The ℓ sub-states population proceeds statistically in a first approximation, i.e. it is related to the available density of states. The Pauli principle is disabled since only one exotic particle is captured.

After being captured, the particle cascades down through its own series of atomic bound states, usually located inside the electron levels due to its higher mass. The cascade, in detail described in section 2.2, is among oth-

ers accompanied by the emission of X-rays and ends when the particle is absorbed by the nucleus due to weak interaction in case of leptons (e.g. μ^-) or strong interaction in case of hadrons (e.g. antiproton, kaon, pion). The cascade time in an exotic atom is short compared to the particle life time, which makes the X-ray processes observable with spectroscopic tools. Provided the particle is heavier than the electron, several effects causing an energy shift to the lower atomic levels become non-negligible due to its vicinity to the nucleus, such as vacuum polarization or recoil effects. Especially in exotic atoms with a large Z the finite size of the nucleus and in hadronic atoms the finite size of the particle play an important role.

Some examples of exotic atoms are:

- *Muonic atoms* have been valuable tools to test the limits of Quantum electrodynamics (QED).
- With *pionic atoms*, the mass of the pion has been determined with high precision.
- *Hadronic atoms* in general are suitable for the determination of particle masses and to measure magnetic moments with high accuracy. Since the inner atomic orbitals overlap with the nucleus, hadronic atoms are a unique source for studying the strong interaction at low energies.

In hadronic atoms, the energy levels of the particle at low n are additionally shifted from their purely electromagnetic value (including further effects such as vacuum polarization) due to the strong interaction between particle and nucleus. The nuclear absorption terminates the cascade process at an $n > 1$, where the wave functions of the lowest atomic levels already overlap with the nucleus. These states are also broadened with a certain width, caused by the nuclear absorption reducing the lifetime of a state.

2.2 Kaonic helium atoms

2.2.1 Processes in the kaonic helium atom

The kaon is a meson, i.e. a bound state of two quarks, with strangeness $S = \pm 1$. One doublet with strangeness +1 is formed by the K^+ and the K^0 , the other one with strangeness -1 is formed by the antiparticles K^- and \bar{K}^0 . The K^+ ($u\bar{s}$) and its antiparticle K^- ($\bar{u}s$) have a mass of (493.677 ± 0.016) MeV/ c^2 and a mean life time $\tau = (1.238 \pm 0.002) \cdot 10^{-8}$ s [4]. They decay weakly via leptonic, hadronic and semileptonic modes.

A **kaonic helium atom** is formed when an (anti)kaon K^- is captured by a helium atom, having an initial principal quantum number of $n \approx 30$ according to equ. 2.1. The average time of the cascade in liquid kaonic helium was found to last $2 \cdot 10^{-10}$ s [5]. As soon as the cascade starts, the following processes occur [6] (the given rates were calculated by Koike et al. [7]):

- After the capture, the atomic states are populated with preference of higher angular momenta ℓ due to their large multiplicity. This is distorted by Stark mixing, see below.
- The beginning of the cascade process starts via density dependent molecular excitation, dissociation or the external Auger effect.
- The dominant effect in the outer orbits is the internal **Auger process**, with a transition rate of $\Gamma_{Auger} \sim N \cdot \sqrt{2\Delta E}$ (target density N , transition energy ΔE .)
- As soon as all electrons are ejected, **radiative transitions** from $(n, \ell - 1)$ to $(n - 1, \ell - 2)$ begin to dominate with a rate proportional to ΔE^3 .
- An important effect at angular momenta $\ell > 1$ is **Stark mixing**: Small and electrically neutral exotic atoms are close to adjacent atoms which causes due to their electric field a mixing of states of different angular momenta ℓ at a certain principal quantum number n . This has an influence on the X-ray yields [1,8]: due to Stark mixing, the particle (kaon) undergoes nuclear absorption from s states of large principal quantum numbers, which eliminates further radiative transitions to

lower levels. Therefore, the X-ray yield decreases with increasing target density, where the probability for Stark mixing is higher.

- The cascade ends with the absorption of the particle by the nucleus. For details of the interaction with the nucleus, see next section 2.2.2.
- An effect which is usually negligible for heavy particles like kaons is the **Doppler broadening**. This is the broadening of a spectral line due to different velocities of the particle, with a width inversely proportional to the square root of the particle mass.

In kaonic helium, the X-ray yields are additionally suppressed. As reported in ref. [5], the relatively high electron binding energy of ~ 25 eV prevents the emission of an additional Auger electron in circular orbits ($\ell = n - 1$) at high n . For a few percent of the captured kaons, the resulting neutral atom ($K^-e^-He^{++}$) remains in a metastable state where the kaons are trapped and subsequently absorbed or decaying with free life time.

A scheme of the cascade of pionic hydrogen, representative for a typical hadronic atom, is shown in figure 2.1.

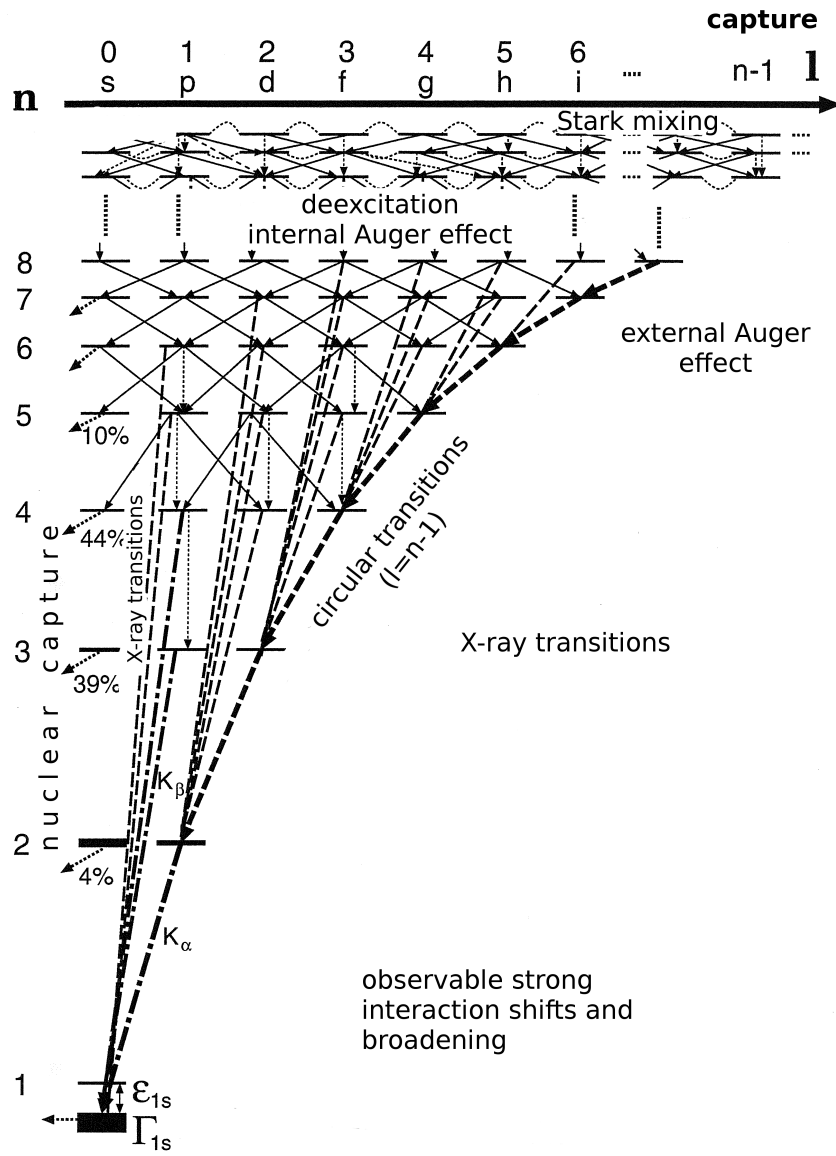


Figure 2.1: Cascade in pionic hydrogen π^-H . The percentage numbers on the left side denote the probability of nuclear capture.

2.2.2 Theoretical framework for the K^- -nucleus interaction

Historically, the investigation of antikaon-nucleus ($\bar{K}N$) interactions by the use of light kaonic atoms became of interest with the idea of kaon condensation in baryonic matter [9]. This may lead to modifications of the K^- mass [10] and to probable effects on the formation of neutron stars.

In principal, the **chiral SU(3) effective field theory**, a low energy realization of quantum chromodynamics (QCD), is the framework for treating hadron-nucleus interactions with strangeness $S = -1$ theoretically [11]. The (optical) potential V describing a hadron-nucleus scattering usually has an attractive real part, representing the binding energy between particle and nucleus, and an absorptive imaginary part, expressed via the decay width. In case of the $\bar{K}N$ interaction perturbative approaches are not applicable due to the isospin-zero s-wave resonance $\Lambda(1405)$, which is formed just below (~ 30 MeV) the K^-p threshold and dominates the interaction. The nuclear potential of the $\bar{K}N$ interaction therefore has a strongly attractive real part in the order of $Re(V) \approx -100$ MeV, allowing the formation of nuclear states, and an equivalently strong absorptive part. The $\Lambda(1405)$ primarily decays via strong interaction into $\pi\Sigma$ ($\bar{K}N \rightarrow \pi\Sigma$), thus the resonance is also considered to be a quasi bound state with isospin $I = 0$ due to the coupling between the $\bar{K}N$ and the $\pi\Sigma$ channels.

Several theoretical models, e.g. a coupled-channel calculation based on the SU(3) meson-baryon effective Lagrangian [12–15], try to calculate the complex potential and to reproduce the $\Lambda(1405)$, the K^-p scattering lengths or the branching ratios. An up to date summary is given in ref. [11] by Weise. The discussion about possible deeply bound kaonic states below threshold, where the real part of the potential is $Re(V) > |-150|$ MeV, was recently resumed [16–18]. However, theoretical extensions to sub-threshold $\bar{K}N$ interaction are manifold [19,20] and in principle limited due to the dominating resonance below threshold.

Particularly in case of kaonic helium, the $\Lambda(1405)$ resonance has to be considered within a multi-body system with the K^- acting as a possible additional binding source between the baryons [11]. The three-body problem is mainly approached via solving Faddeev equations [21,22], or with variational calculations within the $\bar{K}N$ effective interaction. For example, variational calculations by Yamazaki [23] are based on the assumption of K^-p being a bound state, where the resulting nuclear potential has only little energy

dependence and allows large decay widths. Variational calculations with inputs from chiral SU(3) coupled-channel models by Dote [24] obtain a weaker bound K^-pp system with a small binding energy and a small decay width. However, a wide range of calculated binding energies between ~ 20 and 80 MeV and decay widths between 40 and 110 MeV have been obtained for the complex potential of kaonic helium. A realistic description of the nuclear potential in kaonic helium still is a subject of current research since the values of its real and imaginary parts have measurable influences on the atomic states of the atom. This is discussed in the next two sections.

2.2.3 The strong interaction shift in kaonic helium

The nuclear potential of the $\overline{K}N$ interaction, with an absorptive imaginary and an attractive real part of the same order, is not observable directly. On the contrary the strength of the potential influences those atomic orbits where the nuclear states cross the atomic spectrum [25]: The nuclear absorption results in a broadening (**width**) Γ of an atomic energy level, the real part of the potential causes a **shift** ϵ compared to the purely electromagnetic value. In kaonic atoms, the strong absorptive $\overline{K}N$ potential and the influence of the $\Lambda(1405)$ resonance lead to a net repulsive, negative shift of the lower states where the wave function overlaps with the nucleus [26]. Generally, these low-lying states have radiatively suppressed and broad (1 – 10 keV) widths. This limits their observation with spectroscopic tools [27,28]. The nearest higher atomic states, usually playing a minor role, could only be affected by deeply bound nuclear potentials [8,29], where possible large widths and anomalous shifts (i.e. $|\epsilon| > 5$ eV) are predicted [27,30]. In **kaonic helium**, the $1s$ state is strongly influenced by the nuclear potential. The wave function of the kaon in the $1s$ state overlaps with the nucleus resulting in a very broad absorption width, which makes the state hardly accessible with spectroscopical tools. The $2p$ state (a schematic picture is presented in figure 2.2) a fortiori is interesting since the size of a possible shift and width could provide information on the properties of the $\overline{K}N$ potential. In particular, an anomalous large shift would give an indication for deeply bound kaonic states in the nucleus.

Various theoretical calculations of the shift and the width of the kaonic helium $2p$ state have been performed. For spin-zero particles like kaons, the Klein-Gordon-equation is used for calculating the properties of the atomic

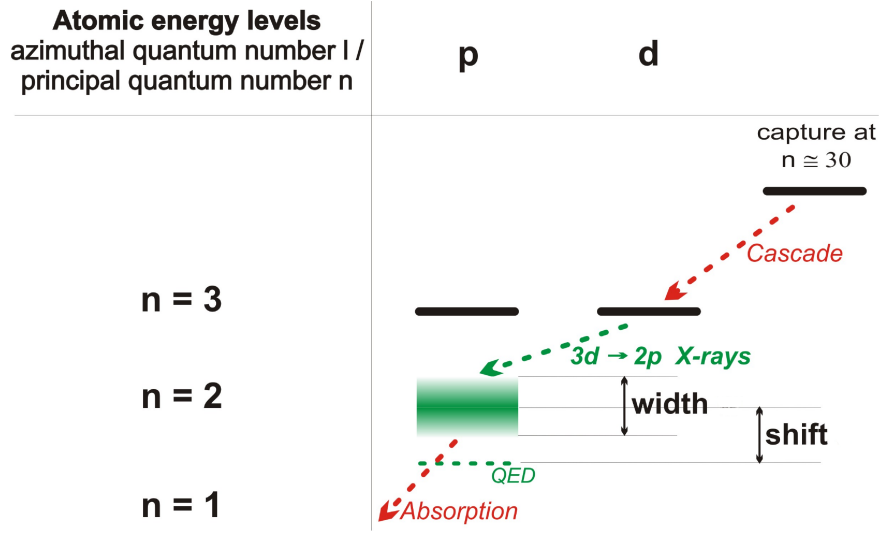


Figure 2.2: Schematic picture of the $3d \rightarrow 2p$ X-ray transition in kaonic helium.

levels (in contrary to fermions, where the Dirac equation is necessary). Since a perturbative approach must be excluded due to the strong influence of the $\Lambda(1405)$ resonance just below threshold, the equation is solved by adding the appropriate short-ranged complex potential to the Coulomb potential [2, 25, 31]. For kaonic helium, this optical potential has been calculated in many ways (see section 2.2.2) and the shift and widths of kaonic atom levels over the whole periodic table have been determined both with around 0 eV [1, 2, 8, 25, 27, 28, 32].

A recent contribution by Akaishi [30] deals with the idea of deeply bound nuclear states in kaonic helium. The realization of the deep nuclear potential with $Re(V) > 200$ MeV is based on a coupled-channel calculation. A $2p$ kaonic nuclear bound state is predicted, leading to a possible anomalous large $2p$ level shift with $|\epsilon| \leq 10$ in ^4He and ^3He and to a difference between the ^3He and ^4He $2p$ level shifts. The calculated shift in ^4He and ^3He by Akaishi as a function of the real part of the nuclear potential is presented in figure 2.3.

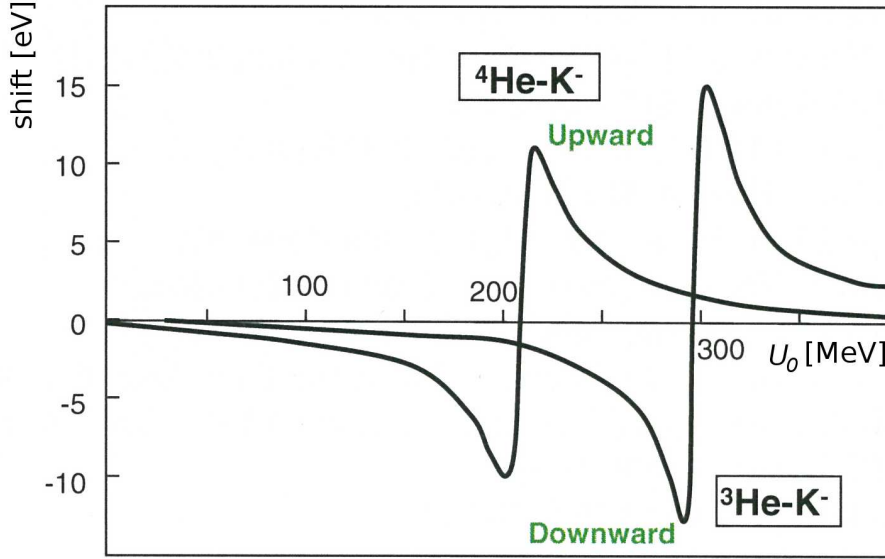


Figure 2.3: A theoretical model of the nuclear potential U_0 in kaonic helium allows anomalous large shifts of the 2p level and isospin differences [30].

2.2.4 The yields in kaonic helium

In hadronic atoms in general, the nuclear absorption of the captured particle at high s -states is enhanced due to Stark mixing, see section 2.2.1. Consequently, the probability of radiative transitions at lower states is decreased which reduces their transition rates. These fluorescence yields are density dependent, because Stark mixing increases with density, when the atoms are closer to the electromagnetic field of their neighbors.

The yields of the investigated transitions, i.e. the number of X-rays emitted via a transition per captured kaon, is an important parameter for spectroscopic experiments with hadronic atoms since the prospective X-ray detection efficiencies and therefore the required beam time can be estimated. The density dependence of the yields also plays an important role for the choice of the target density.

Experimentally, the yields of the atomic states can be calculated from the measured X-ray transitions, provided that the experimental setup dimensions, the detection efficiencies and the kaon production rates are known. Hitherto, the experimentally determined yields in kaonic helium have been known from the experiments on the $2p$ transitions in liquid kaonic ${}^4\text{He}$ per-

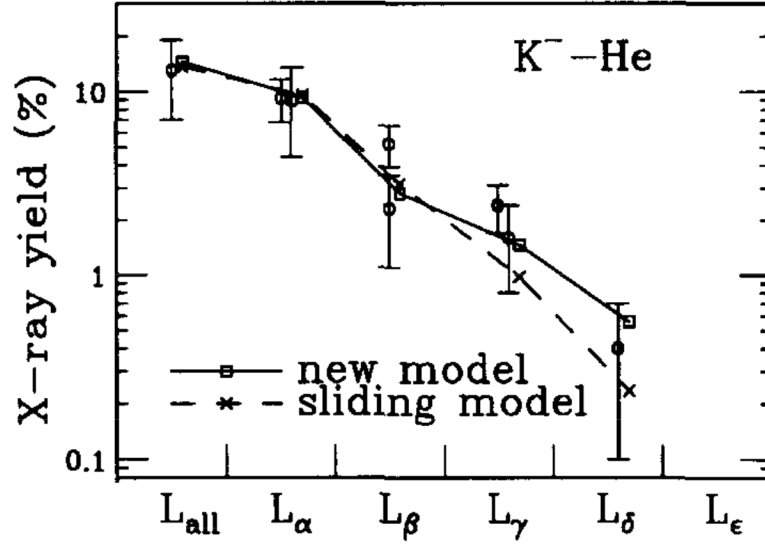


Figure 2.4: Theoretical and experimental yields in liquid kaonic ^4He : Two theoretic models by Koike and Akaishi [39] (lines) are shown, as well as the experimental results of Baird et al. [35] (points). L_i denote the transitions to the $2p$ state from different higher states.

formed between 1971 and 1983 [33–35], which are in the order of 10 % for the $3d \rightarrow 2p$ transition.

Also several theories approach the calculation of the yields in kaonic helium and their density dependence due to Stark mixing, see references [7, 36–38]. The cascade-model by Koike and Akaishi [39] for the calculation of the transition rates in liquid kaonic helium includes the rates of all relevant cascade processes, such as Stark mixing, radiative transition and nuclear absorption. The calculated yields are then obtained via fits to the experimental data on liquid ^4He . This is presented in fig. 2.4, where their results of several transitions to the $2p$ state in liquid ^4He are in good agreement with the experimentally determined yields by Baird et al. [35]. Since there are no experimental results of gaseous helium so far, the determination of the yields in gaseous kaonic helium can give crucial inputs for theoretical models and further experiments on kaonic helium.

2.3 Calculation of the electromagnetic energy levels kaonic helium

The strong interaction shift ϵ of an atomic level is defined as the difference between the energy value arising from influences of the strong interaction and the calculated unaffected energy value. Experimentally, the strong interaction shift of an atomic state therefore is the difference of its measured and its calculated, purely electromagnetic value: $\epsilon = E_{measured} - E_{calc}$. The measurement usually is carried out as a spectroscopic determination of the characteristic X-ray transition to the state of interest. This means in particular for the measured energy of a $2p$ state in kaonic helium:

$$E_{2p,measured}^n = E_{X-ray}(n\ell \rightarrow 2p)$$

and for the calculated energy:

$$E_{2p,calc}^n = E_{calc}(n\ell \rightarrow 2p)$$

with $(n, \ell) > (2, p)$, where all states with $n > 2$ are unaffected by the strong interaction.

The **purely electromagnetic value** of an atomic orbit in an arbitrary kaonic atom is calculated with the relativistic equation for spin zero particles, the Klein-Gordon equation. The Klein-Gordon equation for a free particle is:

$$\left[\frac{1}{c^2} \frac{\partial^2}{\partial t^2} - \nabla^2 + \frac{\mu^2 c^2}{\hbar^2} \right] \psi(t, x) = 0 \quad (2.2)$$

with μ as reduced mass of the kaonic atom, c as the speed of light, \hbar as the reduced Planck's constant and $\psi(t, x)$ as the wave function of the kaon. The stationary solution in a Coulomb field $V(r) = -\frac{e^2}{r}$ gives the following eigenvalues for the energy of an orbit (n, ℓ) :

$$E^{(n,\ell)} = \frac{mc^2}{\sqrt{1 + \left(\frac{Z\alpha}{\eta}\right)^2}} \quad (2.3)$$

with the fine structure constant $\alpha \approx 1/137$ and η as

$$\eta \simeq n - \frac{(Z\alpha)^2}{2\ell + 1} \quad (2.4)$$

Equation 2.3 was used to calculate the purely electromagnetic $2p$ transitions

in kaonic helium. Due to the adjacency of the kaon to the nucleus, effects which shift the lower atomic states had to be taken into account. However, in the first order only the vacuum polarization is not negligible, while other corrections contributing in the order of meV were neglected, like corrections due to the recoil or due to the finite sizes of nucleus and kaon [6, 40]. For the vacuum polarization correction, the solution of a first order perturbative approach in a relativistic framework, the Uehling correction, was taken from reference [41]:

$$\Delta E_{Uehling} = -\frac{\alpha}{\pi}(Z\alpha)^2 \frac{mc^2}{(\eta^2 + (Z\alpha)^2)^{3/2}} \left[\eta K_{2,2\eta}(\kappa) + \frac{2(Z\alpha)^2}{2\eta - 1} K_{2,2\eta-1}(\kappa) \right] \quad (2.5)$$

where κ determines the mass ratio of the kaon in the atom and the electron. The functions $K_{i,j}$, containing the Beta function and generalized hypergeometric functions, are listed in a closed analytic form in ref. [42].

The result¹ for some ${}^3\text{He}$ levels is presented in table 2.1:

	2p [eV]	3d [eV]	4f [eV]	5g [eV]
uncorrected	-11180.1	-4968.8	-2795.0	-1788.7
Uehling correction	-15.4	-1.9	-0.3	-0.1
total energy	-11195.5	-4970.7	-2795.2	-1788.8

Table 2.1: Calculated electromagnetic atomic states in kaonic ${}^3\text{He}$ including the Uehling correction taken from [41].

¹Several calculations have been performed with *mpmath* version 0.17, a python-based mathematics tool by Fredrik Johansson

The X-ray transitions to the 2p level are summarized in table 2.2 for ^3He , calculated as described above, and for ^4He , taken from [43]:

isotope	$3d \rightarrow 2p$ [eV]	$4f \rightarrow 2p$ [eV]	$5g \rightarrow 2p$ [eV]
^3He	6224.7	8400.3	9406.6
^4He	6463.5	8721.7	9766.8

Table 2.2: Calculated electromagnetic X-ray transitions in kaonic helium.

2.4 Recent developments in kaonic helium

There used to be a long standing discrepancy between measured and theoretically predicted shifts of the kaonic helium $2p$ level which was called the **kaonic helium puzzle**. Three spectroscopic measurements on kaonic ^4He , performed between 1971 and 1983 [33–35], obtained an averaged shift of (-43 ± 8) eV for the $2p$ level, while several theories (listed in section 2.2.3) predicted a shift around 0 eV. Fig. 2.5 shows the theoretical result by Hirenzaki et al. [32] (lines) based on the chiral unitary model and the old experimental data (squares) for several kaonic helium atoms. The experimental data fit to the predictions except for the case of helium with $Z = 2$.

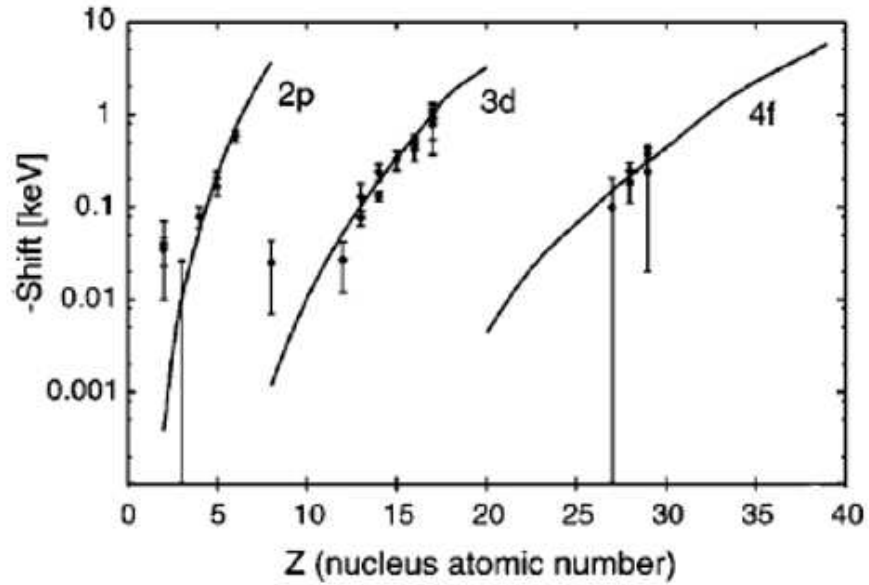


Figure 2.5: The calculated strong interaction level shifts and width for kaonic atoms atoms by Hirenzaki et al. [32] (lines). The shifts of $2p$, $3d$ and $4f$ states of kaonic atoms with different Z are displayed. Note the old experimental data on kaonic helium (squares), giving a large shift of about 40 eV in the $2p$ state.

Motivated by the kaonic helium puzzle and the new theoretical aspects by Akaishi, the precise spectroscopy of kaonic helium X-rays attracted attention in the last years. Two experiments, the E570 experiment at KEK (Japan) in 2007 and the SIDDHARTA experiment at LNF (Italy) in 2009 and 2011, respectively, measured the $2p$ level strong interaction shift via a spectroscopy of the X-ray transitions in ^3He and ^4He . The main difference between these two experiments is the helium target density: In the E570 experiment, liquid ^4He was used, while the SIDDHARTA experiment used gaseous ^3He and ^4He , both with different densities. The advantages over the liquid target are the higher yields of the atomic states in gaseous helium due to the density dependent Stark mixing (see section 2.2.1), and the suppression of background arising from Compton scattering.

Both experiments obtained a strong interaction shift of the $2p$ level of averaged 0 eV in ^3He and ^4He , which solved the puzzle in favor of the theoretical predictions. However, the statistical range of these experimental results permits a shift of up to 10 eV within a confidence level of 95 % which could be an indicator for deeply bound kaonic states. The existence of a possible isospin dependence of the shift within a few eV is also not resolved yet. Therefore, an experiment on ^3He and ^4He with a high measurement precision is needed. It is important to mention that the work for this thesis contributes to the SIDDHARTA experiment in the analysis part and to the E17 experiment in the experimental part.

In the following, a short description of the recent experiments is given:

- **Liquid ^4He with E570:** The E570 experiment, performed at KEK (Tsukuba, Japan) in 2005, solved the kaonic helium puzzle by determining the $2p$ level shift in super fluid ^4He to $\epsilon_{liquid}^{4He} = (2 \pm 2(stat.) \pm 2(sys.))$ eV [43], consistent with the theoretical predictions. A secondary beam of K^- with a momentum of 650 MeV/c produced by the proton beam from the 12-GeV proton synchrotron was guided to the experimental setup and stopped in a cylindrically shaped target cell containing liquid ^4He . The accuracy was mainly reached with three features: a) the use of silicon drift detectors, in total covering an area of 8 cm² and optimized for X-ray spectroscopy in the relevant energy range, b) suppression of background events due to kaon stops outside the target by tracking the incoming kaons and the outgoing

secondary charged particles and c) a simultaneous detector calibration with characteristic X-rays from metal foils excited by charged particles contaminating the kaon beam. A picture of the target system is presented in figure 2.6.

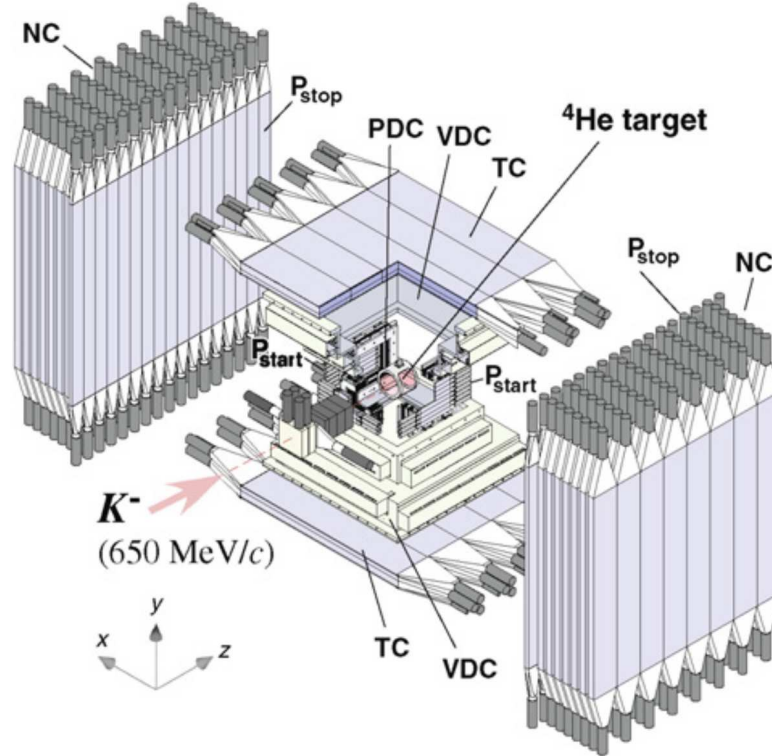


Figure 2.6: Sketch of the E570 setup at KEK. Picture from [?].

- **Gaseous ^4He with SIDDHARTA:** The SIDDHARTA experiment took place at the DAΦNE e^+e^- collider at LNF in Frascati, Italy. A Φ -meson with a mass of $m_\Phi = 1020$ MeV is produced, which decays into a K^+K^- pair. The monochromatic low-energy K^- with a momentum of ~ 150 MeV/c are stopped in a cylindrical target cell filled with gaseous helium. Similarly to E570, the usage of silicon drift detectors (144 cm^2) and a suppression of kaon-uncorrelated background

events lead to a high precision. The detector calibration via characteristic X-rays was done periodically between the data taking process. A detailed description of the setup and of the analysis is given in chapter 4. Consistent with E570, a shift of $\epsilon_{gaseous}^{4He} = (0 \pm 6(stat.) \pm 2(sys.))$ eV [44] was obtained.

- **Gaseous ^3He with SIDDHARTA:** With the same setup used for the ^4He measurement, the shift of gaseous ^3He was determined to $\epsilon_{gaseous}^{3He} = (-2 \pm 2(stat.) \pm 4(sys.))$ eV [45]. Although this is within errors consistent with the result for ^4He , the question for possible differences between ^3He and ^4He is still not solved.
- **Liquid ^3He and ^4He with E17:** The E17 experiment, to be performed at J-PARC, Tokai (Japan) in 2012, is designed to measure the shift of the kaonic helium $2p$ state with a precision of less than 2 eV and approach a probable isospin dependence of the shift. The setup, on the base of the E570 setup, and the facility are described in chapter 5. Two key issues to reach this precision are presented in this thesis: First, the investigation of the response function of the silicon drift detectors used in the experiment, see chapter 3 and second, an estimation of the kaonic helium yields based on the results of SIDDHARTA which allows to assess the prospective X-ray detection efficiencies.

Chapter 3

Silicon drift detectors for X-ray spectroscopy

3.1 Introduction

Semiconductor detectors have been successfully used in a wide range of particle detection and spectroscopy applications for several decades due to the simplicity of their handling and production. The basic principle, namely to fully deplete a semiconductor and to collect the produced charge carriers when an incoming particle ionizes the material after passing through, has been continuously enhanced and optimized to the according requirements. Silicon drift detectors (SDDs) in particular were initially constructed by Gatti and Rehak [46,47] in 1984 as large area position sensitive semiconductor drift chambers (for a schematic view, see figure 3.1). They developed a new scheme based on the principle of sideways depletion, where the transport of charge carriers produced by a hitting particle became independent of the depletion voltage. A full depletion of an n-type silicon wafer is achieved through a small contact placed on an edge, while the charge transport to the collecting anode is provided by a superposed potential valley, applied via a strip array of p-type silicon junctions on the rear and the front side. Due to a small anode, the capacitance and therefore the leakage current and the noise level are drastically reduced compared to former parallel micro strip detectors.

An optimization of this principle for determining a particle's energy was developed a few years later by Rehak and Kemmer [48, 49]. Instead of precisely aligned p-type silicon patterns on both sides, a planar p-n junction on the front side (acting as entrance window) and a p-type pattern on the rear side have been implemented.

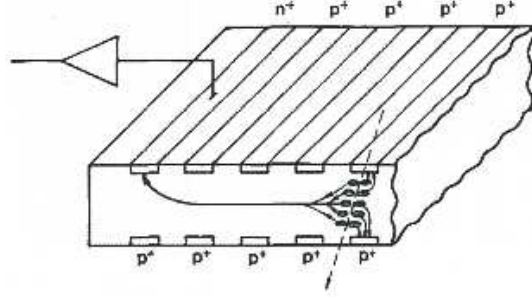


Figure 3.1: Working principle of a position sensitive drift chamber, proposed by E. Gatti and P. Rehak. Picture taken from [47].

The pattern provides, similar to the former model, a linear voltage drop between the p-type stripes, generating the drift field for the electrons.

Further developments in SDD design, optimized for X-ray applications (by Lechner [50, 51]), lead to a cylindrical shaped detector with a small centered anode. The externally biased inner and outer guard rings provide the drift field via an internal voltage divider. For amplification, a field effect transistor (FET) is mounted closely to the anode. The small value of the capacitance of the anode leads to a large amplitude and a short rise time of the output signal. The SDDs can be operated at high count rates and, even at room temperature, a good energy resolution is achieved. A picture of the new design (figure 3.2, left side) and of the calculated potential valley (figure 3.2, right side) is presented.

The SDDs used in SIDDHARTA and E17 are squared and hexagonally shaped, respectively, each with an area of 1 cm^2 . With a thickness of $450 \text{ }\mu\text{m}$ they are well suited for X-ray spectroscopy up to 20 keV . A model of an E17-SDD is shown in figure 3.3, which can be understood similarly for a SIDDHARTA-SDD. In both cases, the drift field is built up by the bias voltages V_{R1} (around -10 V) and V_{RX} ($> -100 \text{ V}$), both applied to the voltage divider on the rear side, and V_{BACK} ($< -100 \text{ V}$) which is applied to the contact of the front side. Since these three voltages are biased externally, the drift field for each device can be adjusted and optimized separately (for details, see section 3.3 and section 3.4).

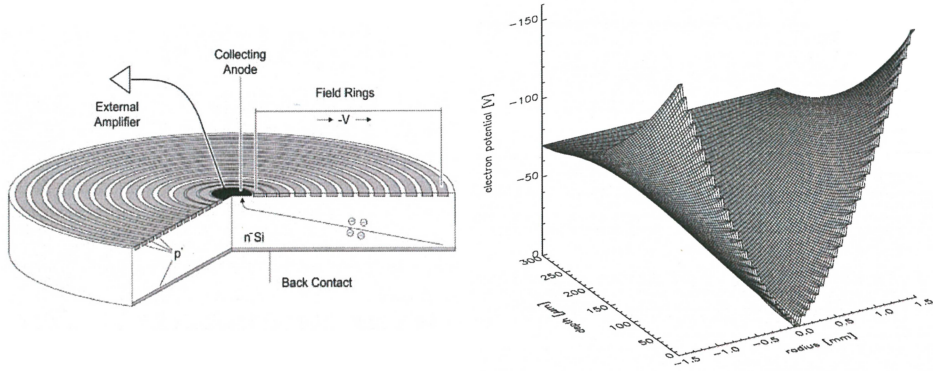


Figure 3.2: Left: Cylindrical SDD proposed by [51], where the charge carriers are guided by a drift field to the anode. Right: Calculated drift field with the anode represented by the lowest point of the potential.

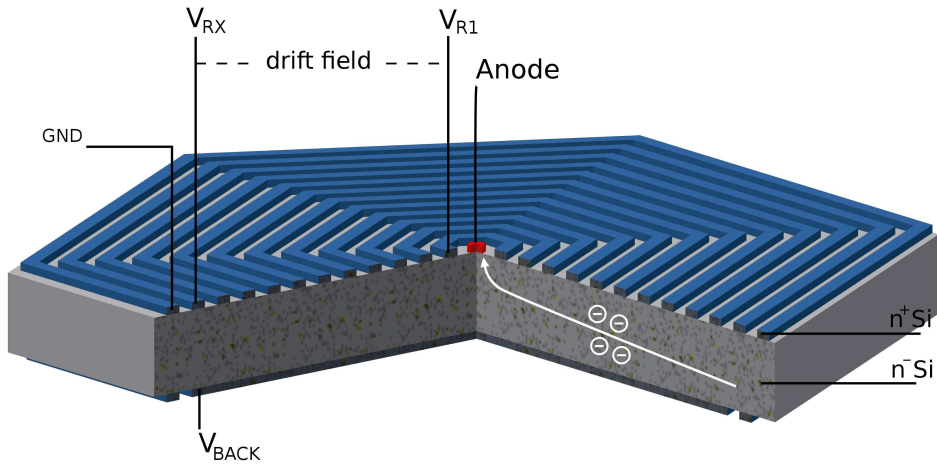


Figure 3.3: Model of an E17-SDD: When an X-ray hits the SDD from the front side (bottom), the generated charge carriers are guided by the drift field to the centered anode. The drift field is built up by the voltages V_{R1} and V_{RX} , applied to the inner and outer ring on the rear side, respectively, and by V_{BACK} .

3.2 Working principle and response function of an SDD

The processes which are followed by an X-ray hitting an SDD are in detail described in references [52–54]. A short overview is given in the following: After an incoming X-ray interacts with one silicon atom in the bulk of the SDD, a photo electron is produced which generates further electron-hole pairs forming a charge cloud. The primary electrons, containing the subsequent Auger and Photo electrons, produce secondary electrons by ionization until their kinetic energy is smaller than the ionization threshold. The total energy of an X-ray is therefore transformed into an equivalent number of charge carriers n_{e-h} (i.e. electrons):

$$n_{e-h} = \frac{E_{X-ray}}{\omega} \quad (3.1)$$

with ω as the electron-hole pair creation energy, which is 3.7 eV for silicon at 300 K [55].

The electrons travel along the drift field to the anode (see figure 3.3) where they are finally amplified by a FET and an output signal is created. Ideally, all electrons are produced in the silicon bulk and collected by the anode. Charge loss mainly comes from processes in the entrance window which is defined as the sum of the metalization zone and this part of the silicon layer, where incomplete charge collection (ICC) occurs. Electrons may also be lost when they escape the silicon or due to impurities and defects in the material which can usually be neglected.

In an energy spectrum of a characteristic X-ray line, the majority of the detected X-rays contributes to the **main peak**. This peak actually is a convolution of the *intrinsic Lorentzian distribution* of the X-ray line (e.g. the natural width of the Mn- $K_{\alpha,1}$ line is 1.43 eV) and of the Gaussian shaped *detector response function*, [56, 57]. For the requirements of this thesis, the natural width of the peaks can be neglected and only the Gaussian function is used to reproduce an X-ray peak. The width of the response function is determined by the quadratic sum of all contributions, which are the electronic noise of the detector and the amplification stages, σ_{el} , and the statistical

fluctuation of the created electron-hole pairs σ_{stat} :

$$FWHM_{main-peak} = 2.35 \cdot \sqrt{\sigma_{el}^2 + \sigma_{stat}^2} \quad (3.2)$$

The electronic noise can be reduced, for example by changing geometric parameters or materials [58]. The statistical fluctuation of the number of the created electron-hole pairs n_{e-h} (see equ. 3.1) is not purely poissonian and dependent on detector material properties which is represented by the Fano factor F (≈ 0.1 for silicon [55]). From equations 3.1 and 3.2 follows:

$$FWHM_{main-peak} = 2.35 \cdot \sqrt{\sigma_{el}^2 + \omega \cdot E \cdot F} \quad (3.3)$$

The **flat shelf** on the low energy side of the main peak and the **low energy tail** of the main peak arise from lost electrons due to the charge collection processes. The latter is not only dependent on detector properties but also on the drift field and drift pathes in the silicon. Since the drift field in an E17-SDDs and SIDDHARTA-SDDs can be adjusted externally (see section 3.1), the tails and low-energy signals due to lost events can be reduced by a proper choice of the bias voltages.

In X-ray spectra, the **escape peak** arises from K shell electrons escaping the detector material. It is located at an energy of $E_{escape} = E_{main-peak} - E_{K_\alpha}^{detector-material}$, with E_{K_α} in silicon at 1.74 keV.

In figure 3.4, the characteristic X-ray spectrum of an ^{55}Fe -source monitored with an E17-SDD is shown. According to ref. [57], the Mn- K_α main peak is represented by a Gaussian function, the low energy side was fitted among others with an exponential and a shelf function.

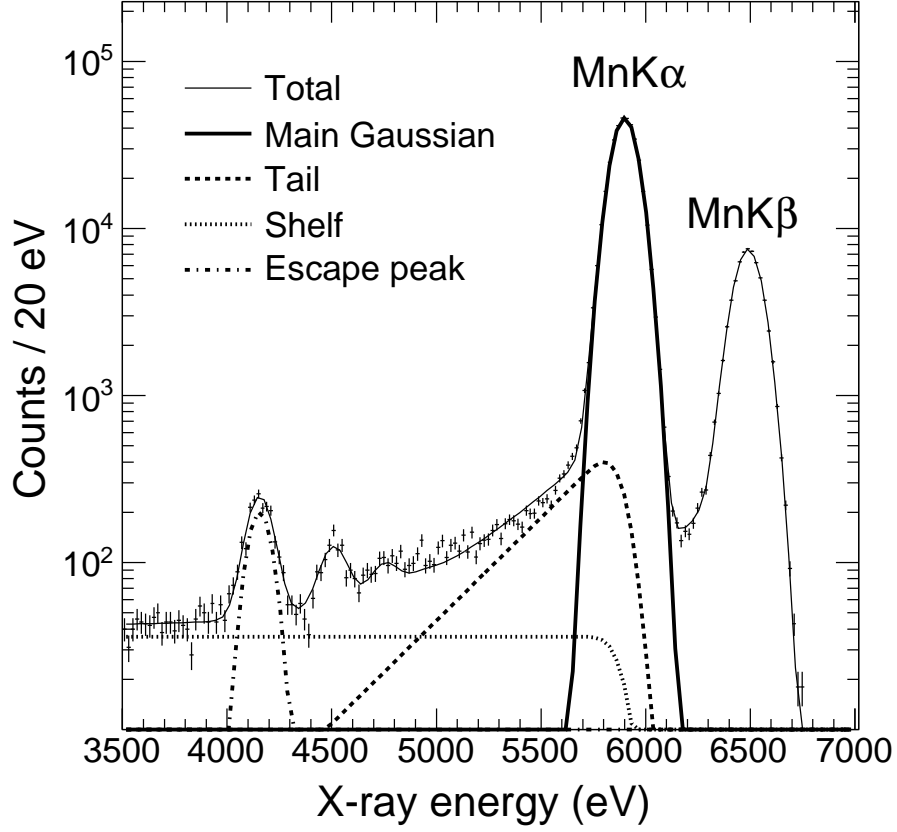


Figure 3.4: Characteristic X-ray spectrum of Mn (fits according to [57]), with the majority of X-rays contributing to the main Gaussian peak.

3.3 SDDs for SIDDHARTA

The X-ray spectroscopy of the kaonic helium X-ray transitions in SIDDHARTA was performed with special developed large area SDDs with integrated FET [59]. The SDDs, their readout circuits and preamplifiers were developed partially within the project "Joint Research Activity JRA 10" of the I3 project "Study of strongly interacting matter (Hadron-Physics)" of the EU, together with the Halbleiterlabor in Munich and the Politecnico Milano group [60]. The ceramic material on which the SDDs are glued was chosen carefully, in order to avoid disturbing fluorescence lines of the ceramic in the region of interest [61].

Altogether 144 SDDs with a common power supply were used for the measurement. Each SDD has its own preamplifier. Three SDD cells are sharing one chip, each with a thickness of $450\text{ }\mu\text{m}$, an area of 1 cm^2 and kept at a temperature of $(170 \pm 0.5)\text{ K}$. A schematic picture of one chip is presented in figure 3.5, left, a model of the final arrangement which surrounds the target cell is shown in figure 3.5, right. An externally generated reset pulse was used for all SDDs in order to induce the discharging process of the FETs simultaneously.

In advance, the bias voltages V_{R1} , V_{RX} and V_{BACK} of all SDDs were adjusted in order to receive a minimum energy resolution. Note that due to the triple-SDD structure only V_{BACK} can be varied separately for each SDD cell, while the other two voltage values influence one whole chip. For all SDDs, an energy resolution of 140 eV FWHM at 5.9 keV has been reached [59].

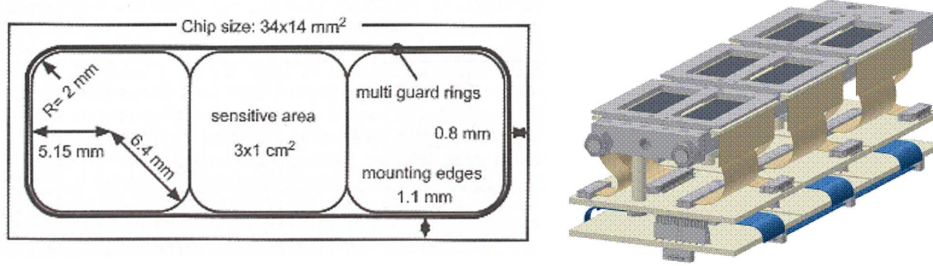


Figure 3.5: Left: Schematic picture of an SDD chip used for SIDDHARTA containing three SDD devices, each with an area of 1 cm^2 (picture from ref. [62]). Right: Model of the SDD arrangement surrounding the target cell.

3.4 SDDs and preamplifiers for E17

In the J-PARC E17 experiment, SDDs are used to measure kaonic helium X-ray transitions with an accuracy of better 2 eV at 6.2 keV . To fulfill this goal, good energy and time resolutions for all SDDs are required. Eight hexagonally shaped SDDs made by KETEK¹ with a thickness of $450\text{ }\mu\text{m}$ and an active area of 1 cm^2 will be used for the measurement. The FET is installed very close to the anode.

¹Type Vitus-SDD

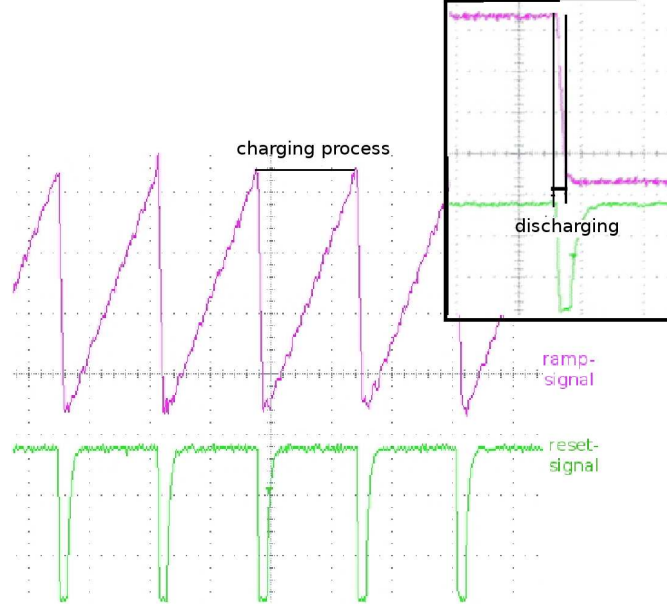


Figure 3.6: Signal of a 4 Volt preamplifier ramp cycle (magenta) and the corresponding reset signal (green). One period of the ramp signal is in the range of a few hundreds of milliseconds without any radiation hitting the detector.

The SDD's corresponding charge-sensitive preamplifiers made by KETEK² generate a sawtooth shaped output signal (*ramp signal*) during their charging and discharging cycle, see figure 3.6. The slope of the rising edge is increased when radiation causes additional charge collection in the SDD. The discharging process is initiated as soon as a certain adjustable voltage threshold is reached. The preamplifiers were equipped with an additional circuit generating a logical *reset signal* which discharges the FET on the SDD and - in order to optimize the performance of the preamplifier - interrupts the data taking process during the discharging process.

²reset type "EPCB-VRPA-S"

In the E17 setup, the SDDs will be installed close to the target cell covering a large solid angle and operated at a temperature of around 130 K in order to reduce thermal radiation to the helium target (kept at 1.4 K). Due to space limitations of the experimental setup the preamplifiers have to be installed inside the vacuum chamber, connected via cables of ≈ 30 cm length to the SDDs. Under this conditions, the response of SDDs is poorly known. Therefore, a study of the SDDs' response on temperature is required before installing the devices into the E17 setup. These studies were performed in a laboratory at the KEK facility, Tsukuba (Japan) and are part of the thesis. They are presented in the following section 3.5, a summary is reported in [63].

3.5 Temperature studies with E17-SDDs

For the temperature studies, ten SDDs and twelve preamplifiers were available. Since no effective differences between the individual SDDs or preamplifiers were observed, the presented measurements resulting from various combinations can be taken representative for a typical SDD-preamplifier-pair.

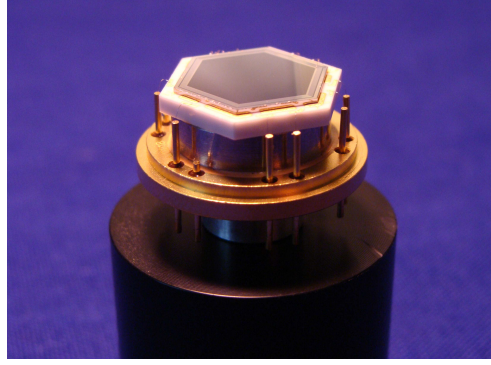


Figure 3.7: Picture of an SDD used for E17, mounted on an aluminum bracket.

In the preparatory stage, a fine tuning of the bias voltages was performed in order to find optimum voltage values providing best achievable energy resolution. The bias voltages were adjusted externally via cables, allowing a measurement of the energy resolution dependence on the bias voltages without removing the SDDs from the vacuum chamber. The following values were kept for all SDDs and all further measurements: $V_{RX} = -130$ V, $V_{R1} = -20$ V, $V_{BACK} = -80$ V (see figure 3.3 in section 3.1).

Also the voltages defining the shape of the preamplifier ramp cycle were adjusted to the measurement conditions, since the behavior of the ramp is dependent on the SDD and the preamplifier temperatures. The regularization of these voltages has to be done directly on the preamplifiers at room temperature, thus an in-situ adjustment was inhibited.

3.5.1 Experimental setup

The vacuum chamber for the measurements is schematically presented in figure 3.8. A copper cold finger (temperature ~ 80 K) was connected conductively to a tank filled with liquid nitrogen (at 77 K). One aluminum housing containing two SDDs and one containing a preamplifier were mounted on the cold finger. The SDD housing, in which SDDs were fixed on aluminum brackets, was placed very close (~ 5 mm) in front of a $100\text{ }\mu\text{m}$ thick Mylar window. A preamplifier was connected via cables with a length of ~ 30 cm to an SDD. Depending on energy or time resolution studies, an X-ray source

(^{55}Fe) or an electron source (^{90}Sr), respectively, was placed outside in front of the Mylar window and aligned to the detectors.

Temperature sensors (PT100) were glued on a chip of each preamplifier as well as on each detector bracket, close to the SDD. Since detectors are connected conductively via aluminum screws to their brackets, the temperature obtained by those sensors can be taken as the temperature on the device. Also heaters for temperature control were placed on each SDD bracket and on each preamplifier. The temperatures on preamplifiers and SDDs could be controlled and optimized separately.

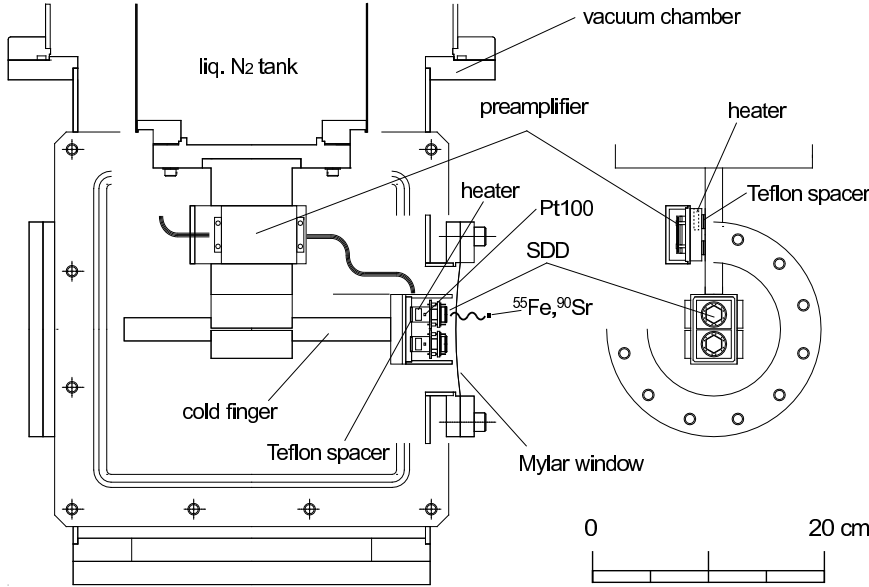


Figure 3.8: Schematic picture of the chamber from side view (left) and front view (right). For details, see text.

3.5.2 Data acquisition

For the studies of the SDDs' energy response an ^{55}Fe source was used. The signal, generated by the FET, gained a first amplification in the preamplifier. The height of the corresponding Gaussian signal, provided by a shaping amplifier³, was measured with an ADC⁴. A scheme of the logic circuit is shown in figure 3.9. The energy resolution of the The Mn- K_α X-ray peak was taken

³CAEN N568b, shaping time 3 μs for X-ray studies and 0.2 μs for drift time studies

⁴TKO Peak Hold ADC, 12 bit, range 2.5V

as FWHM of the Gaussian fit of the main peak (fits according to ref. [57], see section 3.2). A typical energy spectrum of an ^{55}Fe source with an X-ray peak having an energy resolution of 150 eV (FWHM) was already presented in figure 3.4, obtained with an E17-SDD at 130 K and a preamplifier at 280 K.

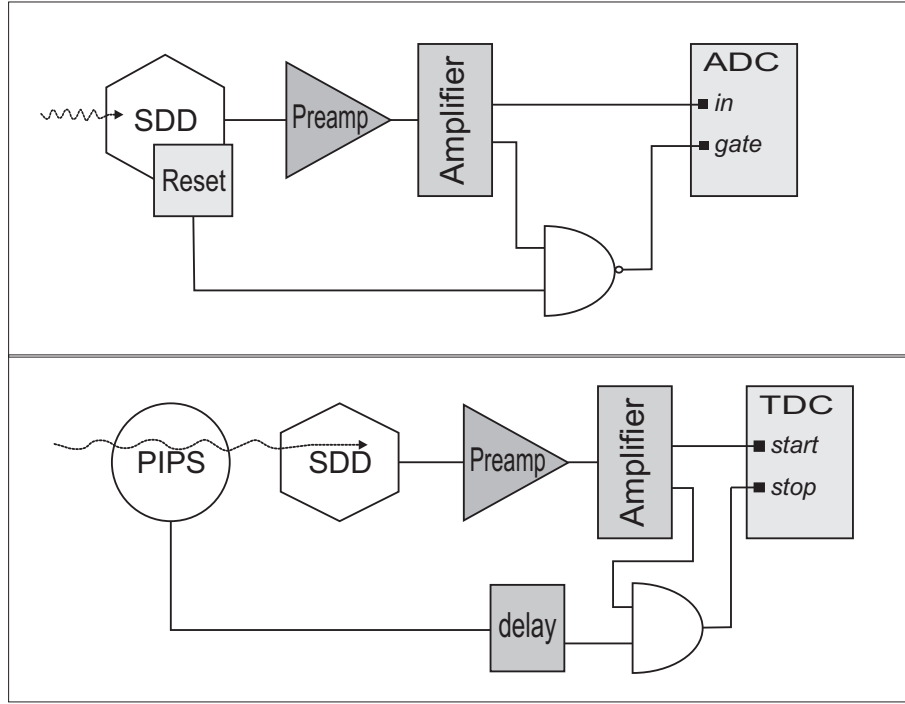


Figure 3.9: Top: Logic scheme of an X-ray measurement where the reset signal gives a veto for the data collection process. Bottom: Scheme of the coincidence measurement. The veto of the reset is not drawn.

For the studies of the SDDs' drift time distribution, a coincidence measurement with a PIPS detector (Passivated Implanted Planar Silicon detector⁵) and an SDD was arranged. These silicon detectors have a thickness of 500 μm , an active area of 300 mm^2 , an excellent time resolution of ~ 50 ns FWHM at 300 K and they are optimized for charged particle detection at high rates. In the setup, the PIPS detector was kept at room temperature, positioned between the window and the radiation source. Due to their high rate, electrons from a ^{90}Sr source were used, permeating first the PIPS and

⁵Canberra, FD300 Series

then the SDD. A leading-edge discriminator was used as input for the TDC⁶ signal, where the time difference between an electron event of the PIPS and of the SDD was recorded. A scheme of the logic circuit is shown in figure 3.9. Because the TDC signals are energy dependent due to processes in the discriminator, a so-called *slewing correction* had to be applied to the TDC events. This complex phenomenon and the correction procedure are a major concern in the SIDDHARTA data evaluation, thus for a detailed description it is referred to section 4.5. Two slewing corrected time spectra of an SDD are presented in figure 3.10.

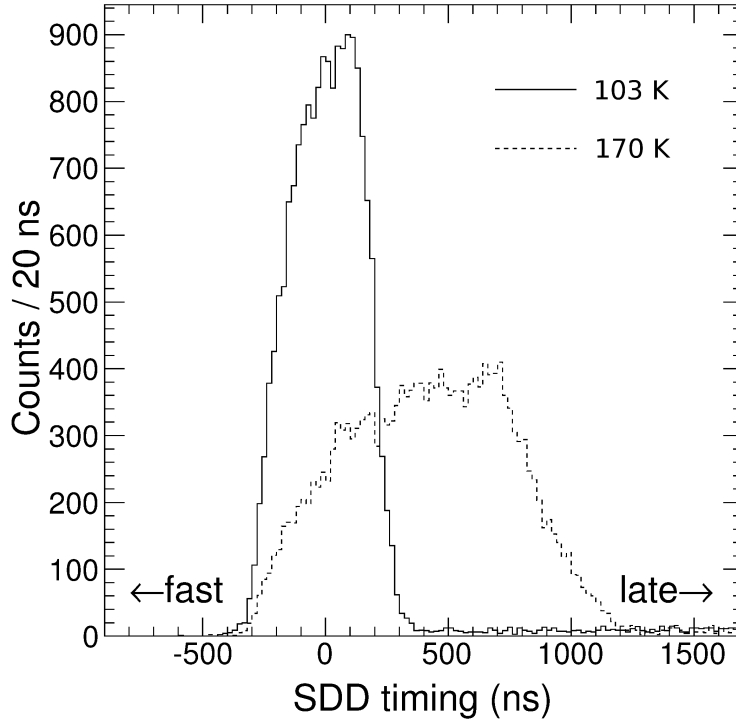


Figure 3.10: TDC spectrum of the coincidence signal from PIPS detector and SDD at 103 K (solid line) and 170 K (dashed line), obtained with electrons from ^{90}Sr . Preamplifier temperature: 280 K.

The peak of the coincidence signal in figure 3.10 is a convolution of all contributions, i.e. of the time resolution of the PIPS detector and of the drift

⁶TKO TDC, 12 bit, range 5 μs

time distribution of the SDD. For the determination of their FWHM, both distributions can be approximated with Gaussian functions. The FWHM of the drift time distribution of the SDD, denoted as Δt_{SDD} , was taken as a quantitative measure, extracted from:

$$\Delta t_{meas} = \sqrt{\Delta t_{SDD}^2 + \Delta t_{PIPS}^2} \quad (3.4)$$

where Δt_{meas} stands for the FWHM of the measured coincidence signal and Δt_{PIPS} for the FWHM of the time resolution of the PIPS detector.

In E17, the SDDs are used for the detection of low-energy X-rays, while their drift time distribution was studied with high-energy electrons. Since charged particles and X-rays underlie different interaction processes with the silicon atoms in the detector, their influences on the shape of the drift time distribution have been studied with data collected by SIDDHARTA, where similar SDDs have been used. The drift time distributions of X-ray events in the SIDDHARTA spectra have been compared to the drift time distribution of background signals in the same energy region, which mainly arise from high energy particles like electrons. No significant differences between their widths was observed. This can be attributed to the area-covering irradiation of the detector: The SDD's drift time distribution is the sum over all drift times of the charge carrier tracks inside the silicon wafer, created by the ^{90}Sr -electrons which *uniformly* permeate the detector surface. This means, that possible differences in the widths of the drift time distributions between X-rays and electrons only affect the local charge carrier production and are negligible in the summarized distribution. Therefore, ^{90}Sr -electrons are an effective tool to study the drift time distribution of an SDD.

3.5.3 Temperature dependence of preamplifier properties

Because the preamplifiers were used in vacuum, the influence of different preamplifier temperatures on the energy resolution and X-ray peak positions was determined.

The dependence of the Mn- K_α line peak positions on the preamplifier temperature is shown in figure 3.11(a). A linear negative shift of 0.5 eV/K within a temperature range from 260 K to 285 K was obtained. The preamplifier temperature has therefore to be controlled better than 1 K in order to keep

the peak center stable within 1 eV. Furthermore, below preamplifier temperatures of 270 K, the functionality of the preamplifier is reduced, resulting among others in random oscillations of the output signal. All preamplifiers were therefore kept at temperatures above 270 K. The energy resolution in turn, presented as a function of preamplifier temperature in figure 3.11(b), shows no observable effect. The variations of energy resolution are within statistical fluctuations between 260 K to 290 K.

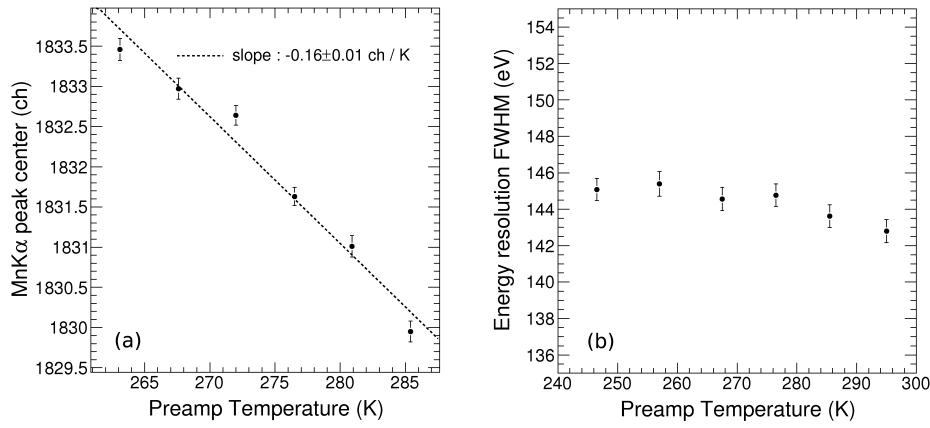


Figure 3.11: (a): Peak center shift in units of channels. The linear effect of 0.16 channels per Kelvin corresponds to a shift of 0.5eV/K. (b): Energy resolution at 5.9 keV as a function of preamplifier temperature. Statistical error bars are shown.

3.5.4 Temperature dependence of SDD properties

The energy resolution of SDDs was studied between SDD temperatures from 100 K to 200 K. The squares and the left axis in figure 3.12 correspond to the energy resolution at 5.9 keV with statistical errors. The energy resolution improves with increasing temperature up to about 130 K, while above 130 K it is constant with an optimum value of about 150 eV (FWHM). The occurring noise causing a worse energy resolution below 130 K is attributed to operation limits of the FET.

The FWHM of the drift time distribution of an SDD, Δt_{SDD} , was measured as a function of its temperature, presented on the right axis (circles) in figure 3.12. This temperature behavior was investigated by comparing the drift time distribution to the electron mobility in silicon. According to ref. [64], the electron mobility in silicon is proportional to the temperature by T^{-n} ,

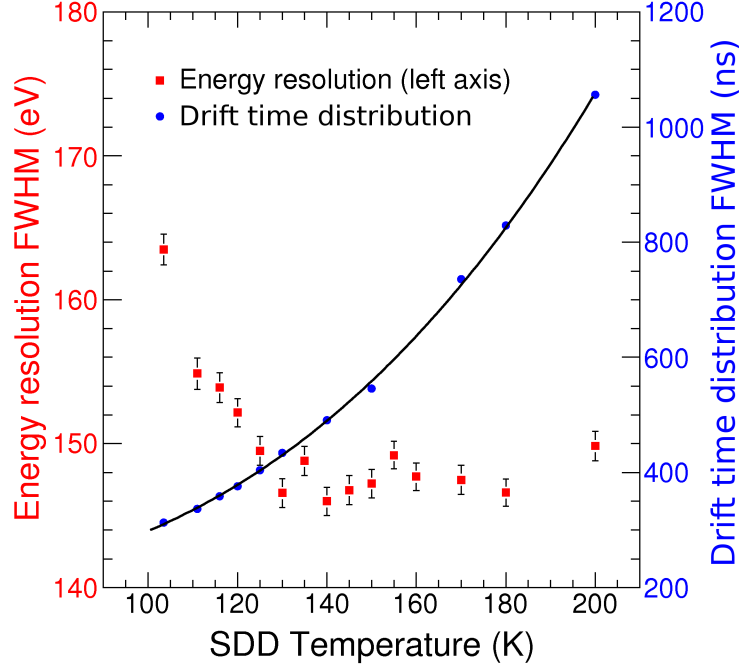


Figure 3.12: Energy resolution in eV (squares) and drift time distribution in ns (circles) vs. temperature on SDD, while the preamplifier was kept at 280 K. The fit corresponds to a T^n function, for details see text.

with $n \approx 2.5$ for temperatures between 100 K and 300 K. It is furthermore inversely proportional to the electron drift time, thus the values for Δt_{SDD} were fitted with a T^n function (solid line in figure 3.12):

$$\Delta t_{SDD}(T) = a \cdot \left(\frac{T}{T_0}\right)^n + b \quad (3.5)$$

with $T_0 = 300$ K. The fit gives for the free parameters $a = (2942 \pm 63)$ ns and $b = (190 \pm 6)$ ns. Close to the published value of 2.5 [64], for n a value of $n = (3.00 \pm 0.06)$ is obtained.

The meaning of the parameters a and b becomes evident by a simple model of an SDD, presented in the following. For the sake of simplicity a two-dimensional and circular-shaped SDD with radius R and an applied drift field E is assumed. The drift velocity of the created electrons, v , is on the one hand the ratio of their drift paths in the SDD to their drift times. On the other hand, the electron drift velocity and the electron mobility μ are

related via the drift field E :

$$v = E \cdot \mu \quad (3.6)$$

The difference between the maximum and the minimum electron drift time is taken as a measure for the width of the drift time distribution Δt_{SDD} . For the relation of drift time distribution and electron mobility follows, with R as the maximum drift path:

$$\Delta t_{SDD}(T) = \frac{R}{\mu(T) \cdot E} \quad (3.7)$$

Including the T^{-n} temperature dependence of μ one gets:

$$\Delta t_{SDD}(T) = \frac{R}{\mu_0 \cdot E} \cdot \left(\frac{T}{T_0}\right)^n + c \quad (3.8)$$

with μ_0 as the electron mobility at the reference value T_0 and c as a constant. In comparison with equation 3.5, it shows that the constant a includes geometrical characteristics of the detector, the electrical field and material properties.

The electron mobility of silicon at 300 K can now be estimated with equations 3.5 and 3.8. In the E17-SDDs, the maximum drift path is $R = 0.62$ cm. The drift field is assessed as the difference between the outer and inner bias voltage, which is around 100 V. With this simple model, an electron mobility of about $\mu_{model} = 1200 \text{ cm}^2\text{s}^{-1}\text{V}^{-1}$ is obtained, which is close to the literature value: $\mu_{lit} \approx 1400 \text{ cm}^2\text{s}^{-1}\text{V}^{-1}$ at 300 K in silicon.

The Mn- K_α peak center was plotted as a function of the SDD temperature in figure 3.13. Below 130 K the peak positions are constant in temperature. Above 130 K the peak position increases linearly with temperature. A slope of 0.19 channels/K corresponding to 0.6 eV/K is found.

This temperature dependence can be explained with the electron-hole pair creation energy in silicon, which effects the number of created electrons and therefore the measured signal in the ADC. According to Mazziotto et al. [55] the electron-hole pair creation energy in silicon decreases with 10^{-4} eV per Kelvin. The electron-hole pair creation energy is inversely proportional to the number of created electron-hole pairs, which was already discussed in section 3.2, equ. 3.1. Since the number of charge carriers determines the height of the output signal measured with the ADC, the X-ray peak centers

in the spectra thus are also shifted with increasing temperature by a factor of 10^{-4} of the incident X-ray. This is consistent with the measured peak shift of 0.6 eV/K corresponding to 10^{-4} of the X-ray energy (5.9 keV) per Kelvin.

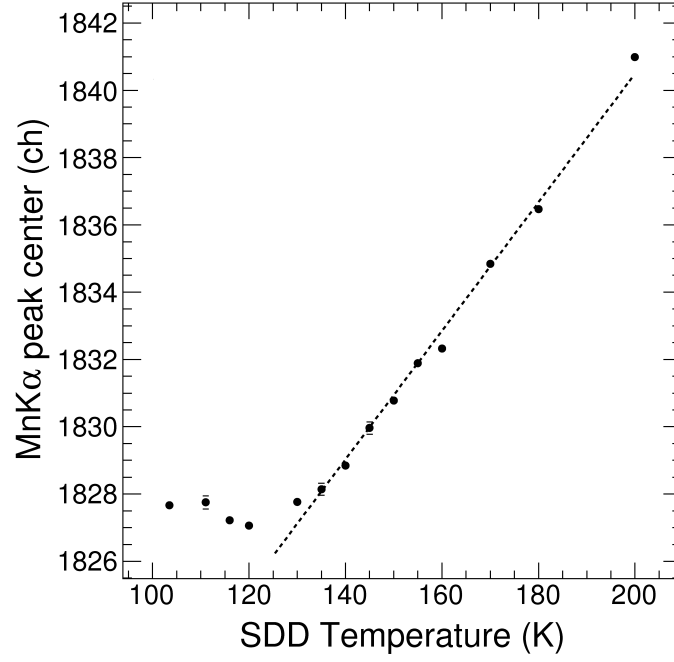


Figure 3.13: Mn-K α peak center as a function of SDD temperature (preamplifier temperature: 280 K). The linear shift occurring above 130 K and represents the temperature behavior of the electron-hole pair creation energy in silicon [55].

3.6 Summary and comparison

The E17-SDDs produced by KETEK and the purpose-built SIDDHARTA-SDDs are identical in their working principle, they have the same absorption depth of $450\ \mu\text{m}$, the same surface area of $1\ \text{cm}^2$ and they are optimized for the spectroscopy of low energy X-rays at high rates. The SIDDHARTA-SDDs have an integrated FET which is discharged periodically via an external reset pulse, simultaneously for all used SDDs during the experiment. The FETs of the E17-SDDs are mounted close to their anode, they are discharged separately for each SDDs via a reset pulse from their preamplifiers. In both cases, an adjustment of the bias voltages of all SDDs has been performed in the preparatory stage in order to reach an optimum energy resolution. In contrary to the SIDDHARTA-SDDs, the single-type construction of the E17-SDDs allows a separate fine tuning for each detector, which is necessary in that case to reach the required precision of $< 2\ \text{eV}$.

In both experiments, SIDDHARTA and E17, the timing information of the SDDs is used to reduce background by selecting the relevant X-ray events from the SDDs' drift time distribution. Because this distribution is dependent on the geometrical properties of an SDD, the differences in the surface area shapes of the two SDD types appear primarily in the shapes of their drift time distributions. As presented in figure 3.14, the effect has been studied with a simple Monte Carlo simulation: On the base of the model discussed in section 3.5.4, the drift time distribution at 300 K of three identical SDDs with different surface areas (circular, hexagonal and quadratical) was calculated. In the simulation, a uniform irradiation of the surface area, negligible charge loss processes and a total absorption of the X-rays was assumed. Due to longer drift paths, the drift time distribution of the quadratical SDD has flat edges compared to the circular and hexagonal one. This tendency is confirmed by the measured drift time distributions of an E17-SDD (hexagonal surface area) and a SIDDHARTA-SDD (quadratical), see figure 3.14, below.

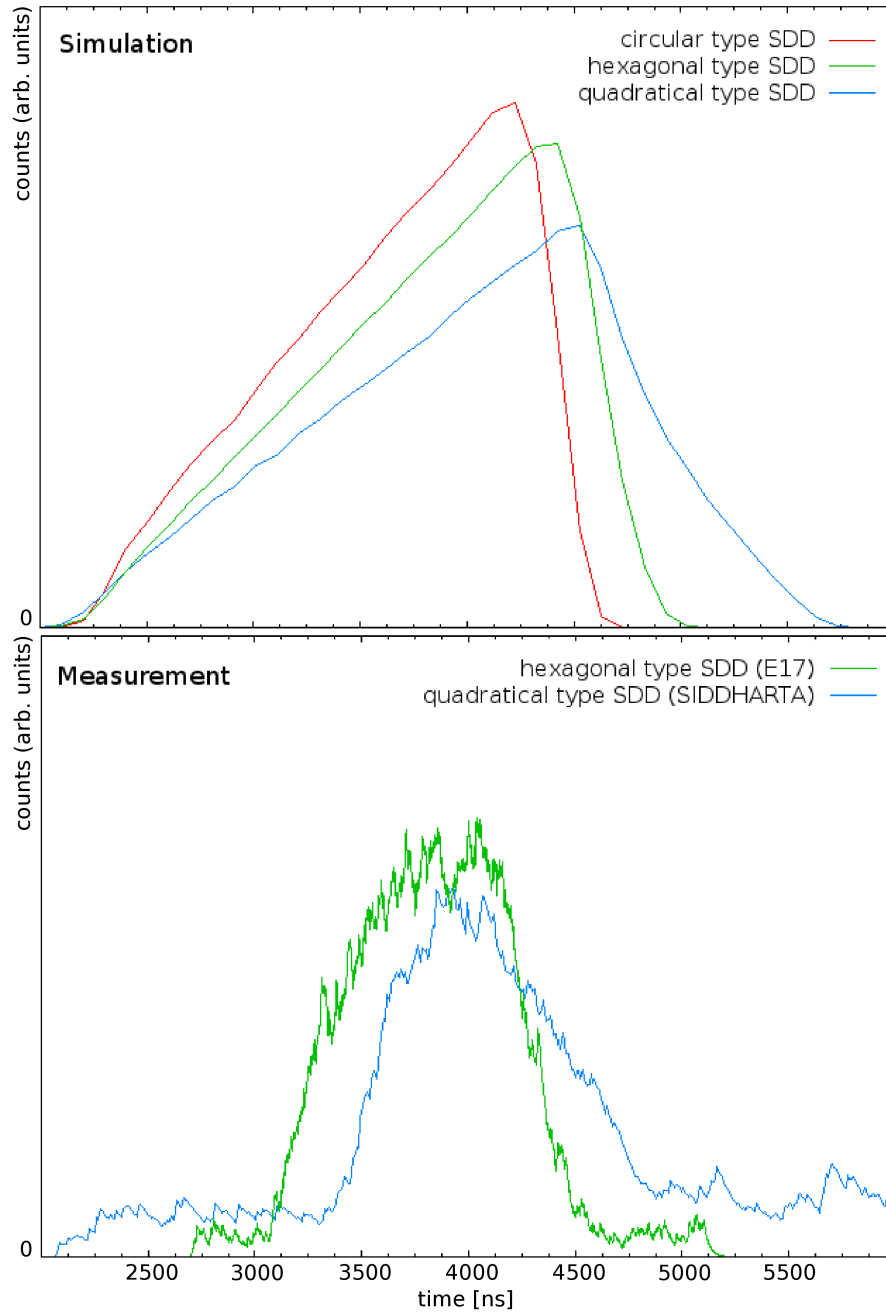


Figure 3.14: Top: A simulation of the drift time distribution of three types of SDDs, each with an absorption depth of $500\ \mu\text{m}$ and an area of $1\ \text{cm}^2$. The electron mobility was set to $1400\ \text{cm}^2\text{s}^{-1}\text{V}^{-1}$, corresponding to a silicon temperature of 300 K. The intrinsic time resolution of the SDDs was assumed to be 70 ns, simulated by a convoluted Gaussian function. Bottom: Measured drift time distribution at 170 K of an E17-SDD and a SIDDHARTA-SDD.

The E17 experiment offers additional challenges by necessitating low SDD temperatures, a separation of their preamplifiers of up to 30 cm and a measurement precision of <2 eV. First, the preamplifiers are modified in such a way that events occurring during the discharging process of the detectors are rejected. Second, a study on the temperature dependence of the SDDs' response function was performed in order to find optimum conditions of the SDDs and their preamplifiers. The results of these studies are:

- The energy resolution was found to be stable with approximately 150 eV at 5.9 keV at SDD temperatures above 130 K up to 200 K.
- To keep the peak center positions stable within 0.5 eV, the temperatures of the preamplifiers and of the SDDs have to be controlled with a precision of 1 K.
- The operation limits of the SDDs and the preamplifiers necessitate a minimum operation temperature of 130 K and 270 K, respectively.
- The FWHM of the drift time distribution, obtained via a coincidence measurement with a PIPS detector, is 400 ns at 120 K. Its temperature dependence with T^n ($n = 3.00$) can be understood with the temperature dependence of the electron mobility in silicon.

Chapter 4

Kaonic Helium with SIDDHARTA

In the SIDDHARTA (Silicon Drift Detectors for Hadronic Atom Research by Timing Application) experiment, low-energy kaons generated by the DAΦNE collider in Frascati (Italy) are stopped in gaseous ^3He and ^4He targets with different densities. The kaonic helium X-ray transitions were measured with the special designed squared-shaped silicon drift detectors described in chapter 3. In order to calibrate the SDDs periodically, characteristic X-rays from metal foils were excited via irradiation by an X-ray tube. A triple coincidence measurement, arranged between a kaon detector and the SDDs allowed a very efficient background suppression. From the SDD energy data, the peak areas of the $3d \rightarrow 2p$, the $4f \rightarrow 2p$ and the $5g \rightarrow 2p$ transitions were obtained for ^3He and ^4He . The yields were calculated for each transition, i.e. the ratio of the number of X-rays from a transition (contributing to the peaks in the spectra) to the number of captured kaons, with inputs from a Monte Carlo simulation. The experimental setup, the measurement procedure and the evaluation are described in this chapter.



Figure 4.1: Photograph of the two main rings at DAΦNE.

4.1 The facility: DAΦNE

DAΦNE (Double Annular ring for Nice Experiments) is an e^-e^+ collider in the National Laboratory of Frascati (NLF), optimized for the production of Φ mesons ($s\bar{s}$) with a mass of $m_\Phi = 1020$ MeV. The facility consists of an injection system (Linac and Accumulator) and of the two main rings for positrons and electrons with two interaction points. A picture of the current facility is presented in fig. 4.2¹.

The injection procedure is described in the following:

Electron generation: A cathode delivers 120 keV electrons which are injected into the linac with a total length of 60 m (beam pulse width: 10 ns, repetition rate: 50 Hz, RF frequency 2856 MHz).

Positron mode: The electrons are accelerated to 250 MeV and focused on a removable target, producing positrons with an efficiency of $\approx 1\%$. The positrons are separated from the electrons and accelerated to 550 MeV. They enter the accumulator - a small storage ring - and finally all pulses leave the accumulator with 510 MeV and are injected to the positron main ring.

Electron mode: By removing the target for the positron production in the

¹Picture from www.lnf.infn.it/acceleratori

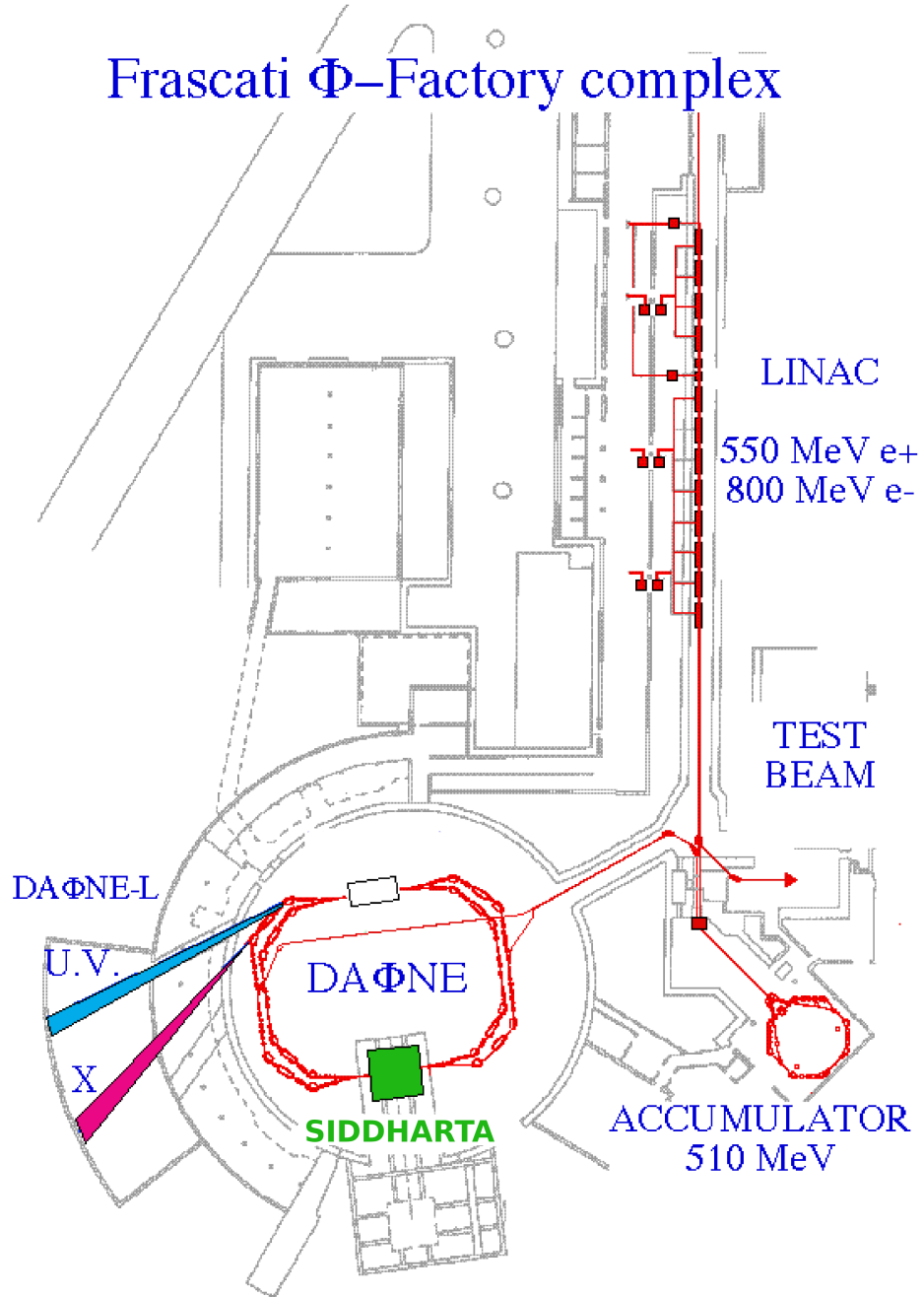


Figure 4.2: DAΦNE mainly consists of the injection area including Linac and Accumulator and of the main rings with their two interaction points (only SIDDHARTA is emphasized in green).

linac, the electrons are accelerated through the whole linac up to 800 MeV. They undergo the same procedure as the positrons, followed by an injection in the electron main ring. The luminosity is measured both by the experimental detectors via the well-known Φ decay rates, as well as by a special system of counters by comparing Monte-Carlo simulated values to scattered electrons and bremsstrahlung events [65].

Collision: The beams are brought into collision with a center of mass energy of 1020 MeV (Φ -resonance) and an annihilation cross-section of $\sim 5 \cdot 10^3$ nbarn. The Φ -meson² decays with a probability of ~ 50 % into a K^+K^- -pair. Other relevant decay modes are the decay into a couple of the neutral weak mixed eigenstates K_L ($\tau \approx 10^{-8}$ s) and K_S ($\tau \approx 10^{-10}$ s) and the decay into three pions. Note that the beams are not exactly aligned in the interaction point: they collide at an angle of ~ 53 mrad. This side effect leads to a so-called Φ -boost, i.e. an additional kinetic energy, causing an angular dependent momentum distribution of the decay products. The experimental setups are positioned at one of the two interaction points.

Beam characteristics: In the current development stage, one injection cycle lasts up to 25 min with a peak luminosity between 3.5 and $4 \cdot 10^{32} \text{ cm}^{-2}\text{s}^{-1}$, see fig. 4.3 [65]. The beam lifetimes are dominated by the **Touschek effect**: due to particle collisions within a bunch, a momentum transfer from the transversal to the longitudinal plane leads to a scattering along the longitudinal axis. Therefore, especially in dense and low energetic beams, particles - in this case: e^+ and e^- - get lost and contribute to the background ("machine background").

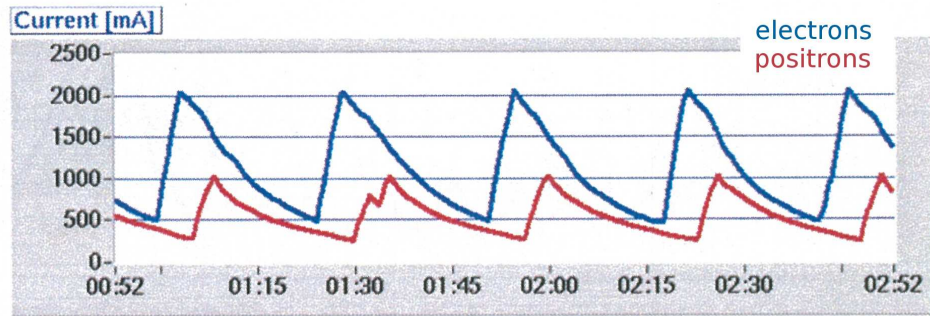


Figure 4.3: Injection cycle of electrons (blue) and positrons (red) over a period of 2 h, figure from ref. [65].

²mean life time: $\tau \approx 1.6 \cdot 10^{-22}$ s

4.2 The SIDDHARTA Setup

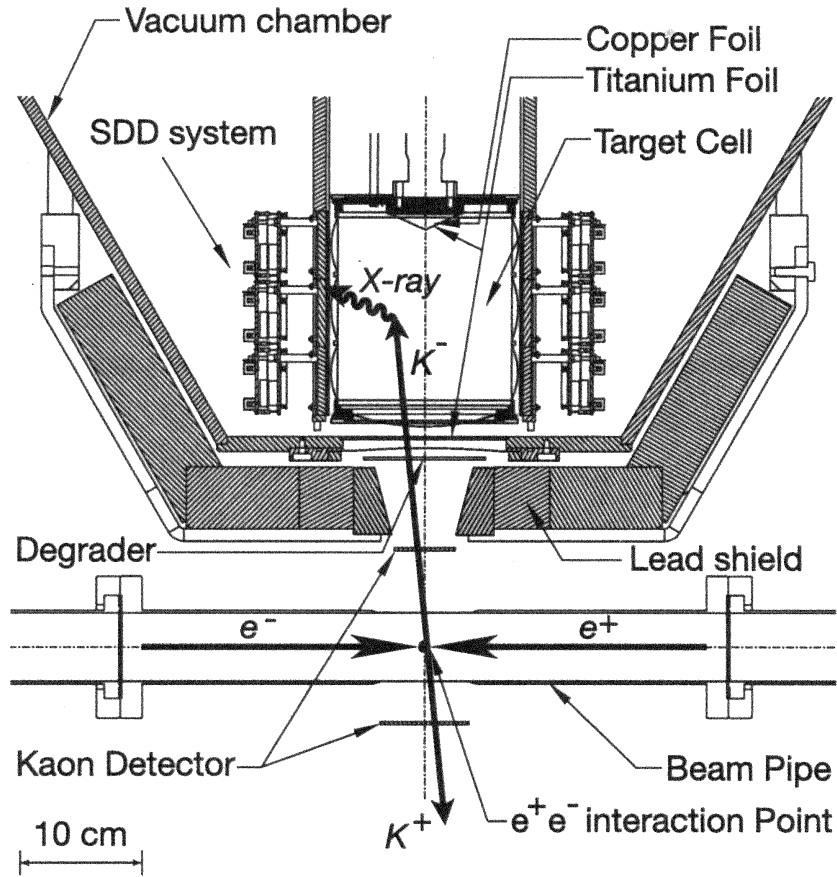


Figure 4.4: The SIDDHARTA setup, showing the important features: the SDD system surrounding the target cell, and the two parts of the kaon detector above and below the interaction point.

The SIDDHARTA setup, positioned at one of the e^+e^- interaction points, is shown in figure 4.4. The setup was carefully shielded with lead in order to suppress machine background dominated by the Touschek effect (e^+ , e^-) and bremsstrahlung. Further background comes from particles from the Φ -meson and the kaon decays (mainly pions). The main features of the setup are:

- *Cryogenic target:* The cylindrical target cell (see fig. 4.5) was completely covered with a Kapton foil with a thickness of $75\ \mu\text{m}$. For the kaonic ^3He and ^4He measurements which are reported in this thesis and partially published in ref. [45], a cell with a radius of 7.2 cm and a height of 15.5 cm was used, filled with ^3He gas (density: $0.96\ \text{g/dm}^3$) or ^4He gas (density: $1.65\ \text{g/dm}^3$), both at a temperature of around 20 K.
- *Kaon detection:* The so-called **kaon detector**³ consists of two scintillators with optically coupled photomultipliers, located above and below the beam pipe in the interaction point. Via a time-of-flight measurement, the slow K^+K^- pairs can be clearly separated from fast minimum ionizing particles (MIPs), i.e. e^+ and e^- from the machine background and Φ -decay products.
- *Degrader:* Additionally, a **degrader** made of carbon was installed above the upper kaon detector in order to reduce the kaon energy and to stop the K^- in the helium gas. The Φ -boost - arising from the beam collision angle at the interaction point - leads to an angular dependent momentum of the kaons which varies up to 10 %. This is compensated by a stepwise shaped degrader, whose thickness varies within 1 mm. In order to maximize the number of stopped kaons in the helium target, the final optimization of the degrader thickness was performed experimentally in the preparatory stage of the measurements: The optimum degrader thickness used for all further measurements was found via a determination of the number of the detected $3d \rightarrow 2p$ X-rays in kaonic ^4He as a function of the degrader thickness. For a picture of the result of these measurements is referred to fig. 4.22 in section 4.6.1, where

³area: $(7.2 \times 7.2)\ \text{cm}^2$, thickness: 1.5 mm, time resolution: $<100\ \text{ps}$ FWHM

its compared with simulated thickness variations in the course of the description of the Monte Carlo simulation.

- *X-ray detector system:* SDDs (see chapter 3) were used for the X-ray detection, each with an active area of 1 cm^2 , a thickness of $450 \text{ }\mu\text{m}$ and kept at a temperature of $(170 \pm 0.5) \text{ K}$. The target cell was surrounded by altogether 144 SDDs with a distance of 7.8 cm between target cell and SDDs. The X-ray signals of the SDDs were processed by a special developed read-out system [60].
- *Calibration:* Characteristic X-rays from thin Cu and Ti foils on the top of the target cell were used in order to convert the SDDs' ADC events into energy data. The X-rays were excited by irradiation with an X-ray tube, replacing the upper kaon detector in regular intervals.

Almost all K^+K^- pairs produced via the Φ decay in the interaction point of the electron and positron ring are recorded with the kaon detector. The kaons pass through the carbon degrader and enter the target cell through a circular Kapton window at the bottom of the vacuum chamber. In contrary to the K^+ , the K^- subsequently interact with the target gas and the surrounding material by producing among others kaonic X-rays. In order to correlate the X-ray events in the SDDs with the kaon events, a triple coincidence measurement between the upper and the lower part of the kaon detector and the SDDs was arranged. By use of a clock with a frequency of 120 MHz, the time difference between the conjunction of the SDD signals and the timing signals in the kaon detector was recorded whenever it occurred within a time window of $6\ \mu\text{s}$.



Figure 4.5: Photograph of the target cell.

4.3 Experimental procedure and data acquisition

4.3.1 Data recording

The following data were recorded simultaneously:

- The energy data of all SDD signals, recorded with an ADC
- The time signals of the kaon detector, separating kaon and MIP events
- The time difference between the SDD signals and the kaon detector signals, recorded with a TDC (obtaining the "drift time distribution" of the SDDs)
- The coincidence signal of the correlated SDD and kaon detector signals
- The measurement time
- The beam current

A scheme of the logic is presented in fig. 4.6.

The coincidence measurement allowed a background suppression by selecting only kaon-correlated SDD events. Additionally, a high threshold signal allowed to reject all SDD signals produced by photons with an energy higher than 20 keV, which also provided background suppression.

The nomenclature of the SDDs is adapted to their read-out system for ADC events with 180 channels, separated into 6 so-called busses. The available 30 read-out positions per bus are assigned to 24 SDDs and 6 empty locations. From this, each SDD can be identified unambiguously, where the first character of their three-digit ID refers to the bus and the last two characters 01 to 30 stand for their position in the bus.

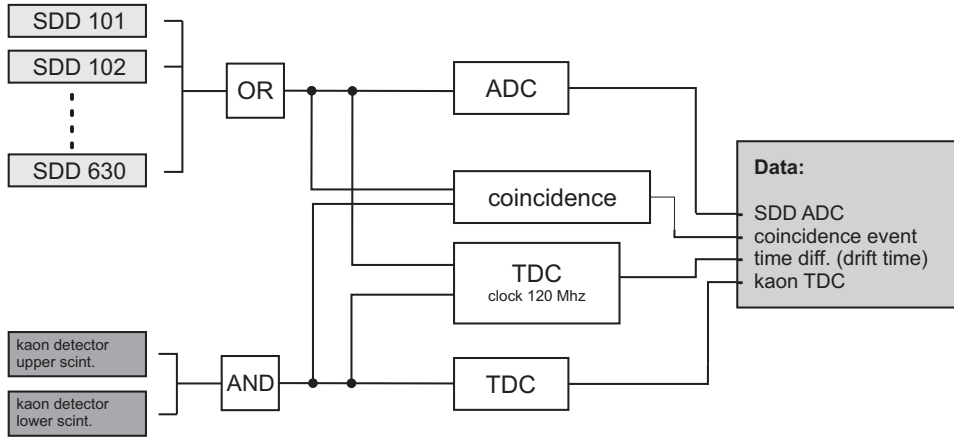


Figure 4.6: Data acquisition in SIDDHARTA. The read out logic circuits of the SDDs and the kaon detector are independently operating (logic not shown here) and combined in the schematically presented final stage of the data acquisition process.

4.3.2 Data types

Two types of data have been recorded during the SIDDHARTA runs:

Production data:

The so-called production data files were recorded for about 10 minutes per file when the K^- from the Φ -decay stopped in the helium target and produced X-rays. Due to the recording of the coincidence signal between the SDD and the kaon detector signals, two types of production data can be distinguished. By extracting only those events where the coincidence occurred, the **coincidence data** with drastically suppressed background are obtained. An energy spectrum of such kaon-correlated SDD events is presented in fig 4.7 (b).

On the other hand, data uncorrelated to events in the kaon detector (so-called **selftrigger data**) therefore mainly show background signals from Φ -meson and kaon decay products, from machine background and bremsstrahlung, as well as some excited X-rays of the surrounding material (see fig. 4.7, (a)).

Calibration data:

During the measurement of the characteristic X-rays from thin metal foils used for the SDD calibration, the upper kaon detector was replaced by an X-ray tube. The calibration data were recorded every few hours for also ~ 10 minutes per file and evaluated by excluding coincidence data between SDDs and kaon detector. The calibration procedure furthermore allowed a superposition of the energy spectra of the chosen SDDs.

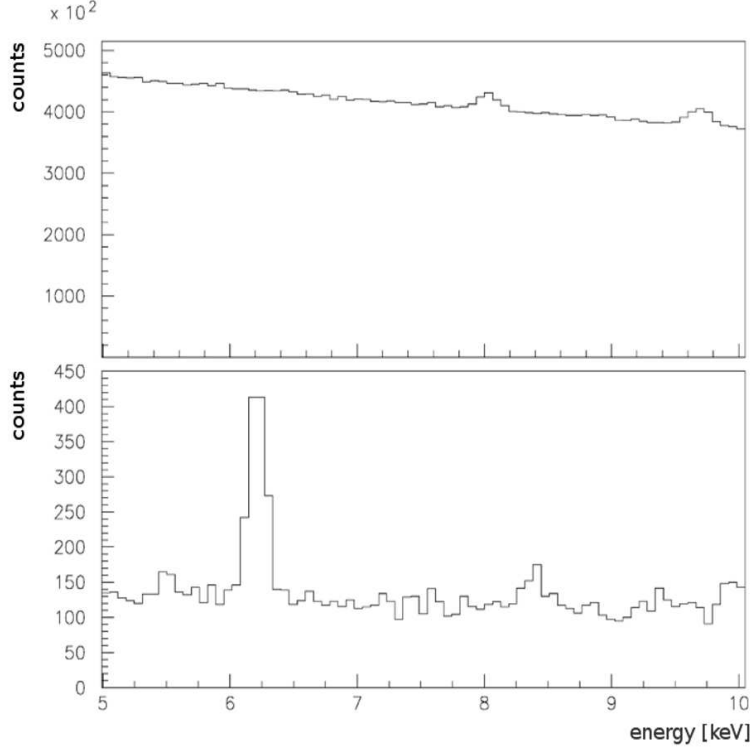


Figure 4.7: (a): Energy spectrum of uncorrelated X-ray events. (b): Energy spectrum of the coincidence data. For the procedure to obtain these spectra, see section 4.5.

4.3.3 Data used for evaluation

Figure 4.8 shows a summary of the measurements with the SIDDHARTA setup in 2009. During the first period of the year, the X-rays from kaonic ${}^4\text{He}$ [44], kaonic hydrogen and kaonic deuterium [66] have been investigated. In November 2009, the X-rays from a ${}^3\text{He}$ target with a total luminosity of about 16 pb^{-1} and from a ${}^4\text{He}$ target with a total luminosity of approximately 5 pb^{-1} have been successively measured for a few days. 172 production data files from the ${}^3\text{He}$ run and 50 production data files from the ${}^4\text{He}$ run have been taken for the determination of the yields. The calibration of the SDDs obtained from 13 calibration files during the ${}^3\text{He}$ run was also used for the back-to-back measured ${}^4\text{He}$ data.

SIDDHARTA 2009						
January - July			July - October		November	
kaonic ^4He , H			^4He , H, d		^3He , ^4He	

November 2009						
3rd	4th	5th	6th	7th	8th	
^3He	^3He	^3He	^3He	^3He	^4He	^4He
Production data: 172 files					50 files	
Calibration data: 13 files					---	

Figure 4.8: Overview of the kaonic X-ray measurements with SIDDHARTA, with focus on the ^3He and ^4He runs in november 2009.

4.4 Data evaluation: Calibration data

For the calibration of the SDDs, Cu and Ti foils at the top of the target cell were excited with radiation from an X-ray tube. Eventually 13 calibration files with sufficient statistics were taken from the ^3He run in november 2009, from which only kaon-uncorrelated ADC events in the SDDs have been extracted. Therefore, for each of the 144 SDDs, 13 calibration spectra were available.

A first selection on principal functionality was performed by eye, since a few detectors did not work properly. The spectra of the remaining working SDDs were fitted with four Gaussian functions for the Ti- K_α , the Ti K_β , the Cu K_α and the Cu K_β lines, respectively, and one linear function for the background, see fig. 4.9.

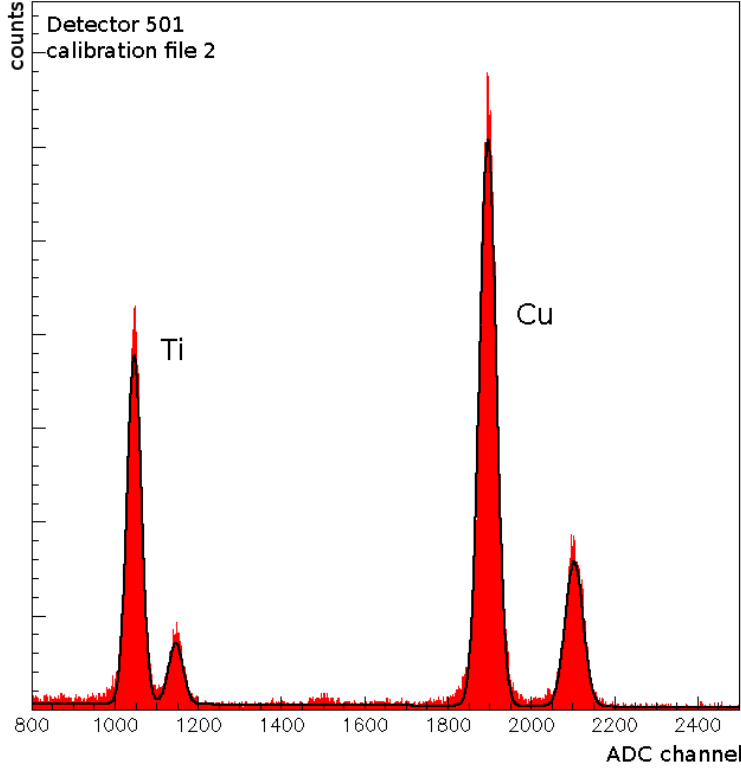


Figure 4.9: Calibration spectrum of an SDD (ID=501), fitted with a linear function for the background and four Gaussian functions for Ti K_{α} , Ti K_{β} , Cu K_{α} and Cu K_{β} ($\chi^2 = 2.3$).

Further SDDs were excluded due to instabilities in the peak centers or bad energy resolutions (> 200 eV FWHM), or when they showed very high background in the region of interest. All detectors located in bus 2 were refused.

Finally, **92 SDDs** were chosen and used for all further analysis.

The calibration of these 92 SDDs was done with the K_{α} peaks of Ti and Cu, for which the averages over all 13 Ti K_{α} and all 13 Cu K_{α} ADC channel peak centers from the calibration spectra were calculated for each SDD.

Note that a K_{α} line actually is a superposition of two subadjacent $K_{\alpha,1}$ and $K_{\alpha,2}$ lines. For the literature values therefore the intensity-weighted energy values of $K_{\alpha,1}$ and $K_{\alpha,2}$ were used which is 4508.83 eV for the Ti K_{α} line (intensity ratio: $K_{\alpha,2}/K_{\alpha,1}=0.5$) and 8041.04 eV for the Cu K_{α} line (intensity ratio: $K_{\alpha,2}/K_{\alpha,1}=0.51$), values from ref. [67].

Remarks to the fits:

The superposed Ti K_α and Cu K_α lines can be sufficiently reproduced with one Gaussian fit each, i.e. the sum of the Gaussian single lines $K_{\alpha,1}$ and $K_{\alpha,2}$ can be treated as a Gaussian function. For demonstration purposes, Monte Carlo simulations of the superposed Ti K_α , Cu K_α and Au L_α lines were performed, including the properties of a SIDDHARTA-SDD. First, a Gaussian function with the weighted energy mean value of $K_{\alpha,1}$ and $K_{\alpha,2}$ (literature values) as peak center was simulated for each line. Second, the superposition of two simulated Gaussian functions representing $K_{\alpha,1}$ and $K_{\alpha,2}$ was calculated and fitted with a Gaussian function. For Ti and Cu no significant differences in the peak center and widths between these two functions could be found, which is displayed in fig. 4.10 for the case of Cu. For the Au line in contrary, the sum of the two Au $L_{\alpha,1}$ and $L_{\alpha,2}$ lines clearly differs from a Gaussian function, i.e. the $L_{\alpha,1}$ and the $L_{alpha,2}$ line have to be fitted separately with Gaussian functions (Au $L_{\alpha,1}$: 9713.3 eV, Au $L_{\alpha,2}$: 9628.0 eV, intensity ratio: $L_{\alpha,2}/L_{\alpha,1}=0.11$).

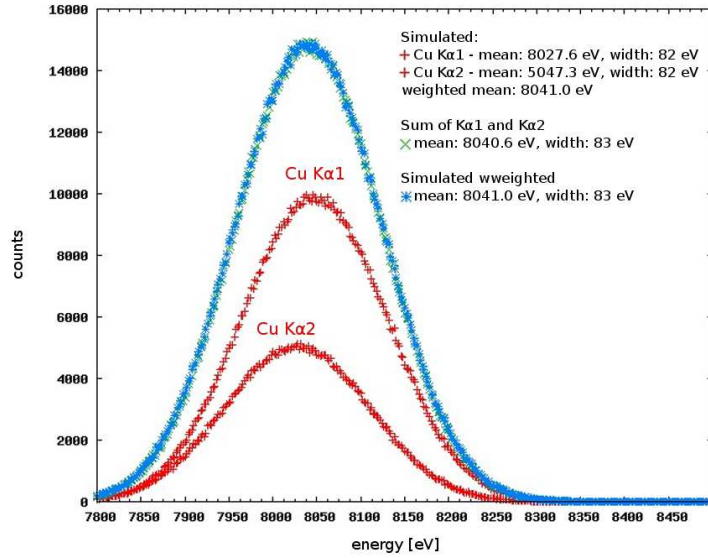


Figure 4.10: Comparison of two simulated SDD response functions. Blue crosses: Gaussian function with the weighted energy mean value of the Cu $K_{\alpha,1}$ and $K_{\alpha,2}$ line as peak center. Green: sum of the simulated Gaussian Cu $K_{\alpha,1}$ and $K_{\alpha,2}$ (both in red) lines.

4.5 Data evaluation: Production data

4.5.1 Self-trigger data

With the kaon-uncorrelated calibrated SDD energy data of the ^3He run, the energy dependence of the peak widths of X-ray lines was studied. Since the low-energy background (< 5 keV) of these spectra was extremely high in some detectors, further SDDs had to be excluded in order to take the Ti peak into account for these studies. A summed self-trigger energy spectrum of the remaining 30 SDDs - in comparison to a self-trigger spectrum with 92 SDDs - is presented in fig. 4.11.

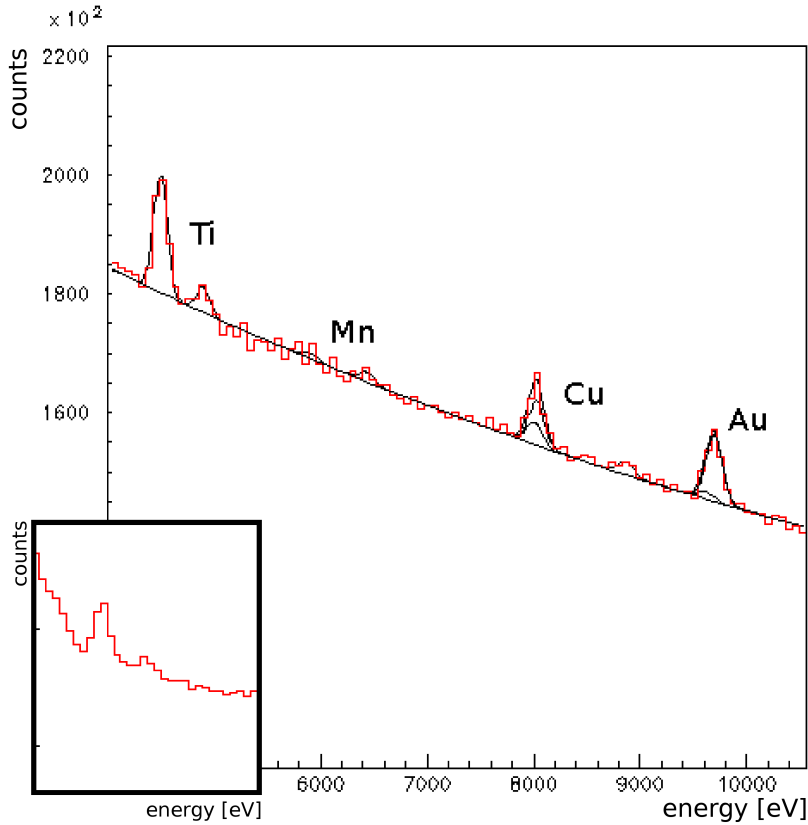


Figure 4.11: Energy spectrum of kaon-uncorrelated X-ray data (self-trigger spectrum), summed over 30 SDDs. In comparison, the small picture shows the region around the Ti peaks in a spectrum where all 92 detectors are summed.

In this spectrum, the characteristic X-rays of the metal foils for calibration purposes (titanium and copper), of an ^{55}Fe source (manganese) and of the gold wires on the rear side of the SDDs are visible. The Ti K_α , Ti K_β , Mn K_α , Mn K_β , Cu K_β , Cu K_α and Au L_α lines were fitted with Gaussian functions, the background was fitted with a polynomial function. In case of the Cu K_α and Au L_α , the subjacent $K_{\alpha,1}/K_{\alpha,2}$ and $L_{\alpha,1}/L_{\alpha,2}$ lines, respectively, were included to the fit functions with fixed intensities and fixed energy intervals according to the literature values of ref. [67].

The energy dependence was determined with the Gaussian widths of Ti K_α , Cu $K_{\alpha,1}$ and Au $L_{\alpha,1}$. According to equ. 3.3 (discussed for the SDD response function in section 3.2), the widths were fitted with

$$width = \sqrt{n_{el}^2 + \omega \cdot E \cdot F} \quad (4.1)$$

with n_{el} as the electronic noise, $\omega = 3.7$ eV as the electron-hole pair creation energy and F as the Fano factor. Consistent with the literature value for the Fano factor [55], a value of $F = 0.093 \pm 0.008$ was obtained. The result is presented in fig. 4.12. The measured widths in the self-trigger spectrum with 30 SDDs are marginally smaller than the widths in a self-trigger spectrum with all 92 SDDs. Nevertheless, this effect is negligible in the region below 10 keV compared to the uncertainty resulting from a fit where the low-energy information of the Ti peak is excluded. The results of this analysis were used for an estimation of the peak widths in the spectra of the coincidence data.

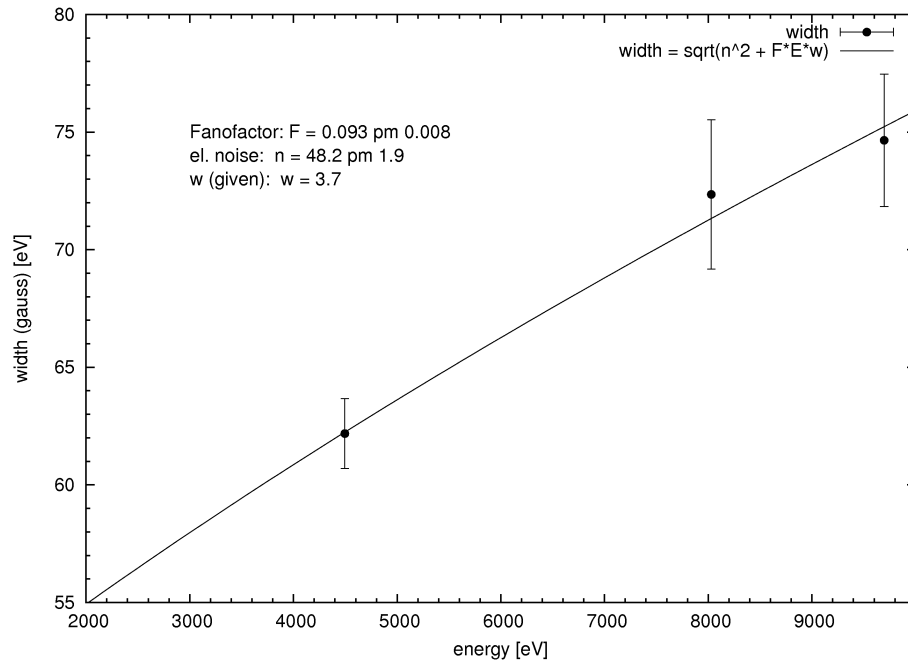


Figure 4.12: Energy dependence of the fitted Gauss-widths of the Ti K_{α} ($K_{\alpha,1}$ and $K_{\alpha,2}$ neglected), Cu $K_{\alpha,1}$ and Au $L_{\alpha,1}$ lines. The electron-hole pair creation energy w was fixed with 3.7 eV ([55]), n represents the electronic noise and f the Fano factor.

4.5.2 Coincidence data

From 172 ^3He and 50 ^4He production files, those events were extracted where a coincidence between the kaon detector and the SDDs occurred simultaneously. The energy information of these events is used for the determination of the X-ray transitions in kaonic helium. Fig. 4.13 shows the energy spectrum of such kaon-correlated X-ray events, summed over 92 calibrated SDDs. Procedures for additional background suppression are described in the following.

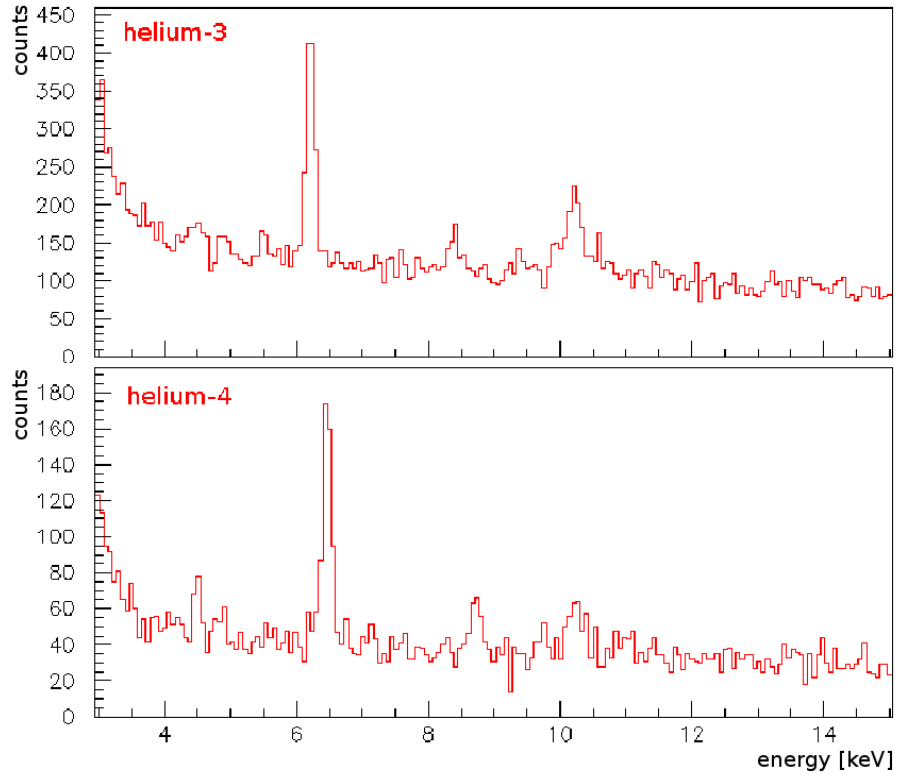


Figure 4.13: Energy spectra of the raw coincidence data of the He runs. 92 SDDs are summarized. The peak around 6 keV corresponds to the $3d \rightarrow 2p$ transition in kaonic ^3He and ^4He .

Drift time selection and slewing correction

The time difference between an SDD event and a kaon detector was recorded with a TDC. The shape of the resulting peak in the time spectrum corresponds to the drift time distribution of the SDDs. Background events can be excluded by selecting only the events contributing to the SDDs' drift time distribution, i.e. mainly kaon-correlated X-ray events. As already indicated for the E17-SDDs in section 3.5 in a similar manner, the timing signals of the TDC are energy dependent. A proper selection of the TDC events which contain the relevant SDD X-ray events between 3 keV and 10 keV therefore necessitates a correction.

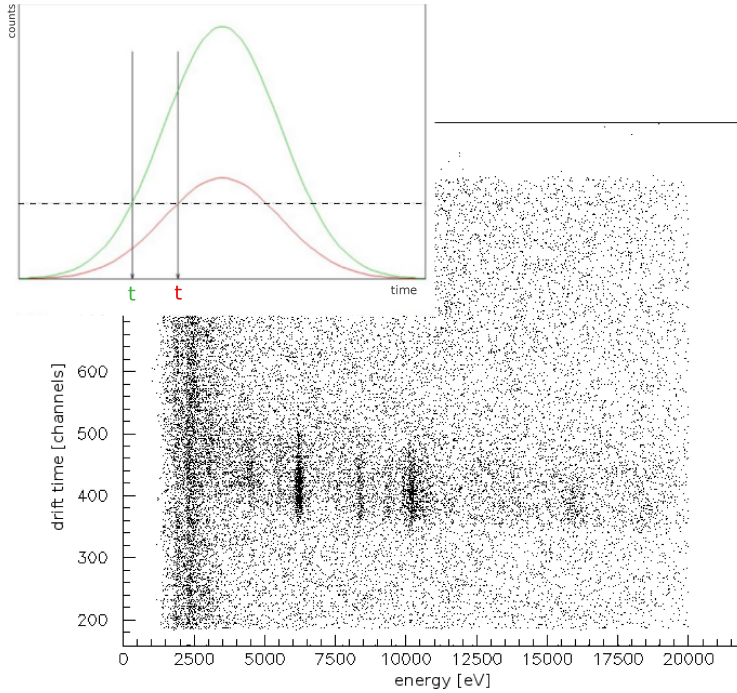


Figure 4.14: Small picture: illustration of the time walk between two signals when they are processed in a discriminator with fixed threshold (dotted line). Big picture: Signals in the TDC channels vs. energy data of the ^3He runs in the SDDs: a slewing is observable where signals with higher energy are processed earlier than low energy signals. The dense region around 6000 eV corresponds to the kaonic $^3\text{He } 3d \rightarrow 2p$ transition.

The small picture in fig. 4.14 illustrates the time difference ("time walk")

between signals of different height caused by the processing properties of a discriminator with fixed voltage threshold. This processing difference leads to a so-called slewing, i.e. an energy dependence of the time signals in the TDC. In fig. 4.14, the TDC channels are plotted as a function of their corresponding energy signals in the SDDs, here for all 172 ^3He files. This presentation is equal for the ^4He files. One can clearly see that signals with higher energy are recorded earlier (i.e.: with a lower channel number) in the TDC compared to SDD signals with lower energies.

For the **slewing correction**, the energy data in the region between 2 keV and 15 keV were divided into nine sections. The corresponding TDC events of these energy sections were fitted with Gaussian functions (fig. 4.15 (a)). The peak centers of these fits were plotted as a function of the mean value of the selected energy region, see fig. 4.15 (b), and fitted with the following function:

$$TDC_{corr}(E) = TDC_0 - (a + b * E + c * \log(E - d)) \quad (4.2)$$

with TDC_{corr} representing the corrected TDC events, TDC_0 as reference value at $E = 2$ keV and E as the calibrated energy data of the SDDs. The fit gives: $a = 520$, $b = 12$, $c = -105$ and $d = -1$. With this function, the TDC signals in all ^3He and ^4He production data files were transformed into corrected TDC events.

Finally, the SDD energy events contributing to the corrected drift time distribution were selected between TDC channel 380 and 560. Fig. 4.16 compares the uncorrected (a) and corrected (b) 2d plot of the TDC signals as a function of the SDD energy events. In the right hand picture (b), also the threshold of the drift time selection (channel 380 to channel 560) is displayed. The blue circles and bars correspond to the mean values and the widths, respectively, of the Gaussian fits of the energy sections from the slewing correction.

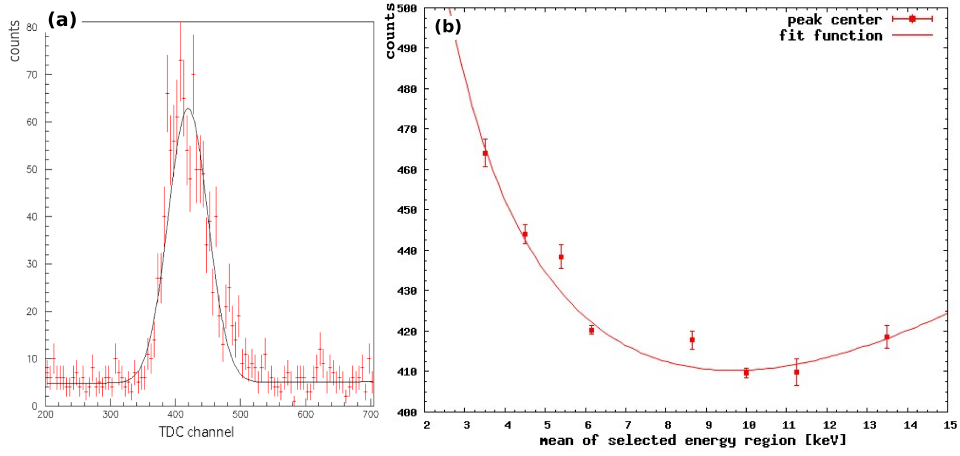


Figure 4.15: (a): TDC time spectrum of the coincidence measurement between kaon detector and SDD energy signals, the latter for a selected energy region around 6 keV. The peak corresponds to the drift time distribution of the SDDs, fitted with a Gaussian function. (b): Peak centers of the TDC time spectra as a function of the mean value of their corresponding energy section.

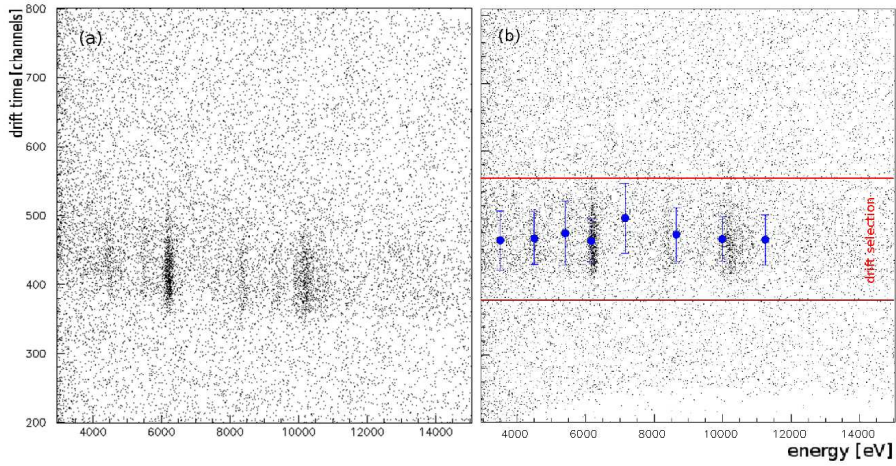


Figure 4.16: As a function of the energy data in the SDDs, the corresponding uncorrected (a) and corrected (b) TDC events are displayed. Also the mean values and widths of the Gaussian functions (blue) and the thresholds of the drift time selection (red) are displayed.

Kaon selection

The kaon detector is made up of an upper and a lower scintillator, each equipped with two photomultipliers. The slow K^+K^- pairs are detected, as well as fast MIPs (electrons, positrons, Φ -decay products). The output signals from the photomultipliers were recorded with a TDC where the start signal comes from a clock. Due to the good time resolution of the kaon detector, the kaons are distinguishable from MIPs. Fig. 4.17 shows a plot of the TDC channels of the two kaon detectors: the sum of the two upper photomultipliers is the ordinate and the sum of the two lower ones is the abscissa. The products of two e^+e^- collisions are visible, happening in the coincidence window of $6\ \mu\text{s}$. The information of the kaon detector offers an additional background suppression: While the coincidence data generally contain the SDD events coupled to kaon detector events, the SDD energy data which solely correspond to the K^+K^- -events were chosen. These events are in the following channel intervals: for the upper detector channels 2110 to 2180 and channels 2260 to 2330, for the lower detector: channels 2060 to 2120 and channels 2220 to 2280. The procedure was executed for all ^3He and ^4He files.

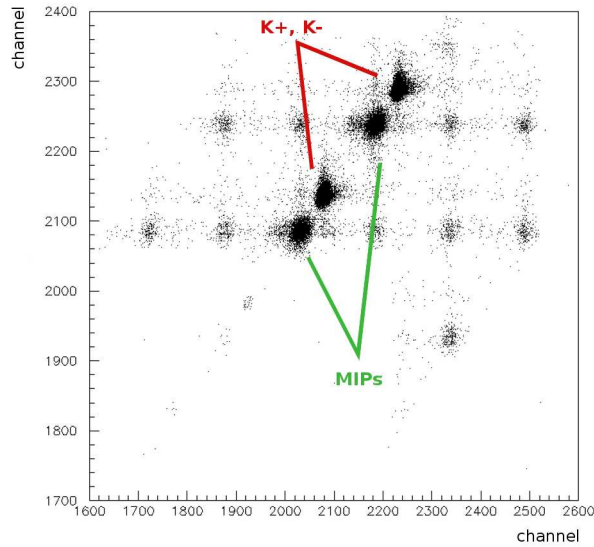


Figure 4.17: 2D spectrum of the lower and upper kaon detector.

In fig. 4.18 the result of the drift time and kaon selection processes is presented. For the ^3He energy spectrum of the coincidence data the raw spectrum without selections is shown in black, compared to the background-suppressed spectrum with kaon selection and drift time selection (red). The same procedure was applied to the ^4He data.

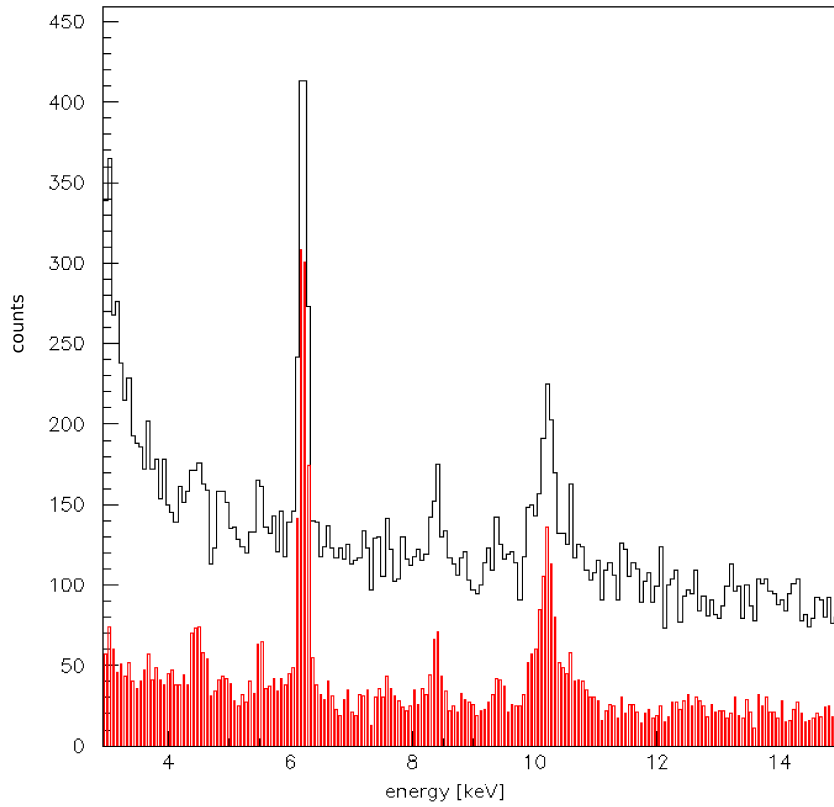


Figure 4.18: Raw ^3He energy spectrum (black) in comparison to the energy spectrum with kaon and drift time selection (red).

Fits

The calibrated energy events of 92 SDDs, extracted from the coincidence data, were exempted from background via kaon selection and drift time selection and summarized. Subsequently, the peaks of the X-ray transitions between 4 keV and 10 keV in the ^3He energy spectrum and in the ^4He energy spectrum were fitted with a Gaussian function for each peak and a linear function for the background. In order to get the peak area for the yield calculation directly from the fits, the peak height in the Gaussian fit functions was replaced by the peak area according to:

$$A = \sqrt{2\pi} \cdot \sigma \cdot h \quad (4.3)$$

with σ as the width of the Gaussian function. The fit function with mean value μ results in:

$$f(x) = \frac{A}{\sqrt{2\pi} \cdot \sigma} \cdot e^{-\frac{(x-\mu)^2}{2\sigma^2}} \quad (4.4)$$

This fit function was used for all X-ray peaks in the spectra. Fig. 4.19 shows the ^3He and ^4He spectra with the total fit function.

The $3d \rightarrow 2p$, $4f \rightarrow 2p$ and $5g \rightarrow 2p$ X-ray transitions in kaonic He are clearly visible, with calculated energy values (for the calculations see section 2.3 in chapter 2):

	^3He	^4He
kHe $3d \rightarrow 2p$	6225 eV	6464 eV
kHe $4f \rightarrow 2p$	8400 eV	8722 eV
kHe $5g \rightarrow 2p$	9406 eV	9767 eV

Also the Ti K_α (4509 eV), Ti K_β (4932 eV) and Cu K_α (8041 eV) characteristic X-rays are visible, excited from the metal foils used for the calibration. These lines are also kaon-correlated since the kaons also excite characteristic X-rays in the metal foils. Further peaks show the X-ray transitions in kaonic carbon, kaonic oxygen and kaonic nitrogen which arise from captured kaons in the atoms of the Kapton foil surrounding the target cell⁴.

⁴Kapton: $\text{C}_{22}\text{H}_{10}\text{N}_2\text{O}_5$

In the fit functions of peaks with low statistics or of superposed peaks, the widths, peak centers and intensities (i.e. heights) were fixed. The value for a fixed peak width was taken from equ. 4.1, where the peak widths were calculated as a function of energy. The fixed intensity ratios to the $6h \rightarrow 5g$ X-ray transition in kaonic carbon (kC) at 5.5 keV are taken from earlier measurements of kaonic hydrogen with the SIDDHARTA setup, taken from ref. [68] and listed below in table 4.1. Special care was taken on the 10 keV region in the kaonic ^4He spectrum, because the $5g \rightarrow 2p$ transition of kaonic ^4He was superposed with the $6h \rightarrow 5g$ transition in kaonic oxygen at 9.9 keV and with the $5g \rightarrow 4f$ transition in kaonic carbon at 10.2 keV. In order to obtain the properties of the kaonic ^4He $5g \rightarrow 2p$ transition, the two other transitions were fitted with fixed widths and peak centers.

transition	energy (lit. value)	peak intensity
kO $7i \rightarrow 6h$	6007 eV	0.18
kN $6h \rightarrow 5g$	7596 eV	0.22
Cu K_α	8041 eV	0.13
kC $7i \rightarrow 5g$	8888 eV	0.30
kO $6h \rightarrow 5g$	9969 eV	1.09
kC $5g \rightarrow 4f$	10217 eV	5.10

Table 4.1: Intensity ratios relative to the kC $6h \rightarrow 5g$ taken from kaonic hydrogen measurements, [68]. The X-ray transitions in kaonic atoms are denoted with a "k" in front of the element symbol. Further transitions with lower intensities were neglected.

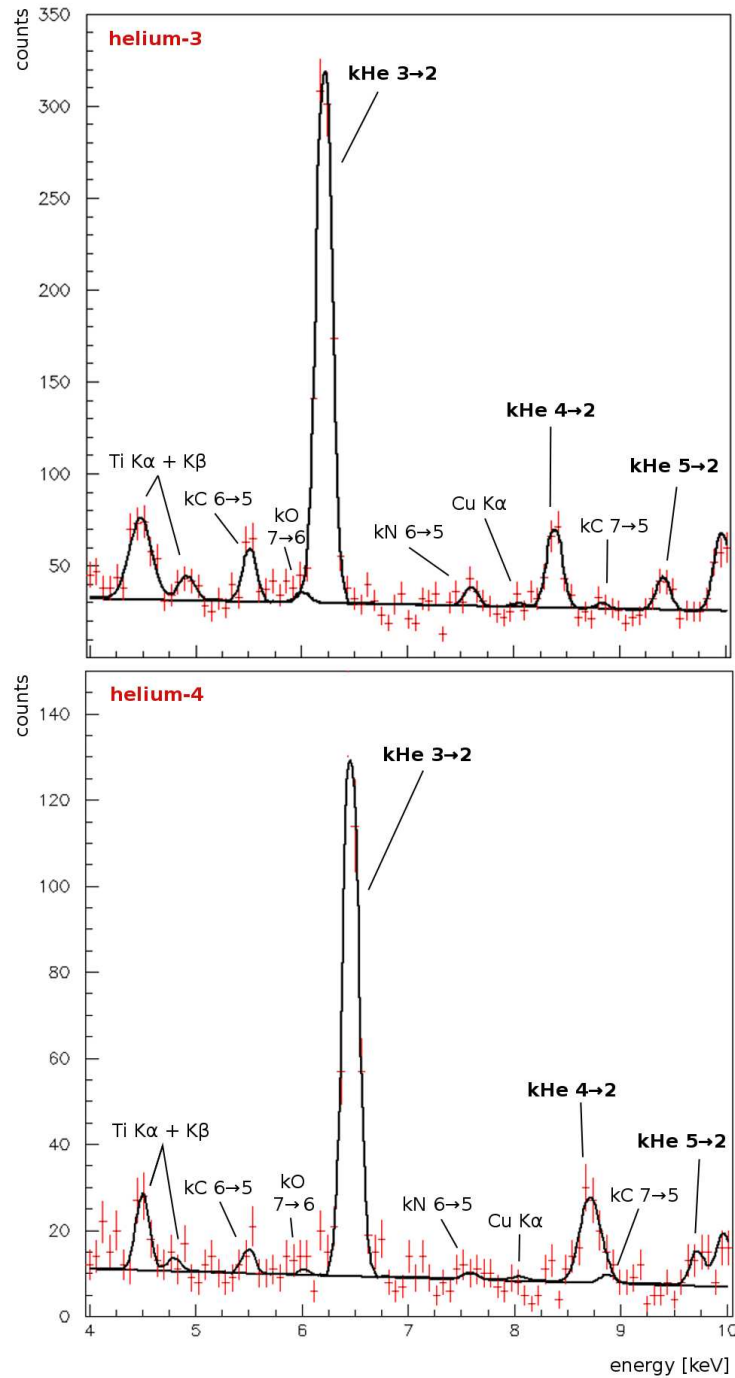


Figure 4.19: Energy spectra of kaonic ${}^3\text{He}$ and ${}^4\text{He}$, obtained after all selection processes. The "k" stands for a kaonic atom. The X-ray transitions in kaonic atoms are denoted with the value of the azimuthal quantum numbers, the characteristic X-rays of the calibration foils with K_α and K_β . In the ${}^3\text{He}$ spectrum, the subjacent $7i \rightarrow 6h$ transition in kaonic oxygen is drawn separately. In the ${}^4\text{He}$ spectrum, the subjacent $7i \rightarrow 5g$ transition in kaonic carbon is shown.

Measured strong interaction shift in kaonic ${}^3\text{He}$

The amount of evaluated ${}^3\text{He}$ data allowed the determination of the strong interaction shift in kaonic ${}^3\text{He}$ with the result of the fits. In order to cross check the evaluation procedure, the result of the strong interaction shift is then compared to the published value [45], which was obtained independently with a larger amount of data.

The strong interaction shift is obtained by calculating the difference between the energy position of the $3d \rightarrow 2p$ transition in the spectra and the calculated electromagnetic value of this transition (section 2.3). However, the direct result of the fit has to be corrected due to two significant discrepancies in the peak positions between the calibration data and the production data.

Rate shift: The position of an X-ray peak in an energy spectrum of an SDD is dependent on the rate of the radiation permeating the detector. The irradiation rate in the SDDs was significantly higher during the calibration data taking, when the X-ray tube was additionally placed in front of the entrance window of the target cell. The X-ray peak centers in the energy spectra of the production data are therefore shifted compared to the spectra of the calibration data. In order to calculate this so-called rate shift, the spectra of the self-trigger data of all 92 SDDs were used showing with high statistics kaon-uncorrelated characteristic X-rays (e.g. of the calibration foils). The Cu $K_{\alpha,1}$, Cu $K_{\alpha,2}$, Cu K_{β} , Au $L_{\alpha,1}$ and Au $L_{\alpha,2}$ line were fitted with a Gaussian function each, with fixed energy intervals and intensity ratios of the $K_{\alpha,1}$ and $K_{\alpha,2}$ lines and the $L_{\alpha,1}$ and $L_{\alpha,2}$ lines, respectively. The self-trigger spectrum of 92 SDDs is presented in fig. 4.20. Due to high background at energies < 5 keV in some SDDs, it was not possible to include the Ti peak to these calculations. The mean value of the deviances of the Cu $K_{\alpha,1}$, Cu $K_{\alpha,2}$, Au $L_{\alpha,1}$ and Au $L_{\alpha,2}$ lines to their literature values was calculated. The determined value of the rate shift is (12 ± 2) eV, the error corresponds to the accuracy of the determination of the peak positions.

Calibration shift: In order to determine the accuracy of the calibration fits, the calibration data were re-analyzed. The SDD calibration spectra were extracted with energy converted ADC events. The Ti and Cu characteristic X-ray peaks were fitted with Gaussian functions, similar to the

calibration process described in section 4.4. The averaged derivation to the literature values (weighted mean of $K_{\alpha,1}$ and $K_{\alpha,2}$) was found to be (-3 ± 2) eV.

Total peak position shift: The total shift of the energy positions in the coincidence spectra compared to the literature values is the sum of the calibration shift and the rate shift. With quadratical summed errors, the shift is (9 ± 3) eV. Note that this shift is irrelevant for the determination of the peak area used for the yield calculations.

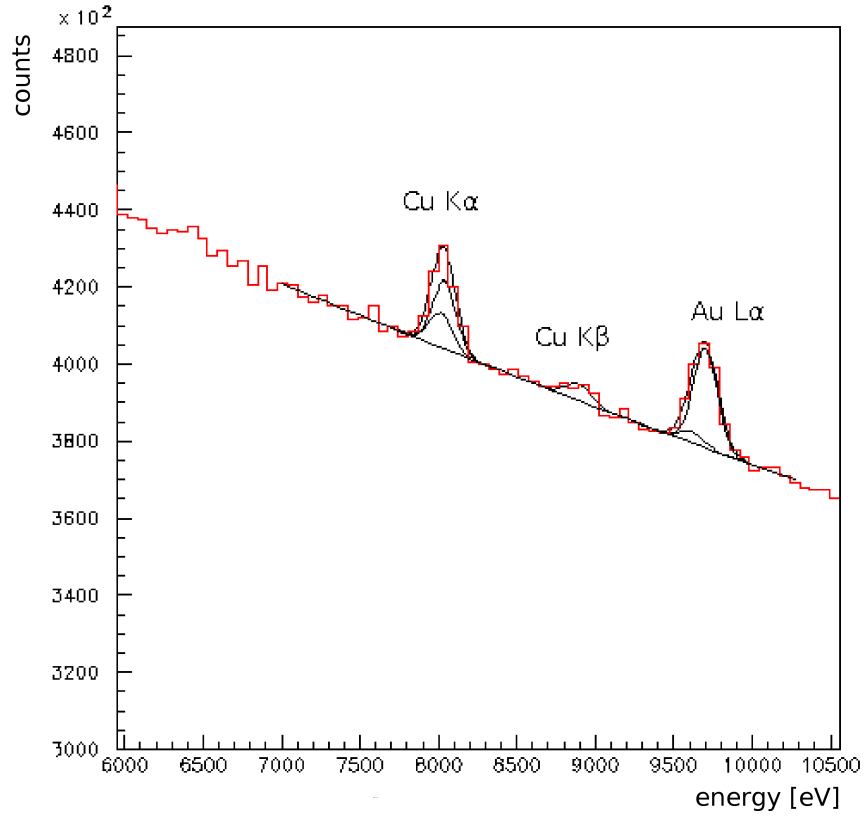


Figure 4.20: Self-trigger spectrum of all chosen 92 SDD. The $\text{Cu } K_{\alpha,1}$, $\text{Cu } K_{\alpha,2}$, $\text{Au } L_{\alpha,1}$ and $\text{Au } L_{\alpha,2}$ line, each fitted with a Gaussian function, were used for the determination of the rate shift.

The **strong interaction shift** for the $2p$ state in kaonic ${}^3\text{He}$ is defined as $\epsilon^{2p} = E_{\text{measured}}^{3d \rightarrow 2p} - E_{\text{calculated}}^{3d \rightarrow 2p}$. The calculated energy value was determined in section 2.3, the measured value arises from the peak center of the $3d \rightarrow 2p$ transition in the ${}^3\text{He}$ spectrum, fitted with a Gaussian function, including the corrections of the rate shift and the calibration fit. The strong interaction shift is presented in table 4.2 in comparison with the published value [45]. The error of the total peak position shift due to calibration and rate dependency was taken as systematic error, the statistical error comes from the Gaussian fit of the peak. While the two values of the shift are in good accordance, the distinct difference in the statistical errors between this result and the published value are attributed to the reduced data set used for the analysis in this thesis in comparison with the data set used in ref. [45].

Energy of the $3d \rightarrow 2p$ X-ray transition in kaonic ${}^3\text{He}$	
Peak center from fit	$(6213 \pm 3) \text{ eV}$
Total peak position shift	$(9 \pm 3) \text{ eV}$
Corrected peak center	$(6222 \pm 8(\text{stat.}) \pm 3(\text{sys.})) \text{ eV}$
Calculated energy	6225 eV
Strong interaction shift	$(-3 \pm 8(\text{stat.}) \pm 3(\text{sys.})) \text{ eV}$
Published value [45]	$(-2 \pm 2(\text{stat.}) \pm 4(\text{sys.})) \text{ eV}$

Table 4.2: Calculated and measured energy values of the $3d \rightarrow 2p$ X-ray transition in kaonic ${}^3\text{He}$. In the last line, the resulting strong interaction shift is presented, in comparison to the published value.

4.6 Yields in gaseous kaonic helium

The absolute yield of an atomic state is determined by:

$$\text{Absolute Yield} = \frac{\text{no. of X-rays to the state}}{\text{no. of captured kaons}} \quad (4.5)$$

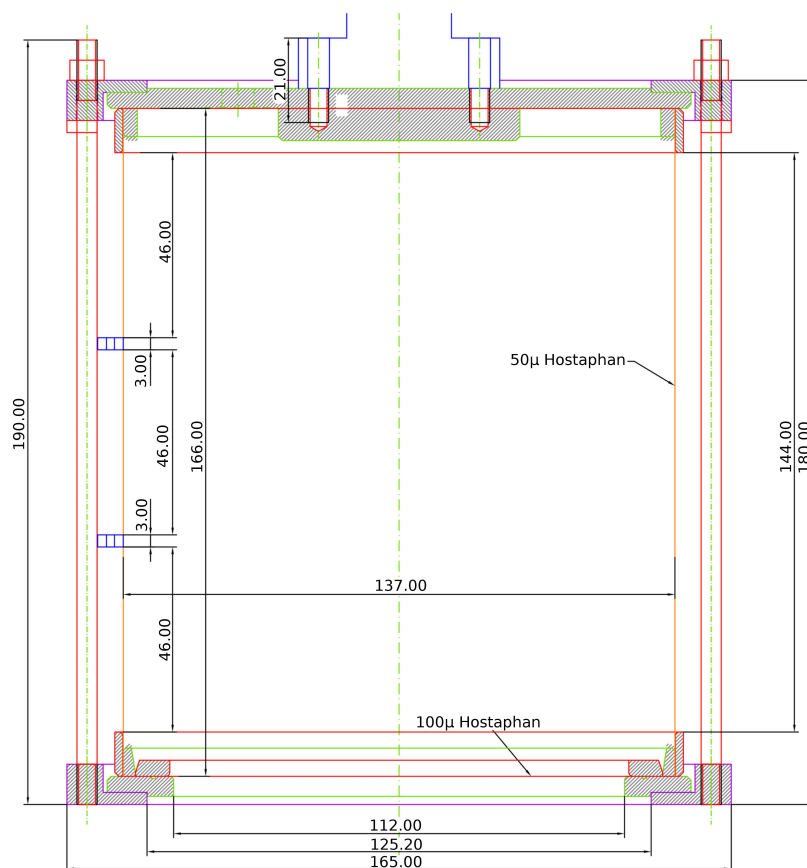
With a Monte Carlo simulation, the total number of X-rays detected by the SDDs in the SIDDHARTA setup was calculated for a theoretical yield of 100 %. Since the simulation includes all experimental factors which may reduce the measured number of X-rays, the calculation of the absolute yield of an atomic state is simplified to:

$$\text{Absolute Yield} = \frac{\text{measured no. of entries in the X-ray peak}}{\text{calculated no. of entries in the X-ray peak for a yield of 100 \%}} \quad (4.6)$$

The number of entries in an X-ray peak basically is equal to its peak area in the energy spectrum of the SDDs, which is discussed in section 4.6.2. In the following, the calculations of the simulated number of X-rays and of the peak areas are described.

4.6.1 Number of X-rays from the Monte Carlo simulation

The **X-ray detection efficiency**, i.e. the number of kaonic helium X-rays detected by the SDDs per kaon event in the kaon detector, was determined via a Monte Carlo simulation. The simulation is based on a code written by M. Cargnelli with *geant3* (see ref. [68]), which allows the simulation of particle trajectories and energy losses in materials. For a theoretic yield of 100% in each state, the X-rays of the $3d \rightarrow 2p$, $4f \rightarrow 2p$ and $5g \rightarrow 2p$ transitions in kaonic ^3He and ^4He , respectively, were simulated in the SIDDHARTA setup. The main features of the simulation are presented in the following four subsections.



Beam pipe

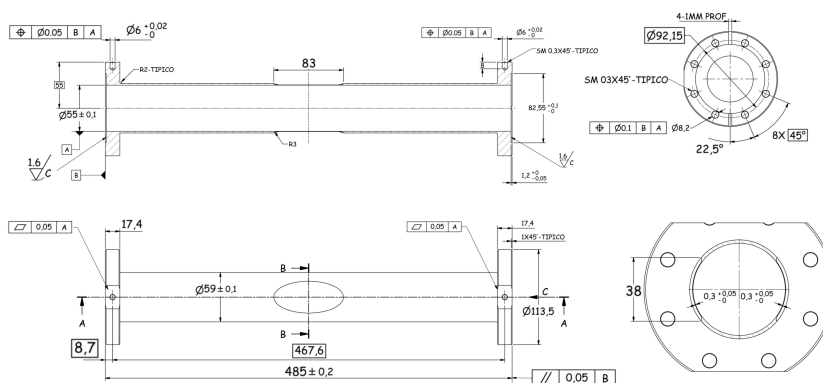


Figure 4.21: Technical drawing of the target cell (top) and the beam pipe beyond the target cell (bottom) with a convex extraction window in the center.

Setup parameters

A virtual setup was generated by inserting the geometric parameters of the SIDDHARTA setup in the program code, including the distances and thicknesses of all setup components, i.e. of the target cell and its surrounding, the carbon degraders, the shielding, the beam pipe around the e^+e^- interaction point and the detectors.

The target densities, which are 0.96 g/dm^3 for ^3He and 1.65 g/dm^3 for ^4He , were determined volumetrically with an error of 2 % from the volume of the target cell and the measured pressure of the filled gas.

In a first step, the dimensions and the material properties of the beam pipe, the degrader, the collimator⁵, the target cell and the vacuum chamber were taken from the technical drawings used for the manufacturing processes, which are presented in fig. 4.21 for the target cell and the beam pipe. The thicknesses of the Kapton foils used for the entrance window of the vacuum chamber and for the target cell are given by the manufacturer.

The final optimizations of the virtual setup dimensions to the real ones happened via the implementation of a *virtual foil* located in front of the degrader, in order to overcome unknown charge loss processes caused by impurities in the materials or uncertainties in the thicknesses. For this purpose, the simulated number of X-rays in kaonic ^4He and ^3He were determined as a function of the virtual foil thickness.

The obtained result was then compared to an experimental measurement on ^4He , which was performed before the SIDDHARTA runs in November 2009. As already described in section 4.2, the degrader thickness in the real setup was optimized in order to maximize the number of stopped kaons in the helium target. The result is presented in fig 4.22(a), where the measured number of X-rays is shown as a function of the degrader thickness. The arrow shows the chosen degrader thickness which was used for all further experiments. The measured values within the gray rectangle fluctuate about 7 % which is taken as the error of this measurement. Note that a different target density of 2.15 g/dm^3 was used for this experiment.

⁵located between degrader and entrance window of the target cell

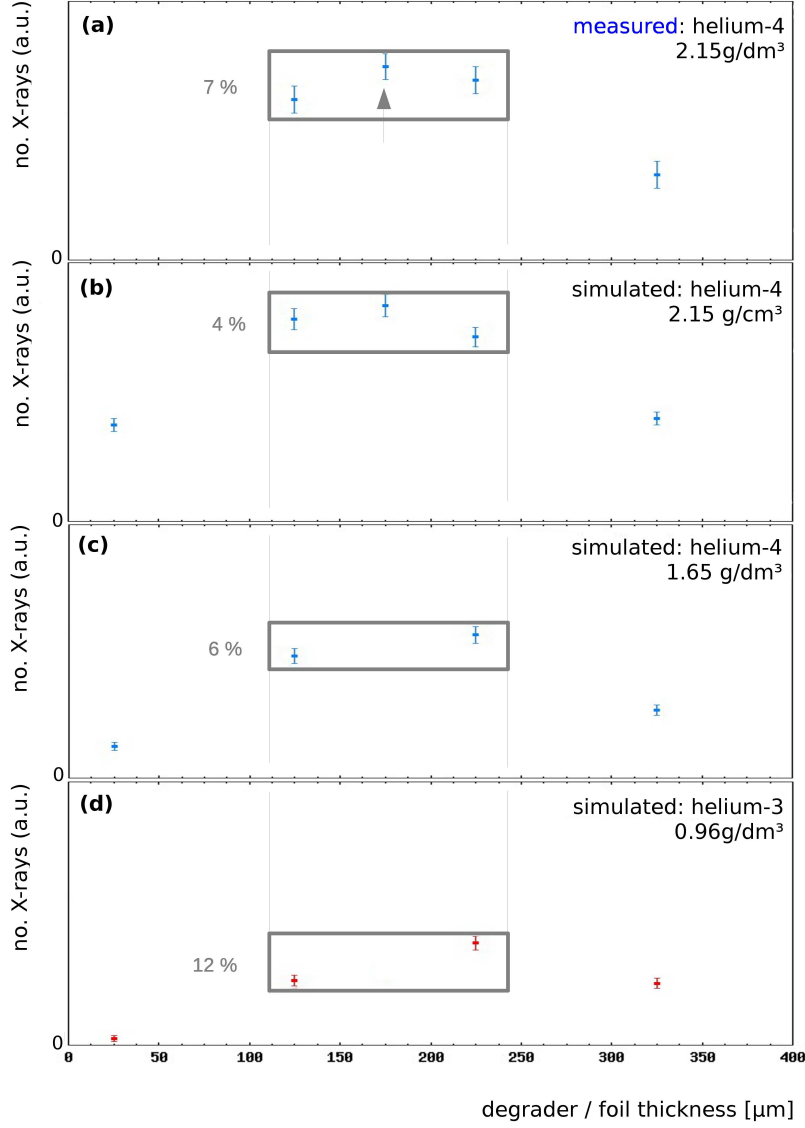


Figure 4.22: Number of measured $3d \rightarrow 2p$ X-rays (denoted as L_α) in kaonic ^4He (density: 2.15 g/dm^3) as a function of the carbon degrader thickness (a). Simulated number of X-rays of the $3d \rightarrow 2p$ X-rays as a function of the virtual foil thickness in (b) kaonic ^4He , density: 2.15 g/dm^3 , (c) kaonic ^4He , density: 1.65 g/dm^3 and (d) ^3He , density of 0.96 g/dm^3 . It is important to mention that the displayed degrader thicknesses only gives the offsets to that value which corresponds to a virtual foil thickness of $0 \text{ } \mu\text{m}$.

In comparison, the simulated number of X-rays as a function of the

virtual foil thickness is shown for ^3He and ^4He at different densities in fig 4.22(b-d). The simulated number of X-rays shows the same behavior than the measured one. Based on the experimental determination of the optimum degrader thickness, the optimum of the foil thickness was taken at the mean value of the simulated values within the gray rectangles. The percentages on the left hand give the fluctuations of the simulated number of X-rays within the rectangles.

Detectors

The sizes of the SDDs and the kaon detector were taken from technical drawings.

In case of the kaon detector, the densities of the scintillators were taken from the manufacturer, the densities of their wrapping (light tight PVC tape) was determined via weighing. The kaon detector covers a solid angle of 8 %, its intrinsic detector efficiency is 100 % for the kaons.

The intrinsic detector efficiency of the SDDs is 100 % for X-rays with an energy below 8 keV and around 97 % for 10 keV X-rays. Note that the number of SDDs used in the simulation was set to 100, i.e. the result of the simulation - the **X-ray detection efficiency** - was obtained for SDDs with a total area of 100 cm² surrounding cylindrically the target cell.

The intrinsic detector efficiencies were calculated via the Beer-Lambert law for both detector types: the attenuation of X-rays in materials with an initial intensity I is given as:

$$I = I_0 \cdot e^{-\mu d} \quad (4.7)$$

with I_0 as the initial intensity, μ as the material dependent absorption coefficient and d as the covered distance in the material. The values for the according absorption coefficients were taken from the Photon Cross Sections Database (XCOM), see ref. [69].

Simulation process

The simulation starts with the creation of Φ -mesons ($m_\Phi = 1020$ MeV) and their decay products at the interaction point of the beam pipe, where all decay particles with branching ratios higher than 5 % are produced including

the K^+K^- -pairs. Since the diameter of the beam profile in the interaction point varies between 1 cm and 2 cm within one injection cycle, the mean value of the beam diameter (1.5 cm) was chosen. From an arbitrary number of created Φ -mesons, the trajectories, energy losses and decays of all Φ -decay particles permeating the virtual setup are simulated with *geant3*. The number of the K^- stops in all materials and in particular in the gas target are then obtained, which is illustrated in fig. 4.23.

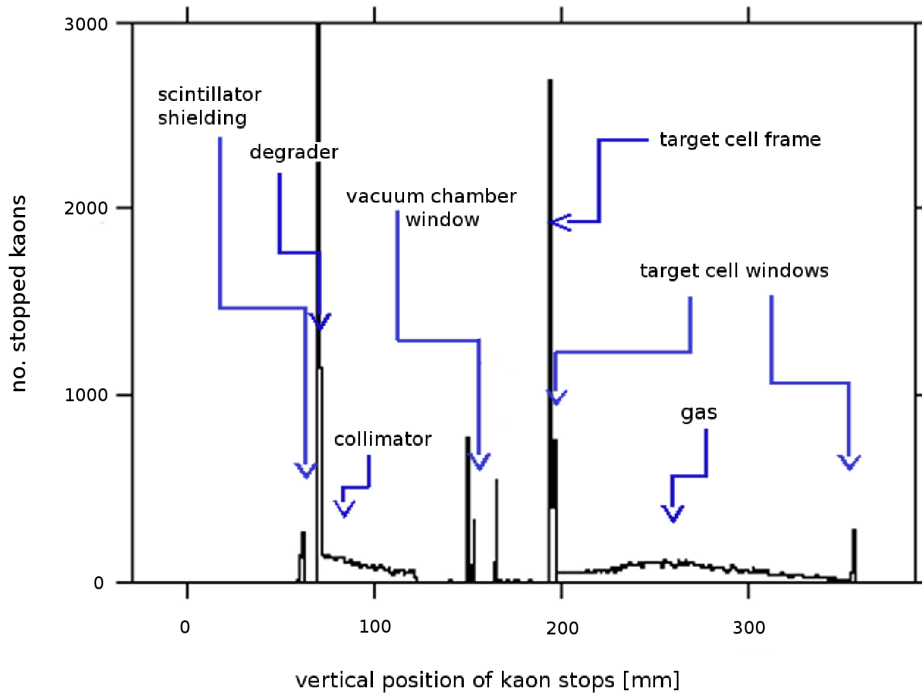


Figure 4.23: Number of simulated kaon stops in the materials of the SIDDHARTA setup.

The determination of the number of low-energy X-rays arising from atomic X-ray transitions after a kaon capture necessitates an artifice due to the limitations of *geant3*, inhibiting calculations at energies below 10 keV: A neutral dummy particle ("geantino") with an appropriate energy is created instead of an X-ray. Further interactions of this particle with the surrounding material are then calculated independently via the Beer-Lambert law (equation 4.7) for the attenuation of electromagnetic radiation in matter.

The number of created geantinos per affected atom (i.e. the yield) was set to 100 % for kaonic atoms.

The attenuation of X-rays in the materials between their creation point in the target gas and SDDs arise from their permeation through the gas and the Kapton foil of the target cell. The calculated attenuation is around 5 % for X-ray energies between 6 keV and 10 keV. Since the differences in the intrinsic detector efficiency for these X-ray energies is negligible, the resulting calculated X-ray detection efficiencies of the kaonic helium $3d \rightarrow 2p$, $4f \rightarrow 2p$ and $5g \rightarrow 2p$ transitions are equal. Consequently, the different peak intensities of the kaonic helium transitions in the measured spectra solely arise from different yields.

Errors

The error of the Monte Carlo simulation includes the statistical error of the simulation, uncertainties of the material budget and the geometry, the error of the gas density measurement, as well as fluctuations of the beam. However, the total error was determined from different simulation results, where sequentially certain input parameters were varied within their uncertainties while the other parameters kept unchanged.

The uncertainties of the material budget are compensated by the thickness of the virtual foil, which was varied within the experimentally estimated range presented in fig. 4.22. The beam diameter fluctuated between 1 and 2 cm, the collision angle between 50 and 55 mrad. Further smaller contributions are e.g. fluctuations in the kaon energy due to the beam energy spread which is around 0.04 % of the Φ mass, uncertainties of several setup distances or the exact height of the collision point. The contributions to the errors are listed in table 4.3, where also the impacts on the simulated X-ray detection efficiencies for ^3He and ^4He are given. In order to cover further unknown contributions, the quadratically summed total errors of ^3He and ^4He were rounded up to 20 % each.

error source	^3He	^4He
statistical error simulation	4 %	4 %
material thickness	12 %	6 %
gas density	3 %	3 %
size of the e^+e^- collision zone	7 %	7 %
size of the e^+e^- collision angle	7 %	7 %
sum of further contributions	8 %	8 %
total error	18 %	15 %

Table 4.3: Main contributions to the errors of the Monte Carlo simulation. For a detailed description, see text.

The simulation records each simulated kaon permeating the virtual kaon detector, as well as the processes followed by such an event. From this, the **X-ray detection efficiencies**, i.e. the simulated number of detected X-rays per detected kaon, is obtained for the 100 SDDs (each with an area of 1 cm^2) in the virtual setup. Note that the X-ray detection efficiency was only determined for X-ray energies between 6 keV and 10 keV where the attenuation through the setup and the intrinsic detector efficiency of the SDDs is constant.

In an analogous manner, the real kaon detector registers the permeating kaons during the experiment, from which the kaon-correlated X-ray events are then selected. The total number of real kaons counted during the measurement was calculated by summarizing the relevant kaon detector entries in the production data files. The error is purely statistical.

These two quantities allow a determination of the **simulated total number of X-rays** which should reach the SDDs in the experiment if the yields were 100 %: The simulated X-ray detection efficiency was multiplied with the measured number of kaons in the experiment. The results of the X-ray detection efficiency for an arbitrary X-ray transition between 6 keV and 10 keV with an assumed yield of 100 % and an SDD area of 100 cm^2 are presented in table 4.4 for the runs on ^3He and ^4He . The **total theoretical number of X-rays** was then calculated for 92 SDDs with propagated error. The X-ray detection efficiencies in ^3He and ^4He were obtained with a simulation of $\sim 10^6$ produced kaons in both cases.

gas	density	simulated X-ray detection efficiency	real number of registered kaons	total no. of X-rays
^3He	0.96 g/l	$(2.69 \pm 0.54) \cdot 10^{-3}$	1716775 ± 1310	4249 ± 924
^4He	1.65 g/l	$(3.76 \pm 0.75) \cdot 10^{-3}$	556107 ± 746	2091 ± 418

Table 4.4: X-ray detection efficiencies and calculated no. of X-rays for ^3He and ^4He with a theoretic yield of 100 %.

4.6.2 Peak areas

The peak areas were obtained from the Gaussian fits of the X-ray transitions of interest in the energy spectrum of the coincidence data files (section 4.5.2). Nevertheless, the values of the peak areas have to be corrected since not all X-rays reaching the SDDs are detected. The calculation of the number of those lost events is described in the following two sections.

Lost events due to drift time selection

To obtain the final ^3He and ^4He energy spectra extracted from the kaon-correlated SDD events, a careful selection process with the slewing corrected TDC data was performed, as described in section 4.5.2. Only the SDD events contributing to the drift time distribution peak in the TDC time spectra were selected. Since the events in the tails of this distribution are hardly separable from background events, events with longer or shorter drift times were cut off. These rejected events nevertheless contribute to the X-ray peak of a helium transition and are thus lost events. Assuming that the background events in the TDC spectra do not contribute to the X-ray peaks of the kaonic helium transitions, the number of lost events was evaluated by counting the entries in the background-subtracted drift time distribution above ($>$ channel 560) and below ($<$ channel 380) the selection threshold. These events are schematically highlighted in red in fig. 4.24. The thresholds are identical for ^3He and ^4He . The number of lost events in the peaks of the kaonic X-ray transition was found to be $(6.8 \pm 1.5) \%$ of the events in the accepted area for ^3He and $(2.3 \pm 1.2) \%$ of the accepted events for ^4He .

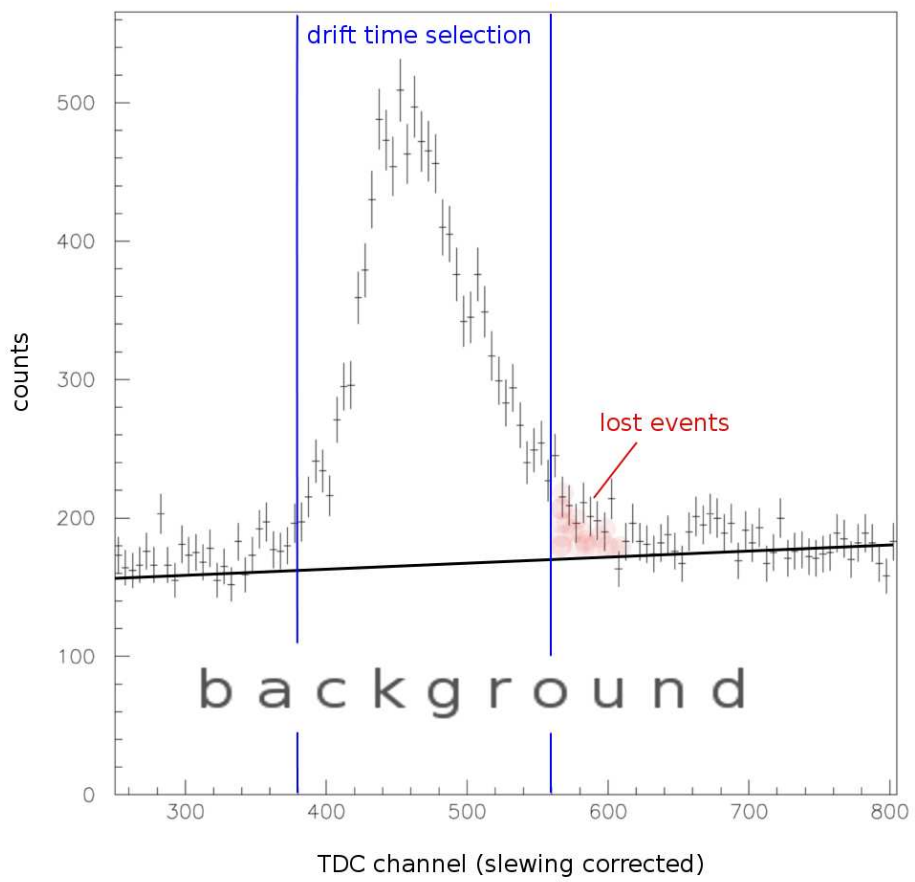


Figure 4.24: TDC spectrum of the time difference between SDD and kaon detector events. The blue lines mark the drift time selection threshold at channel 380 and channel 560, respectively. The events contributing to the drift time peak but located beyond of the thresholds are lost events in the energy spectrum.

Lost events due to SDD breaks

During the measurements, the SDDs temporarily did not collect data for two reasons. On the one hand, the discharging process of an SDD, controlled via an external reset pulse, caused a periodical data collection break for a few seconds in each SDD. On the other hand, a latch-up effect occurred in the SDDs every now then. This is a low-impedance state of the FET caused by irradiation at high rates. Due to adequate protective mechanisms this effect could be overridden by turning off the affected SDD which resulted in a data collection break for several minutes.

Events occurring during these breaks are therefore lost and have to be calculated. Therefore, the energy data of the high-rate self-trigger production data were investigated over the measurement time, which was recorded in each file. An example is presented in fig. 4.25: The recorded energy events of two SDDs with IDs 118 (green) and 329 (blue) are displayed as a function of the measurement time over the data taking period in one file. The measurement time was recorded in units of 0.1 s. The SDDs have short data collection breaks during their discharging sequence, controlled externally for all SDDs simultaneously. Due to the latch-up effect, the detector with ID 329 had a data collection break for several minutes until it was turned on again.

The average of the recorded events per time unit during a working period was calculated for each SDD and for each file. The number of lost events during the break period was then determined by multiplying this value with the time interval of the break. Statistically, no entries in the SDDs during the working period are possible. Thus, a break was defined as a period of at least one second without any entries in the SDD. In the ^3He files, the lost events in the SDD energy data correspond to $(11.4 \pm 0.8) \%$ in average of the recorded events. In case of ^4He , the lost events are $(10.7 \pm 1.2) \%$ of the recorded events. Both errors are purely statistical.

A geometric evaluation of the number of (corrected) recorded events per SDD showed that the number of entries is independent of the position of the SDD. Especially along the rotation axis of the target cylinder no significant differences in the SDDs' entries was found.

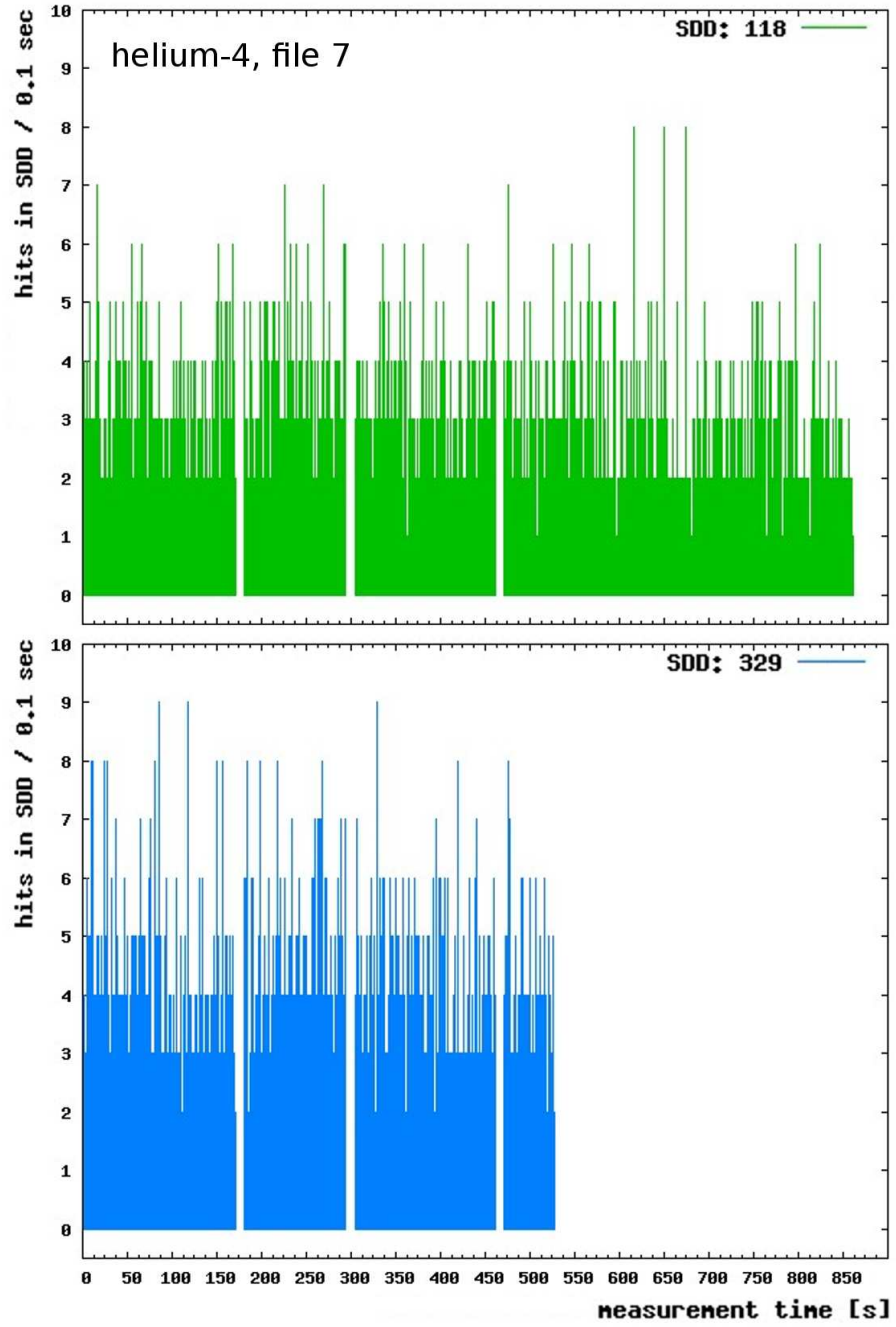


Figure 4.25: Entries of the kaon-uncorrelated data in two SDDs as a function of the measurement time in one file. The breaks arise from the periodic discharging process and, in case of the SDD 329, from the latch-up effect.

4.6.3 Absolute and relative yields

Table 4.5 lists the absolute yields of the $3d \rightarrow 2p$, $4f \rightarrow 2p$ and $5g \rightarrow 2p$ X-ray transition in kaonic ^3He and ^4He including all corrections due to lost events. The error of the peak area was obtained by the fit, the error of the calculated X-rays from the Monte Carlo simulation was estimated to 20 %.

	^3He : 0.96 g/dm ³			^4He : 1.65 g/dm ³		
	$3d \rightarrow 2p$	$4f \rightarrow 2p$	$5g \rightarrow 2p$	$3d \rightarrow 2p$	$4f \rightarrow 2p$	$5g \rightarrow 2p$
area _{fit}	839.3±60.9	123.9±17.6	47.8±13.8	346.4±48.1	68.7±26.1	19.6±17.0
corr. L	0.114±0.008			0.107±0.012		
corr. D	0.068±0.015			0.023±0.012		
area _{corr}	992.6±73.5	146.5±20.9	56.6±16.4	391.5±54.7	77.6±29.5	22.1±19.2
X-rays	4249±924			2091±418		
Yield (%)	23.4±5.4	3.5±0.9	1.3±0.5	18.7±4.6	3.7±1.6	1.1±0.9

Table 4.5: Lines from top to bottom: Peak area from the fit (area_{fit}), correction factor due to the latch-up break (corr. L), correction factor due to the drift time selection (corr. D), corrected area (area_{corr}), number of X-rays with a yield of 100 % taken from the simulation, absolute yields.

The yields of the $4f \rightarrow 2p$ and $5g \rightarrow 2p$ transitions, relative to the $3d \rightarrow 2p$ transition have also been calculated by dividing the corresponding corrected peak areas. In fig. 4.26, the absolute and relative yields are displayed.

The absolute yields of the $3d \rightarrow 2p$ transition in ^3He and ^4He differ by about one sigma, which might be an indicator for the density dependence of the yields: Due to the higher density of the ^4He target, enhanced Stark mixing boosts the nuclear absorption of the kaons in high n states, resulting in a reduced yield of the X-ray transitions at lower states. However, this tendency is not perceivable in the $4f \rightarrow 2p$ and $5g \rightarrow 2p$ transitions. The yields relative to the $3d \rightarrow 2p$ transition are equal within errors.

The error of the yields in ^4He are larger due to the smaller data set.

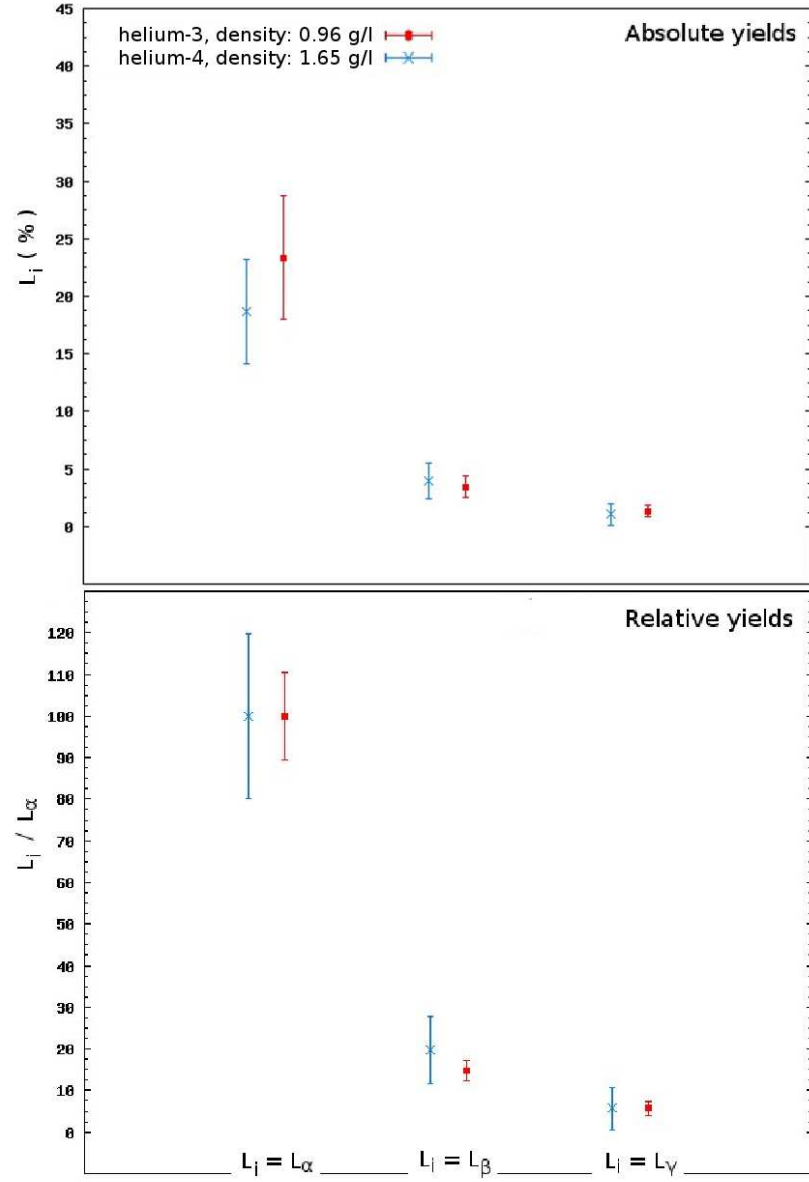


Figure 4.26: Absolute and relative yields in kaonic ^3He (red) and ^4He (blue). The L_α , L_β and L_γ denote the $3d \rightarrow 2p$, $4f \rightarrow 2p$ and $5g \rightarrow 2p$ transitions, respectively.

The method of the calculation of the kaonic helium yields was cross checked with the yields of the transitions in the kaonic atoms appearing in the Kapton foil. Kaons may stop in the foil surrounding the target cell and are captured by the atoms in the foil, forming kaonic oxygen, kaonic nitrogen

and kaonic carbon. Since the foil is positioned directly in front of the SDDs, the detected X-ray transitions of these exotic atoms solely come from the foil. Subsequently their yields - obtained via the method described above - must be independent of the helium target density. The X-ray detection efficiency of the stopped kaons in the foil was determined by the Monte Carlo simulation. In fig. 4.27 the result is presented for the absolute yields of those transitions which are visible in the kaonic helium spectra, having sufficient statistics and with free intensity in their fit function. This is fulfilled by the $6h \rightarrow 5g$ and $5g \rightarrow 4f$ transitions in kaonic carbon and of the $6h \rightarrow 5g$ transition in kaonic oxygen. The absolute yields of the transitions are equal at both targets within errors, confirming that the yields of the Kapton foil are unaffected by the helium target density.

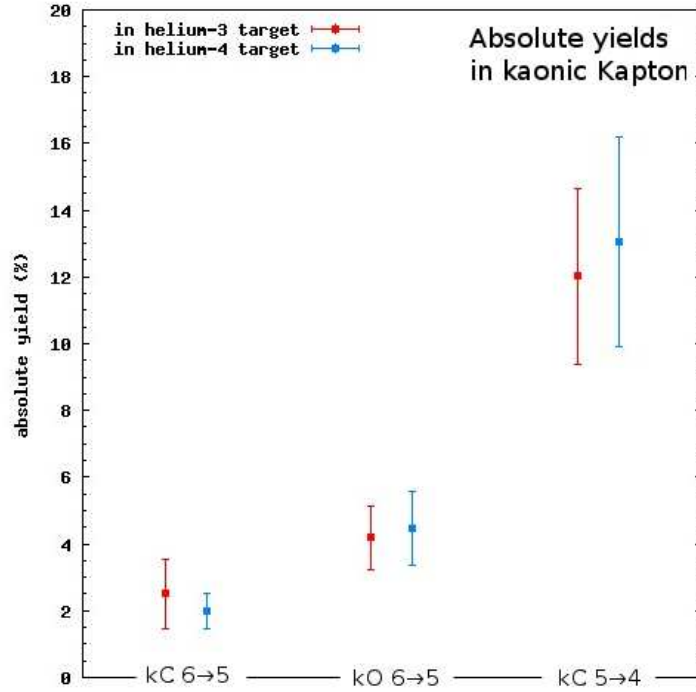


Figure 4.27: Absolute yields of kaonic atoms, formed in the Kapton foil directly in front of the SDDs.

4.7 Conclusion and summary

The yields of the $3d \rightarrow 2p$, $4f \rightarrow 2p$ and $5g \rightarrow 2p$ X-ray transitions in gaseous kaonic ^3He and ^4He were determined with the data set of the SIDDHARTA experiment runs in 2009.

The calibrated SDD data of a ^3He (target density: 0.96 g/l) and a ^4He (1.65 g/l) run were extracted and underwent several procedures in order to reduce background signals. The visible X-ray transitions of kaonic atoms in the final ^3He and ^4He energy spectra were fitted with Gaussian functions. Additionally, the strong interaction shift was determined for kaonic ^3He , which was found to be $(-3 \pm 8(\text{stat.}) \pm 3(\text{sys.}))$ eV, consistent with the published value [45] where a larger data set was used. Furthermore, the peak areas of the kaonic helium X-ray transitions were calculated, including some corrections due to lost events.

Via a Monte Carlo simulation [70] the absolute yields of the kaonic helium transitions were obtained with an error of $\sim 20\%$, coming from uncertainties in the simulation. The absolute yields of the $4f \rightarrow 2p$ and $5g \rightarrow 2p$ show no significant difference between ^3He and ^4He . Nevertheless, the X-ray yields in general decrease with increasing target density due to Stark mixing. This effect may have small impact on the $3d \rightarrow 2p$ transition, where the yield in ^4He is larger by one sigma than the yield in ^3He . Furthermore, the yields of the $4f \rightarrow 2p$ and $5g \rightarrow 2p$ X-ray transitions relative to the $3d \rightarrow 2p$ transition are equal within errors for ^3He and ^4He .

Provided that the yields in ^3He and ^4He (with the same density) are equal, the results of the absolute yields in SIDDHARTA are compared to the published yields of the previous measurements of Wiegand et al. [33] and Baird et al. [35] with liquid kaonic ^4He . In fig. 4.28 (a), the density dependence of the yields due to Stark mixing in gaseous and liquid kaonic helium is obvious in the $3d \rightarrow 2p$ transitions.

The density dependence of the yields in helium was also studied in comparison with various theoretical models, see chapter 2. Fig. 4.28 (b) shows the experimental values of gaseous ^3He and ^4He and of liquid ^4He in comparison with the theoretical results of the cascade calculations by Koike [38]. A description of the model can be found in ref. [39]. The determination of the calculated yields is among others based on the results on the experimentally determined yields and absorption widths in liquid kaonic ^4He by Baird et

al [35]. This may explain the slight discrepancy in the $3d \rightarrow 2p$ transition in gaseous helium between the SIDDHARTA result and the theory. However, the higher transitions as well as the results from liquid helium fit to the model.

In summary, the yield of the $3d \rightarrow 2p$ transition in gaseous helium is higher by a factor of about 2 compared to the ~ 100 times denser liquid helium. This density dependence may also causes a difference in the yields of the $3d \rightarrow 2p$ transitions between the two gaseous targets: the yield of the $3d \rightarrow 2p$ transition in the 1.7 times denser gas is decreased by a factor of ~ 1.3 , which corresponds to an increase of one sigma.

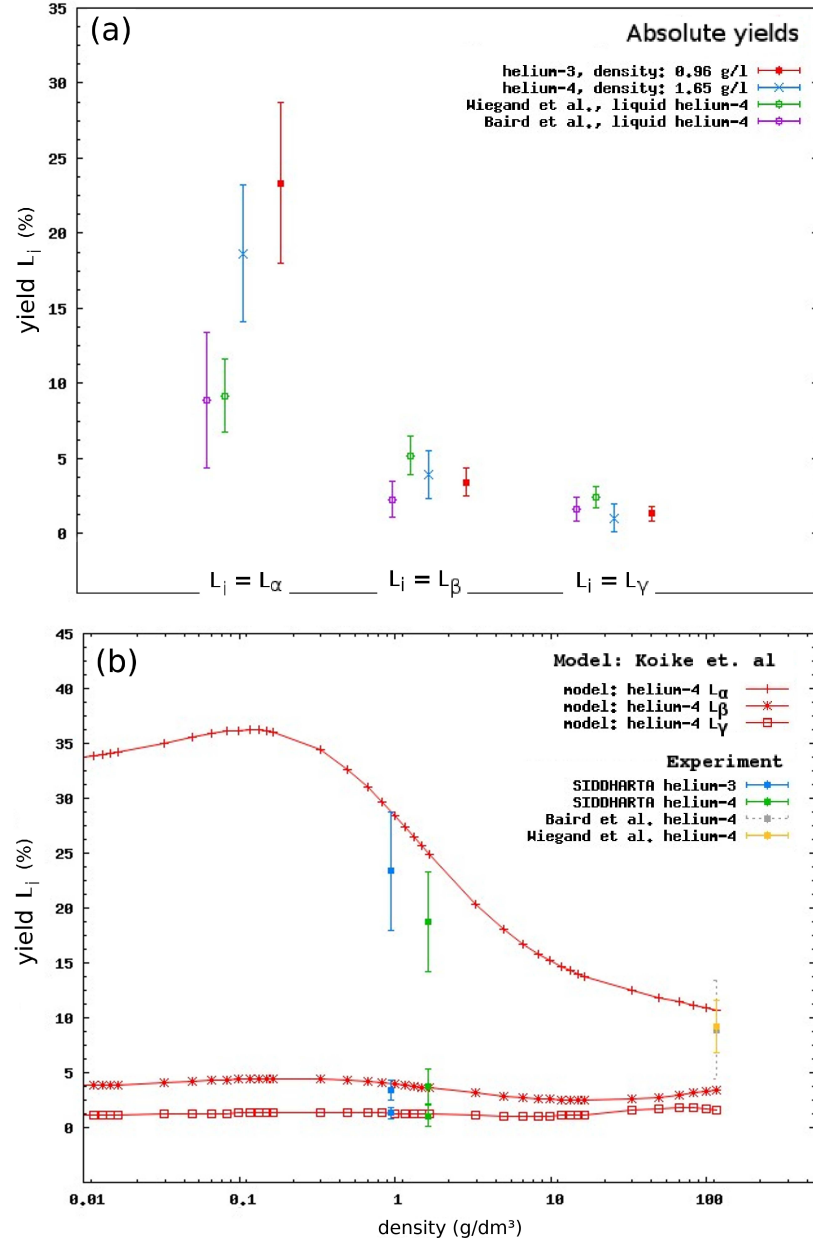


Figure 4.28: The L_α , L_β and L_γ denote the $3d \rightarrow 2p$, $4f \rightarrow 2p$ and $5g \rightarrow 2p$ transitions, respectively. (a): Absolute yields measured of the X-ray transitions in kaonic ^3He (red) and ^4He (blue) by SIDDHARTA in comparison with the yields in liquid ^4He of former experiments [33,35]. (b): Absolute yields of SIDDHARTA and previous experiments in comparison with theoretic calculations by Koike [38]. For the sake of clarity, only the L_α transitions are shown from the previous experiments.

Chapter 5

Kaonic helium with E17

The goal of the E17 experiment, planned after 2012, is the measurement of the kaonic X-ray transitions in liquid ^3He and ^4He with a precision of <2 eV. The experiment will be performed at J-PARC, a proton synchrotron in Tokai, Japan, see section 5.1. The setup was basically adopted from the E570 experiment at KEK [43] and is described in section 5.2. A summary of the experiment is given in refs. [71, 72].

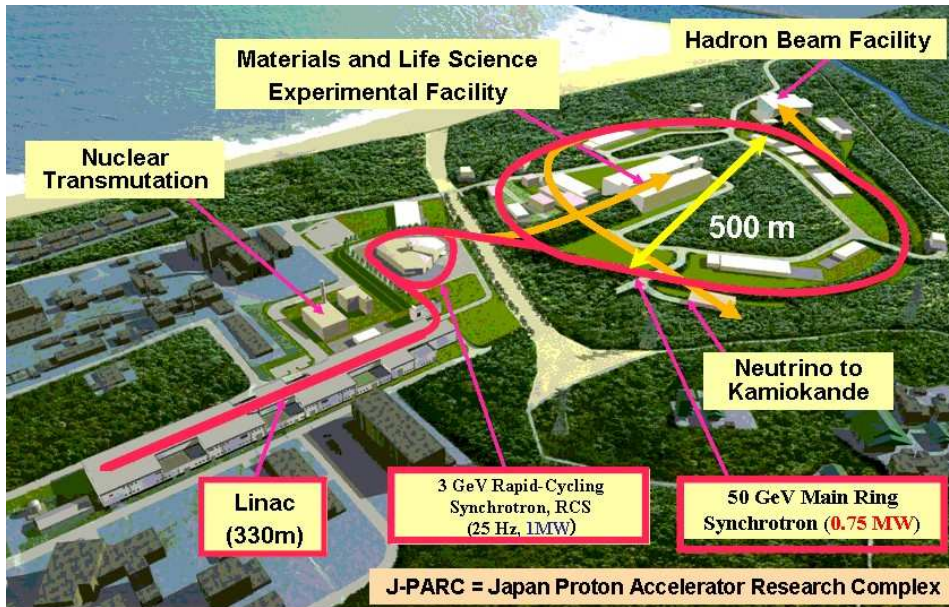


Figure 5.1: Overview over the J-PARC facility in Tokai, Japan. Picture from j-parc.jp/index-e.html

5.1 J-PARC, the facility

J-PARC is a high intensity proton accelerator facility. The complex consists of three accelerators: a Linac for energies up to 600 MeV, a 3 GeV rapid cycle synchrotron (RSC) and a 50 GeV main ring. The high intensity protons from the main ring are used for secondary particle production via target bombardment, e.g. neutrinos for the Kamiokande detector in Japan. The setup of the E17 experiment is located at the end of the K1.8BR beam line in the hadron hall (see northern building in fig. 5.1). At the separation point, the 50 GeV protons are focused on a metal target (Ti or Pb), producing K^+ and K^- with momentum of ~ 0.9 GeV/c. The K^- beam is guided through the K1.8BR beam line where the kaons are separated from other charged particles by a system of magnetic and electric components. The ratio of charged particles (mainly π^- , as well as \bar{p} , μ^- , e^-) to kaons in front of the target cell is about 10:1. A picture of the hadron hall during the construction phase in 2009 is presented in fig. 5.2; the arrow shows the path of the K^- to the position of the E17 setup. The kaons are then stopped in the helium target in the middle of the setup. The beam tuning of the K^- beam with beam intensities of 1 to 10 kW was successfully finished in 2011.



Figure 5.2: Photograph of the K1.8BR beam line in the hadron hall during the construction phase.

5.2 E17 setup

The setup used for E17 is presented in fig. 5.3.

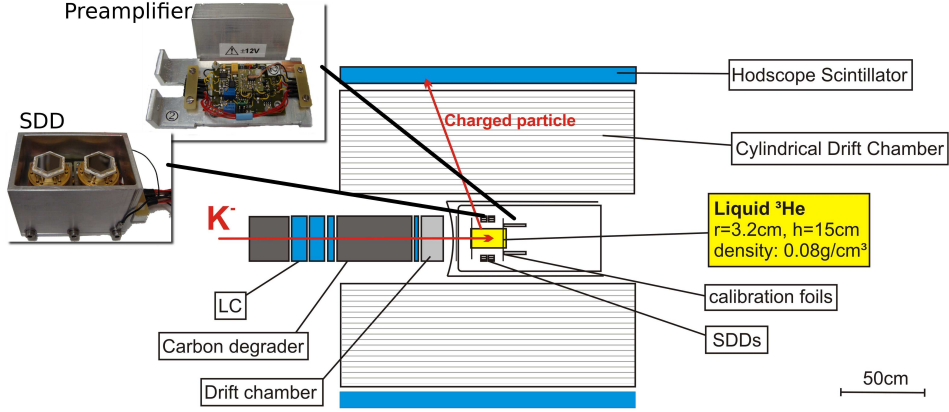


Figure 5.3: Schematic view of the E17 setup. The position of the SDDs and the preamplifiers is also indicated.

The kaons enter the inner cylindrical cryostat, containing the SDDs and the target cell, via a Mylar window. The target cell is a Be cylinder with a radius of 3.2 cm and a height of 15 cm. It is filled with liquid helium with a density of 80 g/l and kept at a temperature of about ~ 2 K. It is surrounded by a cylindrical detector system (CDS) in order to reduce background and to measure the kaonic X-ray transitions. The features of the setup are listed below.

Beam identification: The K^- having an initial momentum of about 0.9 GeV/c are stopped in the target by a carbon degrader, located in front of the cryostat between the beam line drift chamber and the Lucite Cerenkov counter (LC). This Lucite Cerenkov counter identifies the kaons which allows to distinguish them in the offline analysis from other negatively charged particles and to reject kaon-uncorrelated X-ray events.

Fiducial volume cut: Via particle tracking, the events only occurring in the helium target can be selected. First, the timing and the trajectories of the K^- are measured by a counter and a beam line drift chamber when the kaons are passing through the degrader. Second, the cylindrical drift chamber (CDC) and the scintillator hodoscope counters surrounding the CDC identify the secondary charged particles which are produced when the kaons are absorbed by the helium nucleus. Together with the K^- trajectories, the reac-

tion vertex can be reconstructed ("fiducial volume cut"). This allows a selection of the reaction volume of interest in the offline analysis and therefore a rejection of kaon-correlated events from the material of the target cell or outside. The cylindrical detector system covers an angle of about 2.5π ; a 3D model is presented in fig. 5.4, where the yellow part marks the hodoscope and the light blue part the CDC.

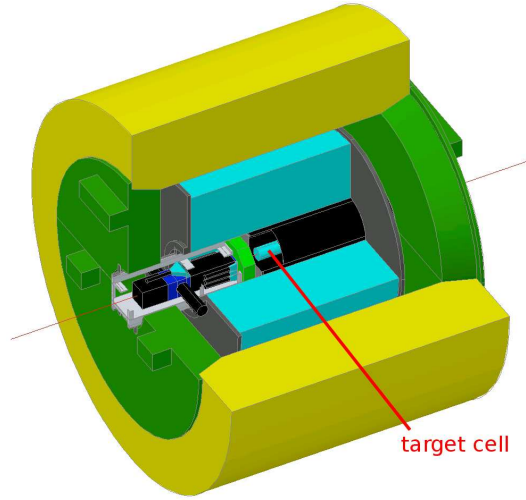


Figure 5.4: Model of the CDS. The cylindrical target cell is located in the middle, surrounded by a CDC (light blue). The carbon degraders are shown in black.

Silicon drift detectors: For the detection of the X-rays from the kaonic helium transitions, eight hexagonally shaped SDDs (area: 1 cm² each) are arranged very close around the target cell, covering a solid angle of about ~ 1 %. For a detailed description of the characteristics of the SDDs see chapter

3. The housings of the preamplifiers and of the SDDs, the latter containing two SDDs each, are covered with a Kapton foil and equipped with a temperature sensor and a heater. A picture of the housings is presented in fig. 5.3, where also their positions in the cryostat are indicated. As one can see in fig. 5.5, which shows a drawing of the cryostat, the SDDs are separated from their preamplifiers due to the limited size of the cryostat. To reduce heat transfer from the SDDs to the target cell, they are kept at a low temperature of < 130 K. The temperature behavior of the SDDs' response function under these conditions was studied extensively, which is reported in chapter 3. Similar to the SIDDHARTA experiment, also the time information of the SDDs is recorded via a coincident measurement, allowing to select the kaon-correlated X-ray events. In a first functionality test of the SDDs in the setup was successfully performed in November 2010 with a measurement of the characteristic X-rays of the calibration foils excited by the pions in the kaon beam.

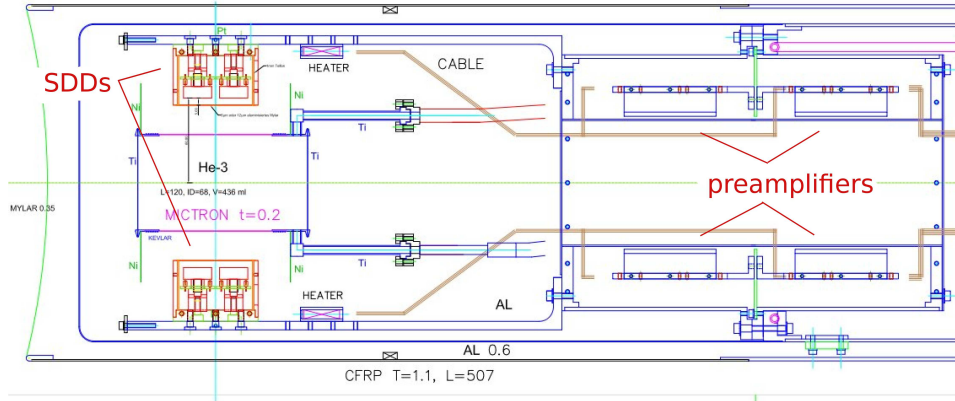


Figure 5.5: Technical drawing of the cryostat, showing the SDD arrangement around the target cell. Due to space limitation, the preamplifiers are separated from the detectors via cables with a length of ≈ 30 cm.

Calibration: An in-situ calibration of the SDDs is essential for reaching a precision of less than 2 eV. Ni (K_α at 7.5 keV) and Ti (K_α at 4.5 keV) foils are installed around the target cell, from which characteristic X-rays are excited constantly by the particles contaminating the beam (mainly π^-). Via a selection of kaon-uncorrelated events, these X-ray spectra can be evaluated separately at any time of the measurement.

Chapter 6

Conclusions and summary

In this thesis, important contributions were made for two experiments on kaonic helium: the study of the response function of silicon drift detectors at low temperatures and with separated preamplifiers for the E17 experiment, as well as the determination of the transition rates (yields) in gaseous kaonic ^3He and ^4He from the SIDDHARTA experiment. This is summarized and discussed in the following.

The experimental part of the thesis is dedicated to silicon drift detectors (SDDs), which are state-of-the-art silicon detectors optimized for X-ray spectroscopy. Due to the requirements of the E17 experiment, an investigation of the temperature behavior of the SDDs used for this experiment was necessary. These SDDs are hexagonally shaped with an active area of 1 cm^2 and a thickness of $450\text{ }\mu\text{m}$. They are mounted separated from their preamplifiers in the E17 setup and kept at low temperatures. The energy resolution and the drift time distribution were studied as a function of temperature under similar conditions. For these experiments, the Mn K_α X-rays from an ^{55}Fe and the electrons from an ^{90}Sr source were used.

The **energy resolution** was found to be constant with 150 eV FWHM at 5.9 keV between SDD temperatures from 130 K to 200 K. It is also unaffected by preamplifier temperatures between 240 K and 300 K.

In contrary, **the position of the peak center** at an X-ray energy of 5.9 keV increases linearly above SDD temperatures of 130 K with about 0.6 eV/K. The result can be understood with the temperature dependence of the electron-hole pair creation energy in silicon, because the position of a

peak center is related to the number of produced electron-hole pairs in silicon. The latter also shows a corresponding shift of 0.6 eV/K.

The peak position is also influenced by temperature variations of the preamplifiers: it changes linearly with temperature by 0.5 eV/K. Both results on the peak position behavior clearly show that the temperatures of the preamplifiers and of the SDDs have necessarily to be controlled within 1 K in order to keep the peak position stable within 0.5 eV.

The **drift time distribution** of the SDDs was measured via a coincidence measurement with a PIPS detector as a function of the SDD temperature. The FWHM of the measured SDD time distribution was found to be 400 ns at 120 K and 1100 ns at 200 K. It increases with a T^n (with $n = 3.00$) function between SDD temperatures from 120 K to 200 K.

This effect is attributed to the temperature dependence of the electron mobility, since the drift time is related to the mobility of electrons in silicon. For this purpose, a simple model of the E17-SDDs was developed from which the drift time distribution was calculated with the electron mobility and compared to the measured values. Furthermore, the obtained electron mobility is in good agreement with the literature value.

In summary, the optimum SDD temperature was found to be 130 K in order to obtain an optimum energy resolution and drift time resolution. Since the preamplifiers show a different behavior below 170 K, they are kept at temperatures higher than 170 K.

Finally, via a simulation, the SIDDHARTA-SDDs and the E17-SDDs were compared by the shape of their drift time distributions, which are mainly affected by the shape of their surface areas.

The analysis part of this thesis concentrates on the evaluation of the X-ray yields from the SIDDHARTA experiment, which investigated the X-ray transitions in gaseous kaonic ^3He and ^4He at the DAΦNE facility in Frascati, Italy. During the experiment, special developed SDDs similar to the E17-SDDs have been used for the X-ray detection. A complex detector system allowed an efficient background suppression in the offline analysis.

Altogether 92 SDDs, surrounding the target cell, have been chosen for the analysis. A selection of solely kaon-correlated X-ray events in the SDDs was obtained from a coincidence measurement between the SDD and kaon detector signals. For a calibration of the SDDs, characteristic X-rays from

metal foils were excited periodically. In order to calculate the yields of the $3d \rightarrow 2p$, $4f \rightarrow 2p$ and $5g \rightarrow 2p$ X-ray transitions in kaonic ^3He and ^4He , the data of the ^3He and ^4He runs with different gas densities were evaluated. After the calibration of the chosen SDDs, the kaon-correlated raw energy data of the ^3He (target density: 0.96 g/l) and the ^4He (1.65 g/l) run underwent a correction and selection procedure in order to suppress further background. In the final energy spectra, the visible X-ray peaks were fitted with Gaussian functions.

In order to cross check the evaluation procedure, the difference between the calculated electromagnetic value and the measured value (strong interaction shift) of the $3d \rightarrow 2p$ X-ray transition of the 2p state in ^3He was determined. The purely electromagnetic values of the transitions to the 2p level in kaonic ^3He were calculated from the solution of the Klein-Gordon equation including the Uehling correction for the vacuum polarization, which was found to be 6224.7 eV for the $3d \rightarrow 2p$ transition. The strong interaction shift was then calculated to $(-3 \pm 8(\text{stat.}) \pm 3(\text{sys.}))$ eV which is consistent with the recently published value.

For the determination of the yields, the according X-ray peak areas in the spectra have been extracted. Due to lost events from the selection procedure and operation characteristics of the SDDs, some corrections were applied. The absolute yields were then obtained with inputs from a Monte Carlo simulation. The simulation starts at the K^+K^- creation point in the beam line and calculates all particle tracks through the virtually generated SIDDHARTA setup. Material uncertainties were compensated by the implementation of a virtual foil which was optimized according to experimental studies dealing with the dependence of the detected X-rays on the degrader thickness. Due to further uncertainties in e.g. the beam parameters or gas density measurements, the total error of the simulation is 20 %.

For the $3d \rightarrow 2p$ transitions, an absolute yield of ~ 24 % was found for ^3He and ~ 19 % for ^4He . A comparison showed no clear difference between ^3He and ^4He , neither in the absolute nor in the relative yields. Solely the absolute yields of the $3d \rightarrow 2p$ transitions in ^3He and ^4He differ by about one sigma. This is attributed to the different target densities, since Stark mixing causes a density dependence of X-ray yields in lower states. In comparison with theoretical calculations and with results of previous measurements of X-ray yields in liquid kaonic ^4He , a clear density dependence is observable.

Since all previous experiments on the X-ray transitions in kaonic helium used liquid helium targets, these unique results of the yields in gaseous kaonic helium can give important inputs for theoretical models. In comparison with the results of the previous experiments, the yields in gaseous helium are higher by a factor of 2. A possible difference in the yields can principally not be excluded, nevertheless this is not clearly observable within the uncertainties which are in the order of 20 % in both, the relative and absolute yields.

Provided that there is no significant difference between ^3He and ^4He , the yields for the liquid helium target in E17 can be estimated to be 10 %.

Bibliography

- [1] C. J. Batty. Antiprotonic-hydrogen atoms. *Rep. Prog. Phys.*, 52:1165–1216, February 1989.
- [2] C. J. Batty, E. Friedman, and A. Gal. Strong interaction physics from hadronic atoms. *Physics Reports-Review Section Of Physics Letters*, 287(5):385–445, August 1997.
- [3] P. Indelicato. Exotic atoms. *Physica Scripta*, T112:20–26, 2004.
- [4] Particle Physics Booklet (Particle Data Group), July 2010 <http://pdg.lbl.gov/>.
- [5] T. Yamazaki, M. Aoki, M. Iwasaki, R. S. Hayano, T. Ishikawa, H. Outa, E. Takada, H. Tamura, and A. Sakaguchi. Trapping of negative kaons by metastable states during the atomic cascade in liquid-helium. *Physical Review Letters*, 63(15):1590–1592, October 1989.
- [6] J. P. Santos, F. P. Parente, S. Boucard, and P. Indelicato. Energy levels of hydrogenlike kaonic atoms. *Hyperfine Interactions*, 146(1-4):325–329, 2003.
- [7] T. Koike, T. Harada, and Y. Akaishi. Cascade calculation of K^-p and K^-d atoms. *Physical Review C*, 53(1):79–87, January 1996.
- [8] C. J. Batty. Light Kaonic And Antiprotonic Atoms. *Nuclear Physics A*, 508:C89–C98, February 1990.
- [9] D. B. Kaplan and A. E. Nelson. Strange goings on in dense nucleonic matter. *Physics Letters B*, 175(1):57–63, July 1986.

- [10] T. Waas, M. Rho, and W. Weise. Effective kaon mass in dense baryonic matter: Role of correlations. *Nuclear Physics A*, 617(4):449–463, May 1997.
- [11] W. Weise. Antikaon Interactions with Nucleons and Nuclei. *Nuclear Physics A*, 835(1-4):51–58, April 2010.
- [12] N. Kaiser, P. B. Siegel, and W. Weise. Chiral dynamics and the low-energy kaon-nucleon interaction. *Nuclear Physics A*, 594(3):325–345, November 1995.
- [13] E. Oset and A. Ramos. Non-perturbative chiral approach to s-wave $\overline{K}N$ interactions. *Nuclear Physics A*, 635(1-2):99–120, May 1998.
- [14] M. F. M. Lutz and E. E. Kolomeitsev. Relativistic chiral SU(3) symmetry, large-N-c sum rules and meson-baryon scattering. *Nuclear Physics A*, 700(1-2):193–308, March 2002.
- [15] T. Waas, N. Kaiser, and W. Weise. Effective kaon masses in dense nuclear and neutron matter. *Physics Letters B*, 379(1-4):34–38, June 1996.
- [16] T. Kishimoto. Kaonic nuclei excited by the (K^-, N) reaction. *Physical Review Letters*, 83(23):4701–4704, December 1999.
- [17] J. Mares, E. Friedman, and A. Gal. Widths of K-nuclear deeply bound states in a dynamical model. *Physics Letters B*, 606(3-4):295–302, January 2005.
- [18] N. Barnea and E. Friedman. Radial sensitivity of kaonic atoms and strongly bound (\overline{K}) states. *Physical Review C*, 75(2):022202, February 2007.
- [19] T. Hyodo and W. Weise. Effective $\overline{K}N$ interaction based on chiral SU(3) dynamics. *Physical Review C*, 77(3):035204, March 2008.
- [20] Y. Akaishi and T. Yamazaki. Nuclear \overline{K} bound states in light nuclei. *Physical Review C*, 65(4):044005, April 2002.
- [21] N. V. Shevchenko, A. Gal, and J. Mares. Faddeev calculation of a K^-pp quasibound state. *Physical Review Letters*, 98(8):082301, February 2007.

- [22] Y. Ikeda and T. Sato. Resonance energy of the $\overline{K}NN\text{-}\pi$ YN system. *Physical Review C*, 79(3):035201, March 2009.
- [23] T. Yamazaki and Y. Akaishi. Basic \overline{K} nuclear cluster, K^-pp , and its enhanced formation in the $p^+p^- \rightarrow K^++X$ reaction. *Physical Review C*, 76(4):045201, October 2007.
- [24] A. Dote, T. Hyodo, and W. Weise. K^-pp system with chiral SU(3) effective interaction. *Nuclear Physics A*, 804:197–206, May 2008.
- [25] A. Gal, E. Friedman, and C. J. Batty. On the interplay between Coulomb and nuclear states in exotic atoms. *Nuclear Physics A*, 606(1-2):283–291, August 1996.
- [26] M. Krell. Repulsive effects due to the absorption in exotic atoms. *Physical Review Letters*, 26:584, 1971.
- [27] E. Friedman and A. Gal. Narrow deeply bound K- atomic states. *Physics Letters B*, 459(1-3):43–48, July 1999.
- [28] A. Baca, C. Garcia-Recio, and J. Nieves. Deeply bound levels in kaonic atoms. *Nuclear Physics A*, 673(1-4):335–353, June 2000.
- [29] W. Weise and R. Hartle. Chiral SU(3) dynamics and antikaon-nuclear quasibound states. *Nuclear Physics A*, 804:173–185, May 2008.
- [30] Y. Akaishi. Kaonic helium atoms in relation to kaonic nuclear bound states. *Proceeding for International Conference on Exotic Atoms and Related Topics (EXA05)*, edited by A. Hirtl, J. Marton, E. Widmann, and J. Zmeskal, Austrian Academy of Sciences Press, Vienna, pages 45–54, 2005.
- [31] C. J. Batty and R. E. Welsh. Nuclear capture in the atomic cascade of kaonic, antiprotonic and sigma-hyperonic exotic atoms. *Nuclear Physics A*, 589(4):601–608, July 1995.
- [32] S. Hirenzaki, Y. Okumura, H. Toki, E. Oset, and A. Ramos. Chiral unitary model for the kaonic atom. *Physical Review C*, 61(5):055205, May 2000.
- [33] C. E. Wiegand and R. H. Pehl. Measurement of kaonic x-rays from he-4. *Physical Review Letters*, 27(21):1410–&, 1971.

- [34] C. J. Batty, S. F. Biagi, S. D. Hoath, P. Sharman, J. D. Davies, G. J. Pyle, and G. T. A. Squier. Measurement of kaonic and pionic X-rays from liquid-helium. *Nuclear Physics A*, 326(2-3):455–462, 1979.
- [35] S. Baird, C. J. Batty, F. M. Russell, P. Sharman, P. M. Bird, A. S. Clough, K. R. Parker, G. J. Pyle, and G. T. A. Squier. Measurements on exotic atoms of helium. *Nuclear Physics A*, 392(2-3):297–310, 1983.
- [36] T. Koike and Y. Akaishi. Cascade calculation of exotic helium atoms. *Strangeness Nuclear Physics - Proceedings of the APCTC Workshop (SNP'99)*, edited by Il-T. Cheon, S.W. Hong and T. Motoba, World Scientific, (1):272, January 2000.
- [37] S. Z. Kalantari, S. S. Hajari, and M. D. Kelisani. Calculation of cascade processes rates and simulation of the transitions in kaonic helium-4 atom. *Hyperfine Interactions, Online First*, DOI: 10.1007/s10751-011-0537-8, 2011.
- [38] T. Koike. Cascade calculation of K-helium atoms. *private communications*, (1), January 2012.
- [39] T. Koike and Y. Akaishi. Stark mixing in the exotic helium atom cascade process. *Nuclear Physics A*, 639:521c–524c, 1998.
- [40] M. Stearns and M. B. Stearns. Energies of pi-mesonic x-rays. *Physical Review*, 103(5):1534–1544, 1956.
- [41] S. G. Karshenboim, E. Yu. Korzinin, and V. G. Ivanov. The Uehling correction to the energy levels in a pionic atom. *Canadian Journal Of Physics*, 84(3):107–113, November 2006.
- [42] S. G. Karshenboim. Some analytic results on the Uehling correction in a muonic atom. *Canadian Journal Of Physics*, 76:169, 1998.
- [43] S. Okada, G. Beer, H. Bhang, A. Cargnelli, J. Chiba, S. Choi, C. Curceanu, Y. Fukuda, T. Hanaki, R. S. Hayano, M. Iio, T. Ishikawa, S. Ishimoto, T. Ishiwatari, K. Itahashi, M. Iwai, M. Iwasaki, B. Juhász, P. Kienle, J. Marton, Y. Matsuda, H. Ohnishi, H. Outa, M. Sato, P. Schmid, S. Suzuki, T. Suzuki, H. Tatsuno, D. Tomono, E. Widmann, T. Yamazaki, H. Yim, and J. Zmeskal. Precision measurement

- of the $3d \rightarrow 2p$ X-ray energy in kaonic He-4. *Physics Letters B*, 653(5-6):387–391, September 2007.
- [44] M. Bazzi, G. Beer, L. Bombelli, A. M. Bragadireanu, M. Cargnelli, G. Corradi, C. Curceanu, A. d’Uffizi, C. Fiorini, T. Frizzi, F. Ghio, B. Girolami, C. Guaraldo, R. S. Hayano, M. Iliescu, T. Ishiwatari, M. Iwasaki, P. Kienle, P. L. Sandri, A. Longoni, V. Lucherini, J. Marton, S. Okada, D. Pietreanu, T. Ponta, A. Rizzo, A. R. Vidal, A. Scordo, H. Shi, D. L. Sirghi, F. Sirghi, H. Tatsuno, A. Tudorache, V. Tudorache, O. V. Doce, E. Widmann, and J. Zmeskal. Kaonic helium-4 X-ray measurement in SIDDHARTA. *Physics Letters B*, 681(4):310–314, November 2009.
- [45] M. Bazzi, G. Beer, L. Bombelli, A. M. Bragadireanu, M. Cargnelli, G. Corradi, C. Curceanu, A. d’Uffizi, C. Fiorini, T. Frizzi, F. Ghio, B. Girolami, C. Guaraldo, R. S. Hayano, M. Iliescu, T. Ishiwatari, M. Iwasaki, P. Kienle, P. L. Sandri, A. Longoni, J. Marton, S. Okada, D. Pietreanu, T. Ponta, A. Rizzo, A. R. Vidal, A. Scordo, H. Shi, D. L. Sirghi, F. Sirghi, H. Tatsuno, A. Tudorache, V. Tudorache, O. V. Doce, E. Widmann, B. Wunschek, and J. Zmeskal. First measurement of kaonic helium-3 X-rays. *Physics Letters B*, 697(3):199–202, March 2011.
- [46] E. Gatti and P. Rehak. Semiconductor Drift Chamber - an application of a novel charge transport scheme. *Nuclear Instruments & Methods In Physics Research Section A-Accelerators Spectrometers Detectors And Associated Equipment*, 225(3):608–614, 1984.
- [47] E. Gatti, P. Rehak, A. Longoni, J. Kemmer, P. Holl, R. Klanner, G. Lutz, A. Wylie, F. Goulding, P. N. Luke, N. W. Madden, and J. Walton. Semiconductor Drift Chambers. *IEEE Transactions On Nuclear Science*, 32(2):1204–1208, 1985.
- [48] P. Rehak, E. Gatti, A. Longoni, J. Kemmer, P. Holl, R. Klanner, G. Lutz, and A. Wylie. Semiconductor drift chambers for position and energy measurements. *Nuclear Instruments & Methods In Physics Research Section A-Accelerators Spectrometers Detectors And Associated Equipment*, 235(2):224–234, 1985.

- [49] J. Kemmer, G. Lutz, E. Belau, U. Prechtel, and W. Welser. Low capacity drift diode. *Nuclear Instruments & Methods In Physics Research Section A-Accelerators Spectrometers Detectors And Associated Equipment*, 253(3):378–381, January 1987.
- [50] P. Lechner, S. Eckbauer, R. Hartmann, S. Krisch, D. Hauff, R. Richter, H. Soltau, L. Struder, C. Fiorini, E. Gatti, A. Longoni, and M. Sampietro. Silicon drift detectors for high resolution room temperature X-ray spectroscopy. *Nuclear Instruments & Methods In Physics Research Section A-Accelerators Spectrometers Detectors And Associated Equipment*, 377(2-3):346–351, August 1996.
- [51] P. Lechner, C. Fiorini, R. Hartmann, J. Kemmer, N. Krause, P. Leutenegger, A. Longoni, H. Soltau, D. Stotter, R. Stotter, L. Struder, and U. Weber. Silicon drift detectors for high count rate X-ray spectroscopy at room temperature. *Nuclear Instruments & Methods In Physics Research Section A-Accelerators Spectrometers Detectors And Associated Equipment*, 458(1-2):281–287, February 2001.
- [52] T. Eggert, O. Boslau, J. Kemmer, A. Pahke, and F. Wiest. The spectral response of silicon X-ray detectors. *Nuclear Instruments & Methods In Physics Research Section A-Accelerators Spectrometers Detectors And Associated Equipment*, 568(1):1–11, November 2006.
- [53] T. Eggert. The X-ray response of silicon drift detectors. *Advances in X-ray Analysis*, 45, 2005.
- [54] R. Hartmann, D. Hauff, P. Lechner, R. Richter, L. Struder, J. Kemmer, S. Krisch, F. Scholze, and G. Ulm. Low energy response of silicon pn-junction detector. *Nuclear Instruments & Methods In Physics Research Section A-Accelerators Spectrometers Detectors And Associated Equipment*, 377(2-3):191–196, August 1996.
- [55] M. N. Mazziotta. Electron-hole pair creation energy and Fano factor temperature dependence in silicon. *Nuclear Instruments & Methods In Physics Research Section A-Accelerators Spectrometers Detectors And Associated Equipment*, 584(2-3):436–439, January 2008.

- [56] J. L. Campbell, J. A. Maxwell, T. Papp, and G. White. Si(Li) detector lineshapes: Contributions from atomic physics and detector properties. *X-Ray Spectrometry*, 26(4):223–231, July 1997.
- [57] J. L. Campbell, L. McDonald, T. Hopman, and T. Papp. Simulations of Si(Li) x-ray detector response. *X-Ray Spectrometry*, 30(4):230–241, July 2001.
- [58] D. M. Schlosser, P. Lechner, G. Lutz, A. Niculae, H. Soltau, L. Struder, R. Eckhardt, K. Hermenau, G. Schaller, F. Schopper, O. Jaritschin, A. Liebel, A. Simsek, C. Fiorini, and A. Longoni. Expanding the detection efficiency of silicon drift detectors. *Nuclear Instruments & Methods In Physics Research Section A-Accelerators Spectrometers Detectors And Associated Equipment*, 624(2):270–276, December 2010.
- [59] T. Ishiwatari. Silicon drift detectors for the kaonic atom X-ray measurements in the SIDDHARTA experiment. *Nuclear Instruments & Methods In Physics Research Section A-Accelerators Spectrometers Detectors And Associated Equipment*, 581(1-2):326–329, October 2007.
- [60] C. Fiorini, T. Frizzi, and A. Longoni. A CMOS charge preamplifier for silicon drift detectors with on-chip JFET and feedback capacitor. *Nuclear Instruments & Methods In Physics Research Section A-Accelerators Spectrometers Detectors And Associated Equipment*, 568(3):322–328, 2006.
- [61] J. Marton. Exotic Atom Research Using Large Area Silicon Drift Detectors. *Proceedings of the International Symposium On Detector Development For Particle, Astroparticle And Synchrotron Radiation Experiments (SNIC 2006), Menlo Park, California, 3-6 Apr 2006*, (3):0196, June 2006.
- [62] M. Bazzi, G. Beer, L. Bombelli, A. M. Bragadireanu, M. Cagnelli, G. Corradi, C. Curceanu, A. d’Uffizi, C. Fiorini, T. Frizzi, F. Ghio, B. Girolami, C. Guaraldo, R. S. Hayano, M. Iliescu, T. Ishiwatari, M. Iwasaki, P. Kienle, P. L. Sandri, A. Longoni, V. Lucherini, J. Marton, S. Okada, D. Pietreanu, T. Ponta, A. Rizzo, A. R. Vidal, A. Scordo, H. Shi, D. L. Sirghi, F. Sirghi, H. Tatsuno, A. Tudorache, V. Tudorache, O. V. Doce, E. Widmann, and J. Zmeskal. Performance of silicon-drift

- detectors in kaonic atom X-ray measurements. *Nuclear Instruments & Methods In Physics Research Section A-Accelerators Spectrometers Detectors And Associated Equipment*, 628(1):264–267, February 2011.
- [63] B. K. Wuenschek, Y. Fujiwara, T. Hashimoto, R. S. Hayano, M. Iio, S. Ishimoto, T. Ishiwatari, M. Sato, E. Widmann, and J Zmeskal. Temperature dependencies of the energy and time resolution of silicon drift detectors. *unpublished*, (3-4), February 2012.
- [64] K. Seeger. *Semiconductor Physics*. Springer, 1973.
- [65] M. Boscolo, F. Bossi, B. Buonomo, G. Mazzitelli, F. Murtas, P. Raimondi, G. Sensolini, M. Schioppa, F. Iacoangeli, P. Valente, N. Arnaud, D. Breton, L. Burmistrov, A. Stocchi, A. Variola, B. Viaud, and P. Branchini. Luminosity and background measurements at the e^+e^- DAΦNE collider upgraded with the crab waist scheme. *Nuclear Instruments & Methods In Physics Research Section A-Accelerators Spectrometers Detectors And Associated Equipment*, 621:121, 2010.
- [66] M. Bazzi, G. Beer, L. Bombelli, A. M. Bragadireanu, A. Cargnelli, G. Corradi, C. Curceanu, A. d’Uffizi, C. Fiorini, T. Frizzi, F. Ghio, B. Girolami, C. Guaraldo, R.S. Hayano, M. Iliescu, T. Ishiwatari, M. Iwasaki, P. Kienle, P. Levi Sandri, A. Longoni, V. Lucherini, J. Marton, S. Okada, D. Pietreanu, T. Ponta, A. Rizzo, Romero Vidal A., A. Scordo, H. Shi, D.L. Sirghi, F. Sirghi, H. Tatsuno, A. Tudorache, V. Tudorache, O. Vazquez Doce, E. Widmann, and J. Zmeskal. A new measurement of kaonic hydrogen X rays. *Physics Letters B*, 704:113–117, 2011.
- [67] X-ray data booklet 2009 Center for X-ray Optics and Advanced Light Source Lawrence Berkeley National Laboratory.
- [68] M. Cargnelli. *private communications*, 2011.
- [69] M.J. Berger, J.H. Hubbell, S.M. Seltzer, J. Chang, J.S. Coursey, R. Sukumar, D.S. Zucker, and K. Olsen
XCOM: Photon Cross Sections Database NIST (National Institute of Standards and Technology)
<http://physics.nist.gov/PhysRefData/Xcom/html/xcom1.html>
1998.

- [70] M. Cargnelli, M. Bazzi, G. Beer, L. Bombelli, A. M. Bragadireanu, C. Curceanu, C. Fiorini, T. Frizzi, F. Ghio, B. Girolami, C. Guaraldo, R. Hayano, M. Iliescu, T. Ishiwatari, M. Iwasaki, P. Kienle, P. Lechner, P. L. Sandri, A. Longoni, V. Lucherini, J. Marton, S. Okada, D. Pietreanu, T. Ponta, A. R. Vidal, A. Scordo, H. X. Shi, D. L. Sirghi, F. Sirghi, H. Soltau, L. Struder, H. Tatsuno, O. V. Doce, E. Widmann, and J. Zmeskal. Kaonic atoms studies at DAΦNE by the SIDDHARTA experiment. *Nuclear Physics A*, 835(1-4):27–34, April 2010.
- [71] M. Iio, H. Bhang, M. Cargnelli, S. Choi, C. Curceanu, O. V. Doce, S. Enomoto, H. Fujioka, Y. Fujiwara, C. Guaraldo, T. Hashimoto, R. S. Hayano, T. Hiraiwa, S. Ishimoto, T. Ishiwatari, K. Itahashi, M. Iwasaki, H. Kou, P. Kienle, J. Marton, Y. Matsuda, H. Noumi, H. Ohnishi, S. Okada, H. Outa, F. Sakuma, M. Sato, M. Sekimoto, H. Shi, D. Sirghi, T. Suzuki, K. Tanida, H. Tatsuno, M. Tokuda, D. Tomono, A. Toyoda, K. Tsukada, A. R. Vidal, E. Widmann, B. K. Wuenschek, T. Yamazaki, and J. Zmeskal. Precision Spectroscopy of Kaonic Helium-3 Atoms X-rays at J-PARC. *EPJ Web of Conferences*, 3(1-4):03017, 2010.
- [72] B. K. Wuenschek, H. Bhang, M. Cargnelli, S. Choi, C. Curceanu, O. V. Doce, S. Enomoto, H. Fujioka, Y. Fujiwara, C. Guaraldo, T. Hashimoto, R. S. Hayano, T. Hiraiwa, M. Ho, S. Ishimoto, T. Ishiwatari, K. Itahashi, M. Iwasaki, H. Kou, P. Kienle, J. Marton, Y. Matsuda, H. Noumi, H. Ohnishi, S. Okada, H. Outa, F. Sakuma, M. Sato, M. Sekimoto, H. Shi, D. Sirghi, F. Sirghi, T. Suzuki, K. Tanida, H. Tatsuno, M. Tokuda, D. Tomono, A. Toyoda, K. Tsukada, A. R. Vidal, E. Widmann, T. Yamazaki, and J. Zmeskal. Status and plans of experiment E17 at J-PARC. *International Journal Of Modern Physics A*, 26(3-4):604–606, February 2011.

Acknowledgments

First of all, I want to thank my supervisor Eberhard Widmann, who offered me the possibility to work on this thesis. I absolutely enjoyed the work in experimental particle physics and the time at the Stefan-Meyer-Institute for subatomic physics.

I also want to express my gratitude to Johann Zmeskal. He accompanied me through all experimental works in the laboratory, he always gave me the feeling that my ideas were from substantial importance and he permitted mistakes.

Many thanks to Tomoichi Ishiwatari, who not only taught me how to handle huge amounts of data files, he always was honest and helped me patiently.

I am also indebted to Michael Cargnelli. Thanks for the help with SIDDHARTA, thanks for the advices, and especially thanks for the Monte Carlo simulations. The work for the code was immense.

In general, I want to acknowledge all people from SMI. Thanks to the students for the great times and for the nice discussions. I also enjoyed the joint work on the outreach projects of SMI. Thanks to the workshop for their quick manufacturing and for fulfilling all unconventional wishes. Special thank goes to Herbert Schneider, who did the basic work for the SIDDHARTA and E17 SDDs, but who also taught me a lot about electronics and about the mood swings of SDDs.

Furthermore, I thank all people of the E17 group in Japan for hosting me

very friendly and helping me in Japan. At this point, in particular I want to say "arigato" to Taka, who was a great host and to Sato and Hashimoto, who worked in the lab with me for such a long period. I had a lot of fun.

I thank all people of the SIDDHARTA group in Italy, for the short but nice times, the good discussions and for the successful work.

This work was supported by the FWF Project P20651-N20 and by the NLF in Frascati, Italy.

I also want to thank my family, my friends, the most important people in my life.

My special thank goes to my brother Alexander, who accompanied me through my whole life. I would not write this without him. I of course want to thank my parents for enabling me this great live and for supporting me unconditionally whenever it was necessary, and the rest of my huge family (old and new).

I also thank the greatest group in the universe - the $\phi\alpha\kappa$ (management board) Claudia, Daniela, Fabienne, Gabriele, Silvia - for the absolutely amazing times as students. And I thank all my close friends for each Friday, for the submarine, for each moonshine, for asking me, for teaching me, for discussing with me. It was always enriching.

My deepest gratitude goes to David.

Thank you. For everything.

Curriculum Vitae

Mag. rer. nat. Barbara Katharina Wünschek

Present Affiliation:

Stefan-Meyer-Institute for subatomic physics
Austrian Academy of Sciences
Boltzmannngasse 3
1090 Vienna
Austria

Permanent Address:

Hackingerstr. 42-44/1/10
1140 Vienna
Austria

Personal

Date of birth: 13 April 1983
Place of birth: Vienna, Austria
Nationality: Austria
Email: bwuenschek@oeaw.ac.at

Education

- 2012: Dissertation at the Stefan-Meyer-Institute for subatomic physics:
Comparison of the measured X-ray yields of kaonic helium-3 and helium-4
- 2008-2012: Doctoral study at the University of Vienna
- 2007: Diploma thesis at the VERA laboratory, Faculty of Physics, University of Vienna:
A study of proton irradiation of paper to assess its influence on PIXE analysis of art objects
- 2001-2007: Study of Physics at the University of Vienna
- 1993-2001: High School, Gymnasium Sacre Coeur, Vienna
- 1989-1993: Elementary School

Employment History

- 2008-2012: Scientific employee at the Stefan-Meyer-Institute for subatomic physics
- 2007-2008: Scientific consultant at the Dean's office, Faculty of Physics, University of Vienna
- July 2005: Scientific aide at the Institute for Isotope Research and Nuclear Physics
University of Vienna
- 2001-2002: Part-time employee at the Planetarium Vienna

Stay abroad

- 2009-2010: for a total of 4 months at KEK, Tsukuba, Japan
- 1999: for a total of 1 month at the Anadyr High School, Sebastopol, USA

Publication list

ISI listed publications

Milota et al. *PIXE measurements of Renaissance silverpoint drawings at VERA*, Nuclear Instruments & Methods In Physics Research Section B-Beam Interactions With Materials And Atoms, 2008, 266

Iio et al. *Precision Spectroscopy of Kaonic Helium-3 Atoms X-rays at J-PARC*, 19th International Iupap Conference On Few-Body Problems In Physics, 2009, 3

Zmeskal et al. *The AMADEUS experiment - precision measurements of low-energy antikaon nucleus/nucleon interactions*, Nuclear Physics A, 2010, 835

Bazzi et al. *First measurement of kaonic helium-3 X-rays*, Physics Letters B, 2011, 697, 199-202

Wuenschek et al. *Status And Plans Of Experiment E17 At J-Parc*, International Journal Of Modern Physics A, 2011, 26, 604-606

Bazzi et al. *Determination of upper limits of the strong-interaction widths of the kaonic ^3He and ^4He $2p$ states*, submitted to Physics Letters B

Wuenschek et al. *Temperature dependencies of the energy and time resolution of silicon drift detectors*, in progress

Further Publications

Doce et al. *Low energy kaon nuclei interaction studies at DAΦNE*. 9th International Iupap Conference On Few-Body Problems In Physics, 2009, 3

Doce et al. *Low energy kaon nuclei interaction studies at DAΦNE*. EPJ Web of Conferences, 2010, 3

Ishiwatari et al. *Precision spectroscopy of Kaonic helium-3 and helium-4 $3d \rightarrow 2p$ X-rays*. Hadron 2009, 2010, 1257

Rizzo et al. *Kaonic atoms measurements at the DAΦNE accelerator: the SIDDHARTA experiment*. Journal of Physics: Conference Series 348 (2012) 012003

Contributions to conferences and workshops

International Workshop on Hadronic Atoms and Kaonic Nuclei - Solved Puzzles, Open Problems and Future Challenges in Theory and Experiment, ECT 2009*, Italy

International Workshop on Meson Production, Properties and Interaction, Meson 2010, Poland

International Conference on Hypernuclear and Strange Particle Physics, HYP-X 2009, Japan

Meeting of the Austrian Physical Society, OPG 2010, Austria

International Conference on Exotic Atoms and Related Topics, EXA 2011, Austria